SANDIA REPORT
SAND2012-7934
Unlimited Release
Printed September, 2012

Compressible Instability of Rapidly Expanding Spherical Material Interfaces

Mina Reda Mankbadi, S. Balachandar, and Alexander L. Brown

Prepared by
Sandia National Laboratories
Albuquerque, New Mexico 87185 and Livermore, California 94550

Sandia National Laboratories is a multi-program laboratory managed and operated by Sandia Corporation, a wholly owned subsidiary of Lockheed Martin Corporation, for the U.S. Department of Energy's National Nuclear Security Administration under contract DE-AC04-94AL85000.

Approved for public release; further dissemination unlimited.

Issued by Sandia National Laboratories, operated for the United States Department of Energy by Sandia Corporation.

NOTICE: This report was prepared as an account of work sponsored by an agency of the United States Government. Neither the United States Government, nor any agency thereof, nor any of their employees, nor any of their contractors, subcontractors, or their employees, make any warranty, express or implied, or assume any legal liability or responsibility for the accuracy, completeness, or usefulness of any information, apparatus, product, or process disclosed, or represent that its use would not infringe privately owned rights. Reference herein to any specific commercial product, process, or service by trade name, trademark, manufacturer, or otherwise, does not necessarily constitute or imply its endorsement, recommendation, or favoring by the United States Government, any agency thereof, or any of their contractors or subcontractors. The views and opinions expressed herein do not necessarily state or reflect those of the United States Government, any agency thereof, or any of their contractors.

Printed in the United States of America. This report has been reproduced directly from the best available copy.

Available to DOE and DOE contractors from
U.S. Department of Energy
Office of Scientific and Technical Information
P.O. Box 62
Oak Ridge, TN 37831

Telephone: (865) 576-8401
Facsimile: (865) 576-5728
E-Mail: reports@adonis.osti.gov
Online ordering: http://www.osti.gov/bridge

Available to the public from
U.S. Department of Commerce
National Technical Information Service
5285 Port Royal Rd.
Springfield, VA 22161

Telephone: (800) 553-6847
Facsimile: (703) 605-6900
E-Mail: orders@ntis.fedworld.gov
Online order: http://www.ntis.gov/help/ordermethods.asp?loc=7-4-0#online

SAND2012-7934
Unlimited Release
Printed September 2012

Compressible Instability of Rapidly Expanding Spherical Material Interfaces

Mina Reda Mankbadi
S. Balachandar
University of Florida
Department of Mechanical Engineering

Alexander L. Brown
Fire and Aerosol Sciences, Org. 1532
Sandia National Laboratories
P.O. Box 5800
Albuquerque, New Mexico 87185-1135

Abstract

In a spherical shock-tube a high-pressure gas contained in a small spherical shell is suddenly released. The flow structure is characterized by a forward moving primary shock and a backward moving secondary shock. A material interface is formed between the outward and the inward shocks. Interfacial material mixing appears in many modern technologies including combustion, supersonic flows, explosions, spray development, and environmental flows. Accurate simulations of the dynamics of interfaces separating the two fluids are essential in computing fluid mixing. Our goal here is to extend such progress to the fast energy-exchange environment.

ACKNOWLEDGMENTS

Thanks to the members of the dissertation committee Drs. Roy, Ukeiley, and Wu. and to other members of the University of Florida's Computational Multi-Physics Group, Georges Akiki, Subramanian Annamalai, Charles Cook, Hyun Lee, Dr. Manoj Parmar, Mrugesh Shringarpure, Gordon Taub, Nadim Zgheib and Dr. Yue Ling.

Support is appreciated from the sponsors of the research, the University of Florida's Fellowship, the Department of Energy's Sandia Fellowship, and the Air Force Office of Scientific Research Grant. Special thanks to Dr. T. Aselage of Sandia National Labs for his guidance and advice.

CONTENTS

1. INTRODUCTION 1
1.1. Background of the Base Flow 1
1.1.1. The Flow Structure 1
1.1.2. Theoretical Models 2
1.1.3. Numerical 2
1.1.4. Experiments 3
1.2. Rayleigh-Taylor and Richtmyer-Meshkov Instabilities 3
1.2.1. Rayleigh-Taylor Instability (RTI) 3
1.2.2. Richtmyer-Meshkov Instability (RMI) 4
1.3. Objectives 5

2. COMPRESSIBLE INVISCID INSTABILITY OF RAPIDLY EXPANDING SPHERICAL MATERIAL INTERFACES 6
2.1. Introduction 6
2.2. Formulation 9
2.2.1. Base Flow Equations (Zero-Order) 9
2.2.2. The Linearized Perturbation Equations 10
2.2.3. Spherical Harmonic Decomposition 11
2.2.4. Boundary Conditions 13
2.3. The Numerical Scheme 13
2.3.1. Extension of the Roe-Pike Method 14
2.3.2. Inner Boundary Numerical Implementation 16
2.4. Results and Discussion 17
2.4.1. The Base Flow 17
2.4.2. The Perturbation Solution 20
2.4.3. The Effect of the Perturbation's Initial Condition on the Amplification Rate 23
2.4.4. Effect of the Spherical Wave Number on the Growth Rate 24
2.4.5. Comparison with Theoretical Models 26
2.5.1. Set 1: Pressure Ratio is Equal to the Density Ratio 32
2.5.2. Set 2: Pressure Ratio is Fixed at 100 but the Density Ratio is Varying 37
2.5.3. Set 3: The Density Ratio is Fixed at 6 but the Pressure Ratio is Varying 38
2.6. Summary 39

3. VISCOUS EFFECTS ON THE RAYLEIGH-TAYLOR INSTABILITY OF RAPIDLY EXPANDING SPHERICAL MATERIAL INTERFACES 42
3.1. Introduction 42
3.2. Formulation 43
3.2.1. Base Flow Equations (Zero-Order) 43
3.2.2. The Linearized Perturbation Equations 44
3.2.3. Spherical Harmonic Decomposition 46
3.2.4. Dimensionless Conservative Form 48
3.3. Boundary Conditions and Numerical Scheme 50
3.3.1. The Numerical Scheme 50
3.3.2. Extension of the Roe-Pike Method 50
3.3.3. Inner Boundary Numerical Implementation 52
3.4.1. The Base Flow 53

3.4.2. The Perturbation Solution 54
3.4.3. Effect of the Wave Number 57
3.4.4. Comparison with Theoretical Models 58
3.4.5. The Effect of the Reynolds Number 59
3.4.6. The Wrinkling of the Contact Interface 59
3.5. Conclusions 60

4. FUTURE WORK: SIMULATIONS OF THE EFFECTS OF SOLID PARTICLES ON FLOW INSTABILITY IN DETONATIVE COMBUSTION 61
4.1. Introduction 61
4.1.1. Significance of the Problem 61
4.1.2. Review of Recent Work 62
4.2. Formulation 63
4.2.1. Description of the Flow 63
4.2.2. Direct versus Splitting Approaches 64
4.2.3. Base Flow Governing Equations 64
4.2.4. The Perturbation Equations 66
4.3. Preliminary Results 67
4.3.1. Base Flow 68
4.3.2. Preliminary Perturbation Flow- Analytical Solution for the Stability of Two Contact Surfaces 70
4.4. Proposed Work 73

5. SUMMARY 75

6. REFERENCES 76

FIGURES

Figure 1–1. A contact interface represented by the green circle between the two shocks (1-1a) and the Ring Nebula (1-1b) 1
Figure 1–2. A contact interface represented by the green circle between the two shocks (1-2a) and the Ring Nebula (1-2b) 2
Figure 2–1. The radial dependence of (1a) pressure, (1b) radial velocity, and (1c) density of the base flow at 4 different non-dimensional times. The location of the primary shock (PS), secondary shock (SS) and contact interface (CI) are most evident in the density profile and are marked. The above results are obtained with a discretization of 2000 uniform grid points extending up to a radial location of $\boldsymbol{\xi} = 15.75$. 18
Figure 2–2. $\boldsymbol{\xi}$- $\boldsymbol{\tau}$ Diagram of the location of the contact interface, primary shock, and secondary shock. In terms of the original non-dimensional location (2a), and rescaled by the location of the contact interface (2b). 19
Figure 2–3. The constant deceleration of the CI and its grid independence. 19
Figure 2–4. Grid Study of base flow parameters Atwood number and the CI width. 20
Figure 2–5. The radial structure of the perturbed flow's density, radial velocity, tangential velocity, and temperature eigen modes for $\mathbf{n = 40}$ 21

Figure 2–6. Dependence of perturbation structure on spherical wave number (6a) and the finite width of the Contact Interface (6b). 22
Figure 2–7. Peak perturbation density and radial velocity growth over time. 22
Figure 2–8. The effect of the initial spatial profile on the computed growth rate (8a) and calculating the growth rate based on the radial integration of a variable squared (8b). 24
Figure 2–9. The global growth rate vs. the wave number for various resolutions. 26
Figure 2–10. The effect of the wave number on the growth rate. 30
Figure 2–11. The Contact Interface for a wave number of $\mathbf{n = 45}$ and a mode of $\mathbf{m = 7}$ (11a) and for a wave number of $\mathbf{n = 9}$ and mode of $\mathbf{m = 7}$ (11b). 31
Figure 2–12. Parametric Study of the Pressure Ratio and Density Ratio. 32
Figure 2–13. The Atwood number as a function of time for various pressure ratios and density ratios. 33
Figure 2–14. The CI Velocity as a function of time for various pressure ratios and density ratios. 35
Figure 2–15. The growth of the perturbations for a wave number of 45 for various pressure ratios. 36
Figure 2–16. The growth rate predicted by various theoretical works for a wave number of 45 for various pressure ratios. 36
Figure 2–17. The Atwood number (17a) and CI Velocity (17b) as a function of time for a pressure ratio of 100 and various density ratios. 37
Figure 2–18. For a pressure ratio of 100, the growth of the perturbation for various density ratios at a wave number of 45. 38
Figure 2–19. The Atwood number (19a) and CI Velocity (19b) for a density ratio of 6 and various pressure ratios. 38
Figure 2–20. For a density ratio of 6, the growth of the perturbation for various density ratios at a wave number of 45. 39
Figure 3–1. The radial dependence of (a) pressure, (b) radial velocity, and (c) density of the base flow at 4 different non-dimensional times. The location of the primary shock (PS), secondary shock (SS) and contact interface (CI) are most evident in the density profile and are marked. The above results are obtained with a discretization of 2000 uniform grid points extending up to a radial location of $\boldsymbol{\xi}$ = 15.75. 53
Figure 3–2. a) $\boldsymbol{\xi}$-$\boldsymbol{\tau}$ Diagram of the location of the contact interface, primary shock, and secondary shock. b) Grid independence of the Atwood number. 54
Figure 3–3. The radial shape of the perturbed flow's density and radial velocity for both the inviscid and viscid cases. The spherical wave number is 1862 and the Atwood number is 0.3575. 55
Figure 3–4. The radial shape of the perturbed flow's tangential velocity and total energy for both the inviscid and viscid cases. The spherical wave number is 1862 and the Atwood number is 0.3575. 56
Figure 3–5. a) Viscous vs. inviscid evolution of the peak perturbation radial velocity. b) the growth of the inviscid perturbation vs. the viscous perturbation. 56
Figure 3–6. The global growth rate vs. the wave number for various Atwood numbers at a Reynolds number of 6.2 x 105. 57
Figure 3–7. The effect of the wave number on the growth rate. 58
Figure 3–8. The effect of the Reynolds number on the growth rate for an Atwood number of 0.3575. 59

Figure 3–9. The total density of the interface for a wave number of 40 and Atwood number of 0.4039..... 60
Figure 4–1. Observed Cellularity Developing on the Surface of a Spherically-Expanding Flame (Marshall et al. 2010)..... 61
Figure 4–2. Frost et al. Experimental Results..... 62
Figure 4–3. Sector of a sphere from Balakrishnan and Menon (2011), parts A and, B are the simulated iso-surfaces of the mixing layer. 63
Figure 4–4. Schematic Illustration of Explosive Dispersals from a Spherical Charge Containing Gas-Particle Mixture (Ling et al, 2010)..... 64
Figure 4–5. The radial dependence of (a) pressure, (b) radial velocity, and (c) density of the base flow at 4 different non-dimensional times. The location of the primary shock (PS), secondary shock (SS) and contact interface (CI) are most evident in the density profile and are marked. The above results are obtained with a discretization of 2000 uniform grid points extending up to a radial location of $\boldsymbol{\xi}$ = 15.75..... 69
Figure 4–6. $\boldsymbol{\xi}$- $\boldsymbol{\tau}$ Diagram of the location of the contact interface, primary shock, and secondary shock. In terms of the original non-dimensional location (6a), and rescaled by the location of the contact interface (6b). 69
Figure 4–7. Numerically Predicted Gas and Particle Velocities in the Planar Case using the Eulerian Approach in Comparison with the planar Standard Drag ODE. 70
Figure 4–8. A model of Two Contact Surfaces Distance "L" Apart where $\boldsymbol{\varrho 2 > \varrho 1 > \varrho o}$..... 70
Figure 4–9. Imaginary Part of Omega. 72
Figure 4–10. Real Part of Omega. 72

1. INTRODUCTION

1.1. Background of the Base Flow

1.1.1. The Flow Structure

While our focus herein is on understanding the instability associated with detonative combustion, it is imperative that we first review the base flow that produces these instabilities. The base flow models can be classified into two groups: (A) point source explosions, where the energy is released from a singular point at the center of the explosion, and (B) a bursting sphere model. The analytical solutions for the point source explosions assuming strong-shock relations are the self-similar solutions of Taylor (1950a), Sedov (1946), and Van Neumann (1947).

Our interest herein is on the high-pressure gas explosions resulting from a bursting sphere. When a highly pressurized sphere is suddenly released, an outward-moving primary shock develops, an inward rarefaction wave in the high-pressure region develops, and a contact interface (CI) appears between the rarefaction wave and the shock wave. Due to the spherical geometry, the rarefaction wave soon develops into an imploding spherical shock. At the contact interface, the pressure and velocity on the two sides are the same, but the density and temperatures on the two sides are different. The contact discontinuity initially moves behind the main shock front but with a decreasing velocity and then starts moving towards the center. This is demonstrated by the sketch in Figure 1–1a. The Ring Nebula (shown in Figure 1–1b) is believed to be resulting from a past explosion of a star. The CI appears in the Ring Nebula as separating the white and the yellow-colored matter. Due to the density jump across the CI, instability may arise and result in distorting the CI as shown in Figure 1–2a. Also, shown in Figure 1–2b is the Eskimo Nebula in which it is hypothesized that the radial spikes are the result of the development of the interfacial instability following the initial explosion of the star.

1a

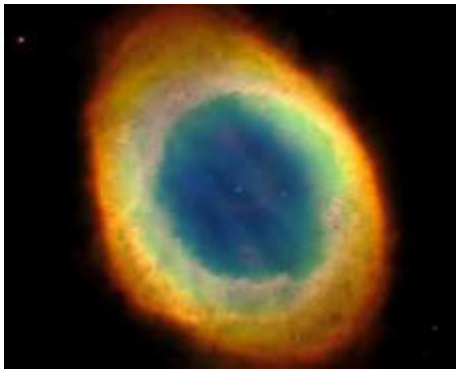

1b

Figure 1–1. A contact interface represented by the green circle between the two shocks (1-1a) and the Ring Nebula (1-1b).

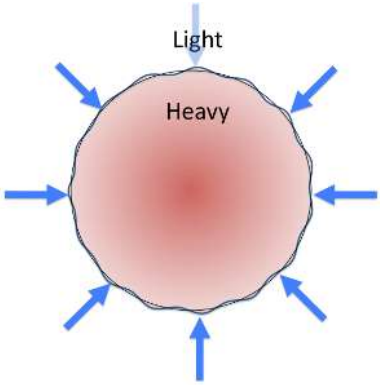

2a

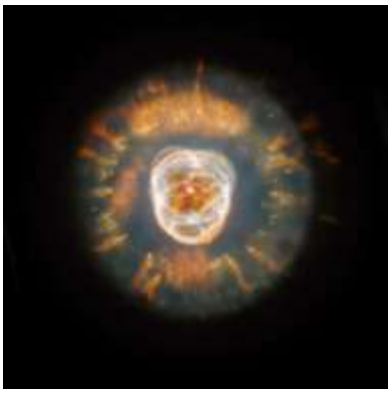

2b

Figure 1–2. A contact interface represented by the green circle between the two shocks (1-2a) and the Ring Nebula (1-2b).

1.1.2. Theoretical Models

An excellent review of the theoretical work in modeling the base flow is given by Sachdev (2004). McFadden (1952) and Friedman's (1961) theoretical solutions assumed that at t = 0, a unit sphere containing a perfect gas at a high pressure is allowed to expand suddenly into a homogeneous atmosphere, such as air. This is an analogue of a plane shock tube problem, but here additionally the spherical term must also be included. McFadden (1952) wrote out a series form of the solution, the zero-order solution in the series is simply the solution of the plane shock tube problem. McFadden (1952) found first order correction for various regions of the flow and explained how the geometry affected the solutions of the shock tube problem. Essentially the same problem was treated subsequently by Friedman (1961), who obtained a solution by perturbing the corresponding plane rarefaction wave. Both McFadden (1952) and Friedman (1961) essentially produced the same model, however in the former, the gas sphere pressure is relatively low such that the phenomenon of a secondary shock is not observed. In the case of the rapid expansion of a higher pressure gas sphere considered by Friedman (1961), a secondary shock develops due to the spherical effect.

The secondary shock is absent in the plane one-dimensional shock-tube problem since the main shock and the expansion come into instantaneous equilibrium, being separated by a region of uniform pressure and velocity. The phenomenon of secondary shock in spherical explosions can be described as follows: physically the high pressure gas passing through a spherical rarefaction wave must expand to lower pressures than those reached through an equivalent one-dimensional expansion, due to the increase in volume. Therefore, the pressure at the tail of the rarefaction wave is lower than that transmitted by the main shock and a compression or a secondary shock must be inserted to connect these two phases.

1.1.3. Numerical

In terms of Numerical work, Brode (1959) used the method of artificial viscosity to numerically compute results for the sudden release of an initially static high pressure gas from spherical enclosures. Brode succeeded in capturing the complete post-explosion wave structure and the birth and evolution of the secondary shock which originates at the tail of the inward facing rarefaction wave. The calculations further revealed that the contact interface moves initially outwards following the blast wave but decelerates and subsequently reverses direction to move

inward. The main contribution of this numerical study is the detection of a secondary shock which originates as an imploding shock following the inward rarefaction into the high pressure gases.

1.1.4. Experiments

Experimental investigations of a bursting sphere flow are given in Boyer (1960). The initial sphere radius was 5.08 cm and the pressure was 22 atm. Brode's (1959) results compared favorably with the experimental data by Boyer (1960), but has also showed some notable disagreements such as the arrival time of the secondary shock at the center.

1.2. Rayleigh-Taylor and Richtmyer-Meshkov Instabilities

1.2.1. Rayleigh-Taylor Instability (RTI)

Rayleigh-Taylor instability (RTI) occurs at the interface of two fluids of different densities when the lighter fluid is pushing on the heavier fluid. Lord Rayleigh (1883) is credited with discovering these effects under the acceleration of Earth's gravity. Taylor (1950b) is credited with expanding the theorem to account for any acceleration in addition to gravitational acceleration. Due to the lighter fluid's attempt to support the weight of heavier fluid any small perturbation can trigger the start of the instability.

In Taylor's (1950b) analysis, he considers two fluids with different densities initially at rest. The heavier fluid is denoted by ρ_2 while the lighter fluid is represented by ρ_1. The interface is located at $z = 0$ and subjected to the gravitational acceleration$\boldsymbol{g} = -g\hat{\boldsymbol{z}}$. The perturbations are then expanded in the $\hat{\boldsymbol{x}}$ direction in terms of complex exponentials with a planar wave number k. The growth in time is assumed to follow be exponential growth such that the perturbation amplitude, a can be written as $a(x, z, t) = a(z)e^{ikx+\gamma t}$ where γ is the amplification rate. A simple dispersion relation can be obtained by applying the conservation of mass conditions. Upon enforcing continuity of the normal velocity and pressure Taylor pioneers a new area of research by arriving at his expression $\gamma^2 = \mathrm{gkAt}$. The Atwood number At is simply the density difference normalized by the density sum.

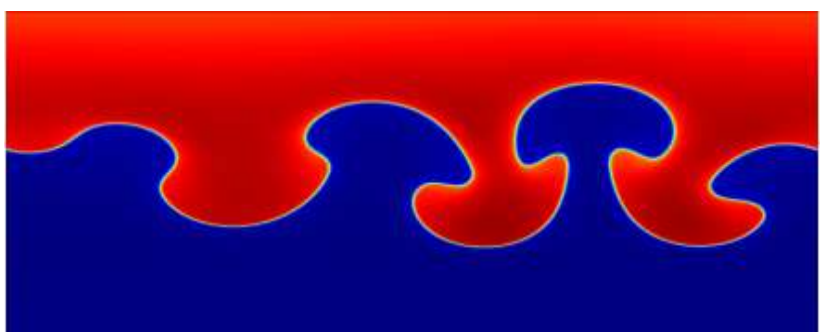

Figure 1-3. Pictorial representation of nonlinear RTI spikes and bubbles.

Taylor's exponentially growing analysis is linear; consequently, it breaks down when the perturbation amplitude is too large. Nonlinear effects are no longer negligible and are observed as „spikes' and „bubbles' while they roll up forming vortices. During the nonlinear phase of RTI, the „bubbles' of lighter fluid rise into the heavier fluid while the „spikes' of heavier fluid „fall'

into the lighter fluid as depicted by Figure 1-3. Taylor's profound work is discussed in further detail in Chapter 2 to elaborate upon the subsequent work of others that ventured into the same field.

1.2.2. Richtmyer-Meshkov Instability (RMI)

Richtmyer-Meshkov Instability (RMI) occurs when an interface between two fluids of differing density is impulsively accelerated. The passage of a shock wave is a classical problem studied by many (Richtmyer, 1960, Meshkov, 1969). As in the case of RT instability, the onset of RM instability is triggered by small amplitude perturbations that initially behave linearly in time. Likewise, the linear regime is concluded with the start of the non-linear regime where the lighter fluid penetrates the heavier fluid forming bubbles and the heavier fluid penetrates the lighter forming spikes as depicted in Figure 1-4.

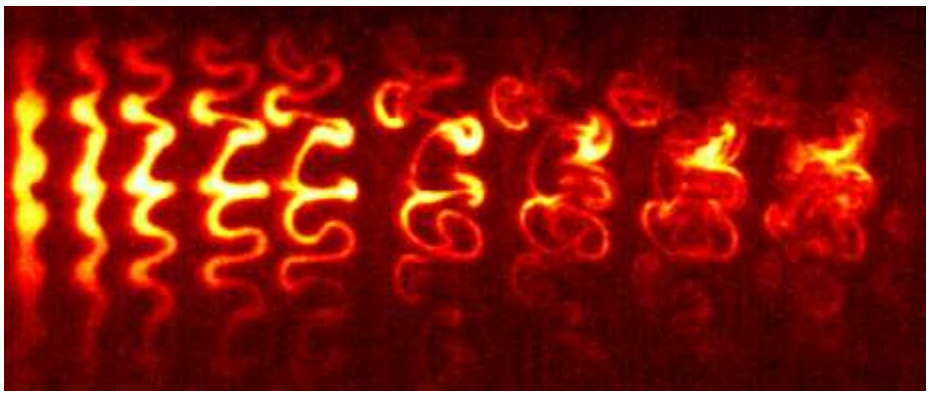

Figure 1-4. RMI (Rightley et al. 1997) Pictorial representation of nonlinear RTI spikes and bubbles.

The understanding of Richtmyer-Meshkov instabilities is seen as the impulsive limit Rayleigh-Taylor instability. Rather than a constant acceleration due to gravity, the interface is impulsively accelerated due to a shock wave or time varying acceleration. Such a phenomenon is often referred to as baroclinic deposition of vorticity onto the interface. Building upon the RT analysis, the amplitude of the disturbance is governed by $\ddot{a}(t) = a(t)\ \ g(t)kAt$. The time varying acceleration $g(t)$ is assumed to occur over a short time period such that the imparted incremental velocity Δu can be defined as: $\Delta u = \int g(t)dt$. Due to the rapid nature of the impulse, the differential equation is integrated to yield $\dot{a}(t)/a_o = \Delta u\ kAt$. The growth rate is given in terms of the initial amplitude $a_o$and planar wavenumber k. Note that the instability is active regardless of acceleration's direction and for all impulses. Consequently, the amplitude of the mixing layer grows linearly in time unlike the RT case which grows exponentially, but similarly it is proportional to the wavenumber k and Atwood number. In chapter 2, the impulsive effects of RMI are present consequently they add to the intricacy of the problem in question. Note that both RMI and RTI are inviscid studies Chandrasekhar (1981) addresses the effects of viscosity for a planar Rayleigh-Taylor instability with zero thickness. In Chapter 3, his work is utilized as means of verification.

1.3. Objectives

Classical Raleigh Taylor instability has been of interest since the early 1900s. It is the interfacial instability produced by a density discontinuity between two fluids in a planar context subjected to a body force, usually gravity. The classical problem does not account for Bell-Plesset effects or curvature effects, impulsive effects, and compressibility effects. In the introduction of Chapter 2, after discussing the history of the various instability mechanisms mentioned, we investigate these additional effects for a moving rather than stationary interface. The Chapter is self-contained and as such it explains in detail the formulation of both the base flow and the perturbed flow. The procedure by which the base flow's governing equations are perturbed and then decomposed in terms of spherical harmonics is elaborated upon. Following which in Chapter 2, we extend the Roe-Pike numerical scheme so that it can be employed to numerically solve the perturbation equations. After which, the growth rate is found to be exponential rather than power law and quantitatively compared with various theoretical works. The effects of compressibility are fully explored through a parametric study. The saturation phenomenon of the growth rate at large spherical wave numbers is explained by comparison with the work by Banderia (1984).

In Chapter 3, the viscous effects are investigated for various Reynolds number and it is shown that an optimal spherical mode with a peak growth rate appears. Unlike the inviscid case, the saturation phenomenon is not present for the viscous case because the viscosity dampens the growth of the instability for very large wave numbers. As in the inviscid case, a comparison with theoretical models is also conducted for the viscous case. The Reynolds number and Prandtl number are shown to dictate the spherical wave number at which the peak growth rate is reached. The spherical wave number determines the number of instabilities that can be experimentally visualized.

Chapter 4 contains the formulation for our future work on the Eulerian-Eulerian multiphase problem where particles are included. As in Chapter 2 and Chapter 3, a similar system of equations is obtained for the perturbed flow. Additionally, an analytical model that predicts the growth rate of the two interfaces close to each other is presented as a guide for the future simulations to be performed. Due to computational constraints, there is little research being done on the subject of a gas-gas interface, in the presence of a neighboring particle-gas interface. The employment of spherical harmonics has proven to be greatly advantageous since it is not as computationally demanding as a Direct Numerical or Large Eddy Simulation (DNS or LES). In the future, with the advancement of computational resources a Direct Numerical Simulation (DNS) for given pressure and density ratio, initial spherical diameter, Reynolds and Prandl numbers, and a single disturbance can be performed.

2. COMPRESSIBLE INVISCID INSTABILITY OF RAPIDLY EXPANDING SPHERICAL MATERIAL INTERFACES

2.1. Introduction

The interest in studying the stability of a spherical material interface stems from its relevance to many engineering applications such as supersonic combustion, pulse denotation engines, fusion reactors, propellant rocket motors, and supernovae. Understanding the mechanisms by which the contact interface becomes unstable has several benefits in these applications. For instance regarding combustion-based applications, a spherical interface separates the hot fuel mixture from the cold ambient air. Mixing at the interface is essential for continued burning and energy release. Consequently, the stability of the interface strongly affects the combustion efficiency.

Here we consider the spherical shock tube problem, where a finite-sized spherical container filled with high pressure gas is suddenly released into the ambient and we are interested in understanding the initial linear stage of the resulting instability. Immediately following the release, just as in a planar shock tube, a spherical blast (or shock) wave and a contact discontinuity (the material interface between the gas that was initially within the container and the ambient) propagate radially out, but the expansion fan propagates into the high pressure gas. Although there is a substantial body of knowledge on the instability of shock waves and material interfaces in isolation under idealized conditions, here we are interested in relating this understanding to the instability of the more complex flow resulting from the release of a finite-sized high pressure spherical container.

The instability of a planar shock wave in a material with an arbitrary equation of state has been rigorously investigated (Swam and Fowles, 1975, Erpenbeck, 1962). When applied to the ideal gas case it can be readily shown that a planar shock remains linearly stable for all values of the adiabatic index. The stability of a spherical shock wave produced by the rapid release of initially highly focused energy has also received much attention in the context of supernovae (Ryu and Vishniac, 1987, Kushnir et al., 2005). They have considered finite release of energy from an infinitesimal point source, where only a strong shockwave is produced, without an associated contact discontinuity or expansion fan. These studies agree that an expanding spherical shock is generally stable except when the adiabatic index is close to one and only for a limited range of large wave numbers. Hence, an expanding spherical shockwave in air with the adiabatic index being close to 1.4 remains stable. On the other hand, an imploding shock is unstable over a wide range of adiabatic index and disturbance wavelengths.

The contact interface is also a surface across which density jumps, but unlike a shock front the velocity and pressure are continuous. The early work of Rayleigh (1900) and Taylor (1950) considered the stability of a plane interface separating two incompressible stationary fluids of different densities subjected to gravity acceleration. When the direction of gravity is from the heavier to the lighter fluid, Taylor showed that the flow is unstable and that the instability growth rate is proportional to the square root of the product of wave number, acceleration, and Atwood number. The latter is defined as the ratio of the difference between the two densities to their sum.

Motivated by the phenomenon of cavitation, Plesset (1954) studied the Rayleigh-Taylor (RT) instability in the context of a spherical surface of discontinuous density. In particular he considered the collapse of the interface that separates an inner air bubble from the outer liquid.

Plesset (1954) and Bell (1951) demonstrated that in addition to the classical RT instability there is an additional mechanism that was not present in the planar case. This additional instability mechanism caused by the movement of a curved interface is pertinent only in cylindrical or spherical geometries and is commonly referred to as the Bell-Plesset (BP) effect.

Both Plesset's (1954) and Taylor's (1950) studies as well as the majority of studies that ensued were limited to incompressible flows. However recently, the compressibility effects have received attention due to their relevance to many important applications. Amendt et al. (2003) considered a "compressible" spherical model similar to that of Plesset, in which the density both inside and outside the interface is taken to be constant in space, but vary in time and thus introducing compressibility effects. The density variation of the inner fluid is dictated by the motion of the interface, by satisfying the continuity equation. The time variation of the density of the outer fluid is used as a free compressibility parameter. An extension of this model is presented by Epstein (2004) where the compressibility effects are considered in the base flow by allowing the density to vary in time. However the density's time rate of change was set to be equal on both sides of the Contact Interface (CI). The perturbed flow is still assumed to be incompressible allowing the growth rate to be explicitly given by a second-order ordinary differential equation.

Amendit's and Epstein's studies as well as others that predated or followed them (Vandervoot 1961; Bernstein and Brook, 1983; Sharp, 1984; Yang and Zhang, 1993; and Turner , 2002) have not been conclusive. Some indicate enhancement of instability growth rate due to compressibility, while others suggesting stabilizing effects of compressibility. Recently, Yu and Livescu (2008) performed a comprehensive investigation of the compressibility effect on the stability of a cylindrical contact interface in order to clarify the matter. The problem was simplified by assuming the interface to be stationary and the base flow's temperature to be uniform. The base flow is allowed to vary along the radial direction, but not in time. Regarding the conflicting results on the effects of compressibility, Yu and Livescu clarified that the effect of compressibility can be different depending on how the incompressible limit is approached. It can be evaluated either by letting the Mach number go to zero or by letting the adiabatic index go to infinity. They concluded that the growth rate increases as the Mach number approaches zero, but it decreases as the adiabatic index increases.

In the present problem of a sudden release of high pressure gas from a finite-sized spherical container, the resulting base flow is spherically symmetric and characterized by the close presence of all three compressible flow features - shock, contact discontinuity and expansion fan. Experiments of spherical explosions, where the detonation product plays the role of the high pressure gas, show the air shock to be stable, while the contact discontinuity between the products of detonation and the ambient to be highly unstable. Accordingly, in the present context of a spherical shock tube, the contact discontinuity can be expected to undergo classical RT and BP instabilities.

Despite its simplicity, the spherical shock tube configuration departs in several significant ways from the idealized conditions assumed in the above mentioned theoretical analysis of the classical instabilities. In a spherical shock tube the instability is influenced by various mechanisms which include classical Rayleigh-Taylor (RT) effect, Bell-Plesset (BP) or geometry/curvature effect, the effect of impulsively accelerating the interface, and compressibility effects. Henceforth, the present instability will be referred to as non-classical RT instability to distinguish it from classical RT instability.

Furthermore, in a spherical shock tube following the release, the density field develops substantial variation along the radial direction around the contact discontinuity and thus differs from the uniform density field assumed in the instability theories. Also, unlike the planar counterpart, the time-dependence of the flow in a spherical shock tube is quite complex, and cannot be taken to be either steady or self-similar. In particular, quantities of relevance to interfacial instability such as the Atwood number and acceleration of the contact discontinuity cannot be assumed to remain constant, and consequently the effect of their time-dependence must be accounted. Lastly, the contact discontinuity is embedded between the primary shock wave and the secondary shock wave that develops from the tail of the expansion fan. The influence of these additional discontinuities in the base flow on the stability of the contact discontinuity has to be considered. Finally, in the case of spherical shock tube compressibility effects are critical in evaluating the spherically symmetric base flow and correspondingly compressibility effects on its instability must be thoroughly ascertained.

Although the theoretical analysis of the spherically symmetric base flow resulting from a spherical shock tube was studied (McFadden, 1952; and Friedman, 1961), the study was limited to early times and includes several simplifying assumptions. Owing to the complex nature of the flow there is no explicit analytic expression for the base flow. Here we consider numerical solutions of both the base flow and the perturbation and we fully account for the compressibility effects. In 1981, Roe formulated an approximate Riemann solver, which was revised in 1999 by Roe and Pike. Here we use a WENO reconstruction algorithm (Haselbacher, 2005) that is based on the work of Jian and Shu (1996). The Roe-Pike solver coupled with a high-order WENO scheme is employed to simulate the base flow. The governing equations for the 3D linear perturbations are derived and then solved numerically using the same scheme. Linearization allows for the expansion of the 3D disturbance in terms of spherical harmonics.

Thus, in the present work we numerically investigate the instability of the rapidly expanding material interface resulting from a spherical shock tube, fully accounting for compressibility effects and without any assumptions or approximations regarding the time and space dependence of the base flow. The numerical results will be compared against the different theoretical results to establish an approximate analytical approach that can adequately explain the computed instability.

The present investigation will be limited to an inviscid flow and thus only the Euler equations are solved for both the base flow and the perturbation. As a consequence, based on inviscid classical RT instability theory, we can anticipate the growth rate of the perturbation to monotonically increase with wave number. Clearly viscous, thermal, and mass diffusion effects must be included in order to identify the most amplified spherical harmonics. Nevertheless, with the present inviscid instability analysis we will be able to address an important question: how well the simple classical RT and BP instability theories that are based on idealized conditions are able to capture the computed inviscid instability of the spherical shock tube problem. Once we establish the applicability of the theoretical results, we will generalize the inviscid instability to a wide range of initial pressure and density ratios that parameterize the sudden release of high pressure gas from a finite-sized spherical container.

The study is presented in the following order: in section II the derivation of the perturbation equations in spherical coordinates is described. The boundary conditions and behavior near the origin are discussed in section III. The numerical scheme and boundary treatment are explained in section IV. The results for the stability of the contact interface are presented in section V for a

specific pressure and density ratio, corresponding to that considered in the classic work of Brode (1995, 1959). In section VI, a comprehensive parametric study is presented in order to analyze the effects of the two key operating parameters: initial inside-to-outside pressure and density ratios. Conclusions are given in section VII.

2.2. Formulation

Before analyzing the stability of the contact interface, the base flow must first be defined. The base flow of interest here is produced by the sudden release to the ambient of a high pressure gas contained initially in a finite-sized sphere. The limiting case for the base flow is Taylor's (1950) and Sedov's (1946) point source solution, where the initial high pressure radius goes to zero, i.e., all the energy is contained in a single point at the origin. It is well understood that in the context of a finite-source release (as opposed to point-source), in addition to the main shock wave, there will be a contact discontinuity and an expansion fan. An expansion fan consists of an infinite number of Mach waves; across the expansion fan, the flow accelerates while the static pressure and density decrease. The tail of the expansion fan, due to the radial effect, becomes a second shock wave, which after a brief period of outward propagation, turns and starts to move inwards towards the origin. These additional discontinuous surfaces were discussed by Brode (1955, 1959) and Friedman (1961). At the contact interface, the pressure and radial velocity on the two sides are the same, but the density and temperature are discontinuous across the surface. Initially, the contact discontinuity moves radially outward behind the main shock front, but its velocity continually decreases until it starts to move inwards towards the origin. After a long time, the contact discontinuity reaches an asymptotic radial location defining the near-field of the rapid energy release, while the main shock wave continues to travel out. The far-field solution of the blast wave becomes identical to Taylor's self-similar solution so long as the shock remains strong. Our focus herein is on the Rayleigh-Taylor instability of the contact interface that develops between the primary and secondary shocks.

2.2.1. Base Flow Equations (Zero-Order)

Here we pursue the approach of Ling et al. (2009) for the base flow; where due to spherical symmetry only the radial velocity is of importance. For simplicity, the fluid is taken to be a perfect gas. Upon neglecting viscosity but taking into account compressibility effects, the base flow equations reduce to a system of three nonlinear partial differential equations in r and t. The Euler continuity, momentum, and energy equations are given by:

$$\frac{\partial \varrho}{\partial t} + \frac{\partial(\varrho U)}{\partial r} + \frac{2\varrho U}{r} = 0 \tag{1}$$

$$\frac{\partial(\varrho U)}{\partial t} + \frac{\partial(\varrho U^2 + P)}{\partial r} + \frac{2\varrho U^2}{r} = 0 \tag{2}$$

$$\frac{\partial E}{\partial t} + \frac{\partial(UH)}{\partial r} + \frac{2UH}{r} = 0 \ . \tag{3}$$

Here E is the total energy and U is the base flow velocity in the radial direction. The density is ϱ; the pressure is P, and the total enthalpy H is given by:

$$H = E + P \ . \tag{4}$$

For a thermally and calorically perfect gas, the total enthalpy is related to the static temperature by $\mathrm{H} = \varrho \mathrm{c_p T}$ likewise for the total energy $\mathrm{E} = \varrho \mathrm{c_v T}$. The specific enthalpy is related to the total enthalpy as $\mathrm{H} = \varrho \mathrm{h}$ likewise for the total energy $\mathrm{E} = \varrho \mathrm{e}$. The base flow domain extends from the origin to beyond the primary shockwave where ambient conditions prevail.

2.2.2. The Linearized Perturbation Equations

The starting point for deriving the perturbation equations is the compressible Euler equations in spherical coordinates. We begin by assuming that each flow quantity is composed of the base flow $(\mathrm{U}, \mathrm{V}, \mathrm{W}, \mathrm{P}, \varrho)$ and a perturbation $(\mathrm{u}', \mathrm{v}', \mathrm{w}', \mathrm{p}', \rho')$. Thus,

$$u = U + u';\ v = V + v';\ w = W + w';\ p = P + p';\ \rho = \varrho + \rho'; \tag{5}$$

where (u', v', w', p', ρ') are the perturbation radial velocity, azimuthal velocity, zenithal (polar) velocity, pressure, and density, respectively. Upon substituting this split into the 3D Euler equations, neglecting the nonlinear terms, and subtracting the base flow equations, the linearized continuity is obtained as follows:

$$\frac{\partial \rho'}{\partial t} + \frac{1}{r^2}\frac{\partial (r^2 U \rho')}{\partial r} + u' \frac{\partial \varrho}{\partial r} + \varrho(\boldsymbol{\nabla} \cdot \boldsymbol{v}') = 0. \tag{6}$$

For the spherical coordinate system, we define:

$$D' = \boldsymbol{\nabla} \cdot \boldsymbol{v}' = \frac{1}{r^2}\frac{\partial (r^2 u')}{\partial r} + \frac{1}{r sin\theta}\frac{\partial\,(v' \sin\theta)}{\partial \theta} + \frac{1}{r sin\theta}\frac{\partial w'}{\partial \phi}\ . \tag{7}$$

The r-momentum equation is given by:

$$\varrho \frac{\partial u'}{\partial t} + \rho' \frac{\partial U}{\partial t} + \varrho U \frac{\partial u'}{\partial r} + (\rho' U + \varrho u')\frac{\partial U}{\partial r} = -\frac{\partial p'}{\partial r}. \tag{8}$$

The perturbation velocity is composed of two components: u' in the radial direction and $\boldsymbol{q}'$ for the tangential direction, where

$$\boldsymbol{q}' = v'\,\widehat{\boldsymbol{\theta}} + w'\,\widehat{\boldsymbol{\phi}}\,. \tag{9}$$

Here $\widehat{\boldsymbol{\theta}}$ and $\widehat{\boldsymbol{\phi}}$ are unit vectors along the azimuthal and zenithal (polar) directions respectively, and

$$\boldsymbol{\nabla_T} = \frac{1}{r}\left(\widehat{\boldsymbol{\theta}}\,\frac{\partial}{\partial \theta} + \widehat{\boldsymbol{\phi}}\,\frac{1}{sin\theta}\,\frac{\partial}{\partial \phi}\right) \tag{10}$$

is the gradient in the tangential direction. The tangential momentum equation is obtained from the v' and w'-momentum equations:

$$\varrho \frac{\partial \boldsymbol{q}'}{\partial t} + \varrho U \frac{1}{r} \frac{\partial (r\, \boldsymbol{q}')}{\partial r} = -\boldsymbol{\nabla_T} p' \,. \tag{11}$$

The energy equation is given by:

$$\frac{\partial E'}{\partial t} + \frac{1}{r^2} \frac{\partial (r^2 U H')}{\partial r} + u' \frac{\partial H}{\partial r} + H\, (\boldsymbol{\nabla} \cdot \boldsymbol{v}') = 0 \tag{12}$$

and,

$$H' = E' + P' \,, \tag{13}$$

where E' and H' are the total perturbation energy and total perturbation enthalpy respectively.

2.2.3. Spherical Harmonic Decomposition

Since the perturbation equations are linear, we can expand them in the $\widehat{\boldsymbol{\theta}}$ and $\widehat{\boldsymbol{\phi}}$ directions using the spherical harmonic functions as:

$$\boldsymbol{q}'(\, r, \theta, \phi, t) = \tilde{q}\, (r, t)\; r\, \boldsymbol{\nabla_T} Y_{nm}(\theta, \phi) \tag{14}$$

$$\begin{Bmatrix} \rho'(r,\theta,\phi,t) \\ u'(r,\theta,\phi,t) \\ p'(r,\theta,\phi,t) \\ E'(r,\theta,\phi,t) \\ H'(r,\theta,\phi,t) \end{Bmatrix} = \begin{Bmatrix} \tilde{\rho}(r,t) \\ \tilde{u}(r,t) \\ \tilde{p}(r,t) \\ \tilde{E}(r,t) \\ \tilde{H}(r,t) \end{Bmatrix} Y_{nm}(\theta, \phi) \,. \tag{15}$$

Here, the spherical wave number n = 0, 1, 2,… and the mode number m = 0, 1, 2,…, n. The spherical harmonic $Y_{nm}(\theta, \phi)$ of order n, m is given by:

$$Y_{nm}(\theta, \phi) = L_n^m(\theta)\, e^{im\phi} \,, \tag{16}$$

where $L_n^m(\theta)$ is the associated Legendre polynomial. Upon employing this decomposition the divergence becomes:

$$D' = \left[\frac{1}{r^2} \frac{\partial (r^2 u')}{\partial r} + \boldsymbol{\nabla_T} \cdot \boldsymbol{q}' \right] = Y_{nm} \left[\frac{1}{r^2} \frac{\partial (r^2 \tilde{u})}{\partial r} - \lambda \frac{\tilde{q}}{r} \right], \tag{17}$$

where $\lambda = n(n+1)$. After substituting the decomposition into the linearized equations we obtain:

$$\frac{\partial \tilde{\rho}}{\partial t} + \frac{1}{r^2}\frac{\partial [r^2(U\tilde{\rho} + \varrho\,\tilde{u})\,]}{\partial r} - \varrho\,\lambda\frac{\tilde{q}}{r} = 0 \tag{18}$$

$$\varrho\left(\frac{\partial \tilde{u}}{\partial t} + \tilde{u}\frac{\partial U}{\partial r} + U\,\frac{\partial \tilde{u}}{\partial r}\right) + \frac{\partial \tilde{p}}{\partial r} - \frac{\tilde{\rho}}{\varrho}\frac{\partial P}{\partial r} = 0 \tag{19}$$

$$\varrho\,\frac{\partial \tilde{q}}{\partial t} + \varrho U\left(\frac{\partial \tilde{q}}{\partial r} + \frac{\tilde{q}}{r}\right) + \frac{\tilde{p}}{r} = 0 \tag{20}$$

$$\frac{\partial \tilde{p}}{\partial t} + \tilde{u}\,\frac{\partial P}{\partial r} + U\,\frac{\partial \tilde{p}}{\partial r} + \gamma\tilde{p}\left[\frac{1}{r^2}\,\frac{d(r^2U)}{dr}\right] + \gamma P\left[\frac{1}{r^2}\,\frac{\partial(r^2\tilde{u})}{\partial r} - \frac{\lambda\tilde{q}}{r}\right] = 0\,, \tag{21}$$

where γ is the adiabatic constant and the energy equation has been replaced by an equivalent perturbation pressure equation. The final perturbation equations are written in conservative form as follows:

$$\frac{\partial \boldsymbol{U}}{\partial t} + \frac{\partial \boldsymbol{F}}{\partial r} + \boldsymbol{S} = 0 \tag{22}$$

$$\boldsymbol{U} = \begin{Bmatrix} u_1 \\ u_2 \\ u_3 \\ u_4 \end{Bmatrix} = \begin{Bmatrix} \tilde{\rho} \\ \tilde{\rho}U + \varrho\tilde{u} \\ \varrho\tilde{q} \\ \tilde{E} \end{Bmatrix} \qquad \boldsymbol{F} = \begin{Bmatrix} u_2 \\ 2Uu_2 - \tilde{\rho}U^2 + \tilde{p} \\ Uu_3 \\ \tilde{u}H + U\tilde{H} \end{Bmatrix} \tag{23}$$

$$\boldsymbol{S} = \frac{1}{r}\begin{Bmatrix} 2u_2 - \lambda u_3 \\ U[2(2u_2 - \tilde{\rho}U) - \lambda u_3] \\ \tilde{p} + 3Uu_3 \\ 2\left(\tilde{u}H + U\tilde{H}\right) - \lambda\tilde{q}H \end{Bmatrix}. \tag{24}$$

To close the system, we have:

$$\tilde{p} = (\gamma - 1)\left(\tilde{E} - Uu_2 + \frac{\tilde{\rho}}{2}U^2\right). \tag{25}$$

Thus, for a given spherical wave number n we can solve the continuity, radial-momentum, tangential-momentum, and energy equations to obtain the perturbation solution. Notice that the mode number m does not appear in the final governing equation, hence the growth of the instability is dependent only on the spherical wave number n.

2.2.4. Boundary Conditions

The disturbance must decay away from the contact interface and thus the far-field boundary condition becomes:

$$r \to \infty : \qquad \{\tilde{\rho}, \tilde{\rho}U + \rho\tilde{u}, \rho\tilde{q}, \tilde{E}\} \to \{0, 0, 0, 0\}\,. \tag{26}$$

The inner boundary condition for the perturbation flow is not as obvious. The inner boundary condition for the base flow is a reflecting wall at the origin; consequently, the inner boundary condition for the perturbation flow is also a reflecting wall at $r = 0$.

The base flow's inner reflecting boundary condition requires the radial velocity to be zero ($U = 0$) at the origin, which leads to $\partial P/\partial r = 0$ in order to satisfy the radial momentum equation. Likewise for the perturbation flow, the vectorial velocity must be zero ($\tilde{u} = 0$ and $\tilde{q} = 0$) which leads to $\partial\tilde{p}/\partial r = 0$ in order to satisfy the radial perturbation momentum equation.

1.1.1. The Perturbation Equations near the Origin

The perturbation equations as written in (22)-(25) are singular at $r = 0$; consequently, we need to examine the solution near the origin. To clarify the behavior near $r = 0$, let us rewrite the source term to as:

$$\boldsymbol{S} = \begin{Bmatrix} 2\,\tilde{\rho}\dfrac{U}{r} + \varrho\dfrac{2\,\tilde{u} - \lambda\,\tilde{q}}{r} \\ \dfrac{U}{r}\,[2\,u_2 + \varrho\,(2\,\tilde{u} - \lambda\,\tilde{q}\,)] \\ \dfrac{\tilde{p}}{r} + 3\,\varrho\,\tilde{q}\dfrac{U}{r} \\ 2\,\tilde{H}\,\dfrac{U}{r} + H\dfrac{2\,\tilde{u} - \lambda\,\tilde{q}}{r} \end{Bmatrix}. \tag{27}$$

Upon substituting the base flow solution near the origin, the perturbation equations can be reduced to observe that the singularity arises from the two terms:

$$\frac{\tilde{p}}{r};\ \frac{2\,\tilde{u} - \lambda\tilde{q}}{r}\ , \tag{28}$$

which should be handled carefully in any numerical boundary treatment.

2.3. The Numerical Scheme

A finite volume approach is employed to solve the system of perturbation equations. The flux is calculated by applying the Roe scheme (Roe, 1981; and Roe and Pike, 1999). Gradients are calculated using a Weighted Essentially Non-Oscillatory (WENO) scheme that is second order accurate (Haselbacher, 2005; and Jian and Shu, 1996). The time evolution is according to the classical fourth order Runge-Kutta method. The Roe-Pike scheme is extended here for the perturbation flow.

2.3.1. Extension of the Roe-Pike Method

There are three major steps in the Roe-Pike Method. The first of which involves writing the equation in a semi-linear form by defining a Jacobian $\boldsymbol{A} = \partial \boldsymbol{F}/\partial \boldsymbol{U}$ for some „average' values of the quantities and calculating the eigenvalues/vectors of the Jacobian in terms of these average quantities. The second step is decomposing the jumps across the discontinuity in terms of the eigenvectors, $\boldsymbol{K}_i$ as $\Delta \boldsymbol{U} = \sum_{i=1}^{4} \alpha_i \boldsymbol{K}_i$, and finding the weights α in terms of the averaged quantities. The last step is finding the average quantities that satisfy the flux-difference formula. The Jacobian $\boldsymbol{A}$ for the perturbation equations can be written as:

$$\boldsymbol{A} = \begin{bmatrix} 0 & 1 & 0 & 0 \\ -\frac{(3-\gamma)}{2}U^2 & (3-\gamma)U & 0 & \gamma - 1 \\ 0 & 0 & u & 0 \\ -U\left(\frac{H}{\rho} - \frac{\gamma-1}{2}U^2\right) & \frac{H}{\rho} - (\gamma-1)U^2 & 0 & \gamma U \end{bmatrix}, \tag{29}$$

where

$$\frac{H}{\rho} = \frac{a^2}{\gamma - 1} + \frac{U^2}{2}; \;\; a^2 = \frac{\gamma P}{\rho}. \tag{30}$$

The eigenvalues are found to be: $\lambda = \{U - a,\ U,\ U,\ U + a\}$ and the eigenvectors are:

$$\boldsymbol{K} = \begin{array}{cccc} k_1 & k_2 & k_3 & k_4 \\ 1 & 1 & 0 & 1 \\ U - a & 0 & 0 & U + a \\ 0 & 0 & 1 & 0 \\ \frac{H}{\rho} - Ua & \frac{U^2}{2} & 0 & \frac{H}{\rho} + Ua \end{array} \tag{31}$$

Proceeding onto the second step of calculating the wave strengths, a system of four algebraic equations for α_i in terms of $\Delta \boldsymbol{U}$ is formed:

$$\Delta \boldsymbol{U} = \sum_{i=1}^{4} \alpha_i \boldsymbol{K}_{\boldsymbol{i}} \,. \tag{32}$$

The solution to the system yields the perturbation weights, which are given as:

$$\alpha_2 = \frac{\gamma - 1}{a_a^2}\left[\Delta u_1 \left(\frac{H_a}{\rho_a} - U_a^2\right) + U_a \Delta u_2 - \Delta u_4\right] \tag{33}$$

$$\alpha_1 = \frac{1}{2a_a}\left[\Delta u_1 (U_a + a_a) - \Delta u_2 - a_a \alpha_2\right] \tag{34}$$

$$\alpha_4 = \Delta u_1 - (\alpha_1 + \alpha_2) \tag{35}$$

$$\alpha_3 = \Delta u_3 \ , \tag{36}$$

where the subscript on the base radial velocity U_a is used to denote an average between the right and left states.

Notice that the Jacobian obtained here is the same as that for the regular quasi-linearized Euler equations (governing equations of the base flow); therefore, the form of the eigenvalues and eigenvectors are the same as in the Roe-Pike analysis of the Euler equations. The equations obtained for the perturbation weights α have the same form as that of nonlinear Euler equations (Toro, 2009). However here, $\Delta\boldsymbol{U}$ denotes the perturbation's jump across the discontinuity rather than the base flow's jump. Roe-Pike also presented an approximate formula for the weights in terms of the characteristic variables; it is possible to derive such an approximate formula for the perturbation equations as well by writing:

$$\Delta\widetilde{\varrho u} = \varrho_a \Delta\tilde{u} + U_a \Delta\tilde{\rho} + E_m \tag{37}$$

$$\Delta\left(\widetilde{\varrho u^2}\right) = U_a^2 \Delta\tilde{\rho} + 2\varrho_a U_a \Delta\tilde{u} + E_e \ , \tag{38}$$

where the momentum error E_m and the energy error E_e are given by:

$$E_m = [(\varrho_R - \varrho_a)\tilde{u}_R - (\varrho_L - \varrho_a)\tilde{u}_L] + [\tilde{\varrho}_R(U_R - U_a) - \tilde{\varrho}_L(U_L - U_a)] \tag{39}$$

$$\begin{gathered} E_e = [\tilde{\varrho}_R(U_R^2 - U_a^2) - \tilde{\varrho}_L(U_L^2 - U_a^2)] + \\ 2[\ \tilde{u}_R(\ \rho_R U_R - \varrho_a U_a) - \tilde{u}_L(\ \rho_L U_L - \varrho_a U_a)\ ] \ . \end{gathered} \tag{40}$$

The subscripts *L, R* are used to indicate the left and right states respectively. In this case, the approximate weights are written in terms of the perturbation characteristic variables:

$$\alpha_1 = \frac{1}{2a_a^2}[\Delta\tilde{p} - \varrho_a U_a \Delta\tilde{u}] \tag{41}$$

$$\alpha_2 = \Delta\tilde{\rho} - \frac{\Delta\tilde{p}}{a_a^2} \tag{42}$$

$$\alpha_3 = \varrho_a \, \Delta\tilde{q} \tag{43}$$

$$\alpha_4 = \frac{1}{2a_a^2}[\Delta\tilde{p} + \varrho_a U_a \Delta\tilde{u}] \ . \tag{44}$$

Again the rewritten weights are identical in form to the weights obtained by Roe-Pike (Toro, 2009), except the difference between the right and left state is the difference in perturbation quantity rather than the base quantity. For either form of the perturbation weights, the „averaged' base flow quantities are determined such that the flux difference equation is satisfied.

$$\Delta \boldsymbol{F} = \sum_{i=1}^{4} \alpha_i \lambda_i \boldsymbol{K}_i \ . \tag{45}$$

For the base flow's weights, Roe and Pike showed that the approximate characteristic weights satisfy the flux difference equation for any definition of an average. In other words, so long as the averaged value falls between the right and left values the flux difference is satisfied. Upon repeating the same process for the perturbation characteristic weights, the conclusion is the same. Unlike the approximate characteristic weights, the more accurate weights demand that the average be defined as:

$$\rho_a = \sqrt{\rho_R \rho_L} \tag{46}$$

$$U_a = \frac{\sqrt{\rho_R} U_L + \sqrt{\rho_L} U_R}{\sqrt{\rho_R} + \sqrt{\rho_L}} \ . \tag{47}$$

The remaining averaged parameters are computed in a similar fashion. Now that flux difference is computed, the flux at the face $\boldsymbol{F}_F$ can be evaluated by:

$$\boldsymbol{F}_F = \frac{1}{2} (\boldsymbol{F}_L + \boldsymbol{F}_R) - \frac{1}{2} \Delta \boldsymbol{F} \ . \tag{48}$$

Notice that the perturbation equations' Jacobian was directly given in terms of only the base flow. Therefore, no additional approximation was needed. This is no surprise because the perturbation system was already linear, so there was no need for a quasi-linear form.

2.3.2. Inner Boundary Numerical Implementation

At the inner boundary $r = 0$, solely by requiring that $U = 0$, $\tilde{u} = 0$, and that $\tilde{q}$ is nonsingular, the fluxes at the face reduce to:

$$\boldsymbol{F} = \begin{Bmatrix} \tilde{\rho} U + \varrho \tilde{u} \\ 2Uu_2 - \tilde{\rho} U^2 + \tilde{p} \\ Uu_3 \\ \tilde{u} H + U \tilde{H} \end{Bmatrix} \rightarrow \begin{Bmatrix} 0 \\ \tilde{p} \\ 0 \\ 0 \end{Bmatrix} \ . \tag{49}$$

The condition that the gradient of the perturbation pressure is zero is enforced through the flux, since the pressure at the face $r = 0$ is set equal to the cell centered value at $r = \Delta r/2$. The

singularity is removed by refraining from solving the $\tilde{q}$-equation at the first node; instead, we specify $\tilde{q}$ at the first node as $\tilde{q} = 2\tilde{u}/\lambda$.

2.4. Results and Discussion

We first present the results for a specific case of a spherical container with an inside to ambient pressure ratio of 22 and a temperature ratio of 1. For simplicity we consider both the compressed gas and the ambient to be air with an adiabatic index γ of 1.4. Correspondingly the initial inside to ambient density ratio is also 22. The ambient temperature and pressure are taken to be 299°K and 1.0207 atm respectively. The initial location of the diaphragm r_o was 0.0254 m. These operational parameters were chosen because several other prior studies have used the same spherical shock tube condition, since the earliest work by Brode [20] and Freidman [18]. For this case we first briefly review the results of the base flow and then proceed to discuss the instability results and compare the numerical results with the different theoretical predictions. Once the comparison is firmly established we then generalize to consider a wider range of pressure and density ratios.

All the results presented herein are normalized as follows: the length scale is chosen to be the initial location of the spherical diaphragm separating the high pressure gas from the ambient air, thus a dimensionless radial coordinate can be defined as $\xi = r/r_o$. The velocity and density are normalized by the ambient speed of sound and density respectively. The time scale τ is formed from the ambient speed of sound and the initial location of the diaphragm, hence the dimensionless time is obtained as $\tau = (t\,a)/r_o$. Lastly, the pressure and total energy are normalized by ρa^2, where ρ and a are the density and speed of sound of the undisturbed ambient.

2.4.1. The Base Flow

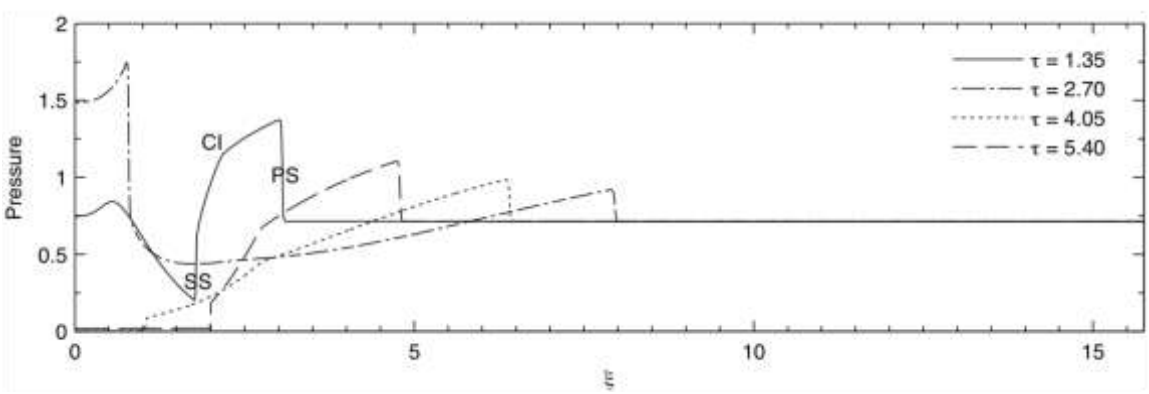

1a

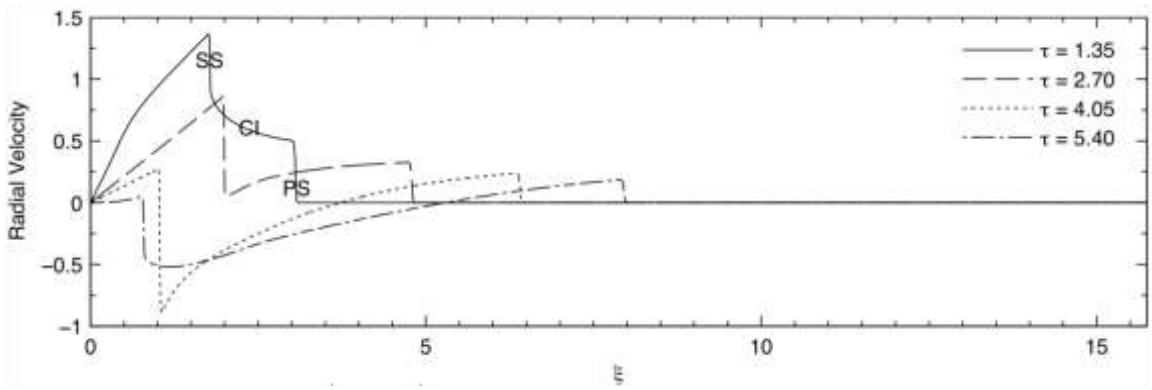

1b

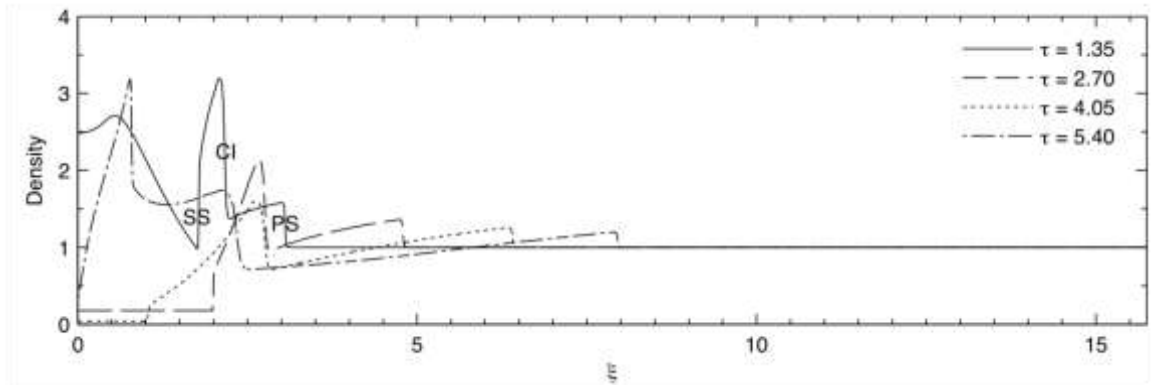

1c

Figure 2–1. The radial dependence of (1a) pressure, (1b) radial velocity, and (1c) density of the base flow at 4 different non-dimensional times. The location of the primary shock (PS), secondary shock (SS) and contact interface (CI) are most evident in the density profile and are marked. The above results are obtained with a discretization of 2000 uniform grid points extending up to a radial location of ξ = 15.75.

Figure 2–1 shows the dimensionless pressure, velocity, and density of the base flow as a function of ξ at various times. The pressure and velocity jumps across both the primary shock (PS) and the secondary shock (SS) are clear in Figure 2–1a and Figure 2–1b respectively. The pressure and velocity are continuous across the contact interface (CI), but the density is discontinuous, which is evident in Figure 2–1c. The primary shock moves only in the forward direction, while the secondary shock initially moves outward, then inwards, and finally reflects off the origin. The location of the maximum density derivative is used as an estimate for the contact interface's position denoted by R_{CI}.

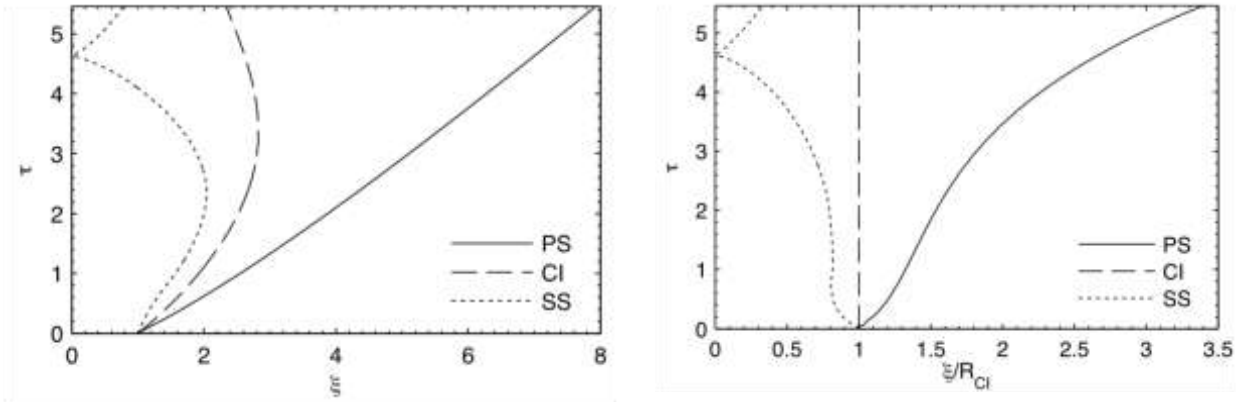

2a **2b**

Figure 2–2. ξ- τ Diagram of the location of the contact interface, primary shock, and secondary shock. In terms of the original non-dimensional location (2a), and rescaled by the location of the contact interface (2b).

Figure 2–2 depicts the location of the discontinuities as a function of time. As shown in Figure 2–2a, during the time range [0, 4] the contact interface's path is approximately parabolic, which suggests a constant deceleration of the CI that is explored in detail later on. The secondary shock's first reflection happens at a dimensionless time, $\tau = 4.6$. Once the SS is reflected it continues to move outward until it interacts with the CI creating a tertiary shock, while undergoing Richtmyer-Meshkov (RM) instability (Richtmyer, 1060; and Meshkov (1969). For now, we focus on studying the non-classical RT instability of the CI, before its interaction with the secondary shock. Therefore, the time domain of interest is up to $\tau = 5.4$ in order to isolate the non-classical RT mechanism from the RM mechanism. In Figure 2–2b, we normalize the radial distances by the location of the CI, thus showing the location of the shocks relative to the CI. It is clear that the secondary shock for an extended duration remains close to the contact at about 80% of its radial location; even the primary shock till about $\tau = 3.3$ remains within one radius of the contact's location. Thus, it is of interest to study how the non-classical RT instability of the CI is influenced by the presence of the two nearby shocks.

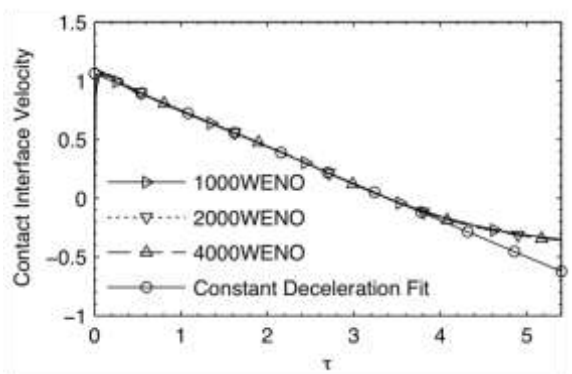

Figure 2–3. The constant deceleration of the CI and its grid independence.

The velocity of the contact interface and its grid independence are shown in Figure 2–3. Note that the CI's velocity goes to zero around $\tau = 3.5$. From the figure, the deceleration of the contact interface appears to be a constant for the range of $\tau = 0.0$ to about 4.0. Interestingly, this time range coincides with the inward motion of the secondary shock. Once the secondary shock reflects off the origin the inward acceleration of the CI begins to slow down. Also in Figure 2–3, we demonstrate the effect of the numerical grid resolution on the extracted deceleration. Results for three different resolutions ranging from 1000 to 4000 uniform grid points resolving a region of $0 < \xi < 15.75$ are shown in the figure and it is

evident that the velocity of the CI rapidly becomes grid-independent.

The convergence of the base flow with increasing numerical resolution is critical when studying the behavior of the perturbation. This is particularly important in the present context of non-classical RT instability, which depends on the sharpness of the interface. Figure 2–4 illustrates the effect of refining the computational grid on the mean flow parameters relevant to the growth rate of the instability. The two parameters presented in the figure are the Atwood number and the finite thickness of the contact interface. The Atwood number is computed by finding the local maxima and the local minima of the density. The narrow region between the locations of these two local extrema is defined as the thickness of the contact interface. It is clear that the Atwood number converges to its asymptotic value with increasing resolution. Furthermore, it is very interesting that the Atwood number remains nearly a constant during the time period of investigation. In comparison, the convergence of the width of the contact interface is slower. This phenomenon is typical of discontinuity-capturing numerical approaches, because the width of the discontinuity is limited by the grid spacing and thus convergence is at best first order. The resulting finite thickness of the contact interface will have an impact on the growth rate of the instability and this effect is investigated in detail.

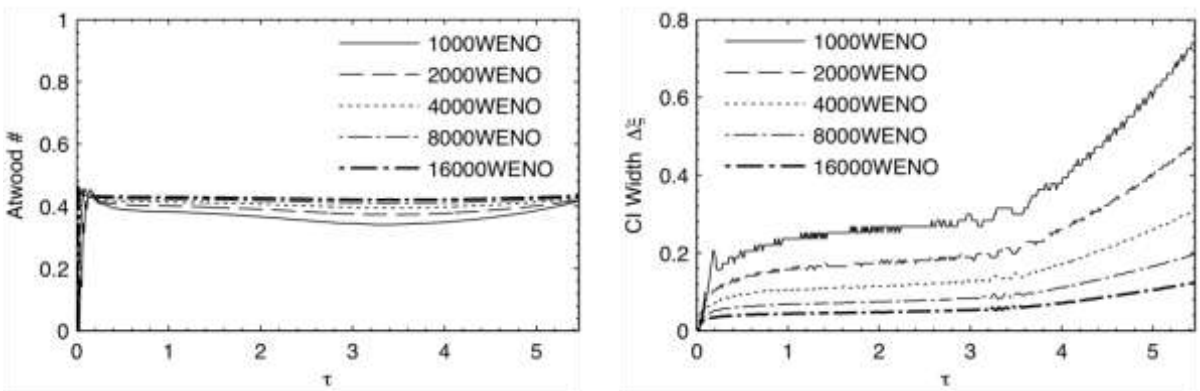

4a **4b**

Figure 2–4. Grid Study of base flow parameters Atwood number and the CI width.

2.4.2. The Perturbation Solution

In this section we present results on the spatial and temporal structure of the perturbation resulting from the instability analysis. It must first be emphasized that the present approach is an initial value formulation and not an eigenvalue problem. Since the base flow, whose stability is being investigated, is a function of both time and ξ, the governing equations for the perturbation (22)-(25) remain dependent on both time and ξ. Here we solve these equations along with the base flow equations starting from an assumed initial perturbation structure. The two disadvantages of the initial value approach are that a system of partial differential equations must be solved for the perturbation and that the computed time evolution of the perturbation depends on its assumed initial structure.

For the results presented in this section, the perturbation density was initialized with a Gaussian distribution with a peak density perturbation chosen to be 0.1% of the initial density of the inner high pressure fluid. The distribution is centered at the initial location of the spherical diaphragm, $\xi = 1$. The width of the Gaussian distribution is chosen such that it decays to 1% within 30% of the radial location. Fortunately, as will be discussed in section 5.3, the growth of the disturbance

is quite insensitive to a broad class of initial perturbation profiles, thus allowing general conclusions about the instability, without being dependent on the details of the initial perturbation. Thus, the results to be presented below on the spatial structure of the perturbation profile can be taken to be generic. The perturbation results presented below are for a specific spherical wave number of $n = 40$ and the results for other values of n are qualitatively similar.

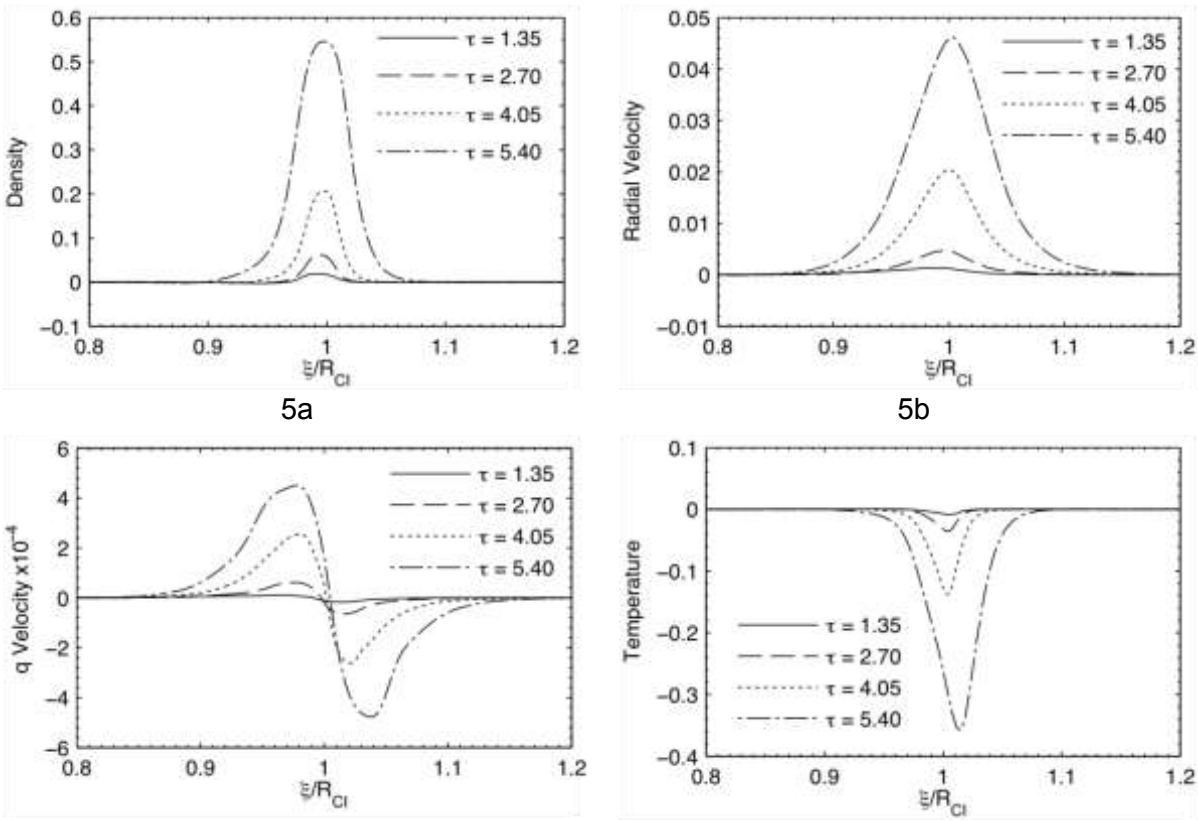

5a 5b

5c 5d

Figure 2–5. The radial structure of the perturbed flow's density, radial velocity, tangential velocity, and temperature eigen modes for $\mathbf{n} = 40$.

The radial profile of the perturbation is presented in Figure 2–5 for four different times. The perturbation density and velocity have a Gaussian-like profile. Over time their peaks remain approximately aligned with the location of the contact interface (note that if plotted against unscaled ξ the disturbance will appear to move and grow with the CI). The tangential velocity switches sign around the CI and is of much smaller amplitude than the radial velocity. These two features of the tangential velocity are physically consistent with the large value of the spherical wave number and the Gaussian-like profile of the perturbation radial velocity. Thus, the structure of the radial and tangential velocity components yield pairs of vertical tubes centered about the spherical contact interface. It is observed that the pressure perturbation is quite small (i.e., $\tilde{p}/P \sim 0$) and as a result $\tilde{T}/T \approx -\tilde{\rho}/\rho$ and thus the radial distribution of temperature perturbation resembles that of density. From (25) the total energy perturbation can be expressed as, $\tilde{E} \approx \rho U \tilde{u} + 3\tilde{\rho} U^2/2$, and thus takes a somewhat more complex radial structure than the perturbation temperature.

The dependence of perturbation structure on spherical wave number is shown in Figure 2–6a, where radial velocity perturbation is plotted against scaled radial location at $\tau = 2$ for five different values of n. As can be expected the thickness of the disturbance along the radial direction decreases with increasing spherical wave number. For $n = 4$, the disturbance decays slowly away from the CI and remains non-zero as it extends to the primary and secondary shocks, which are located at $0.8\mathrm{R_{CI}}$ and $1.5\mathrm{R_{CI}}$ respectively. In fact the interaction of the disturbance with the secondary shock can be seen to locally enhance the disturbance around $0.8\mathrm{R_{CI}}$. For n greater than about 20 the disturbance decays sufficiently rapidly that it can be considered to be isolated from direct interactions with the primary and secondary shocks. For large values of the spherical wave number the disturbance structure appears to reach an asymptotic structure and not scale inversely with n. This is an effect of the finite resolution of the base flow depicted in Figure 2–6b. Notice that width of the contact interface in Figure 2–6b is almost the same as the width of the radial velocity distribution for $n = 537$ in Figure 2–6a. Only for an infinitely thin contact interface (true contact discontinuity), and with adequate resolution, the perturbation thickness will continue to decrease with n.

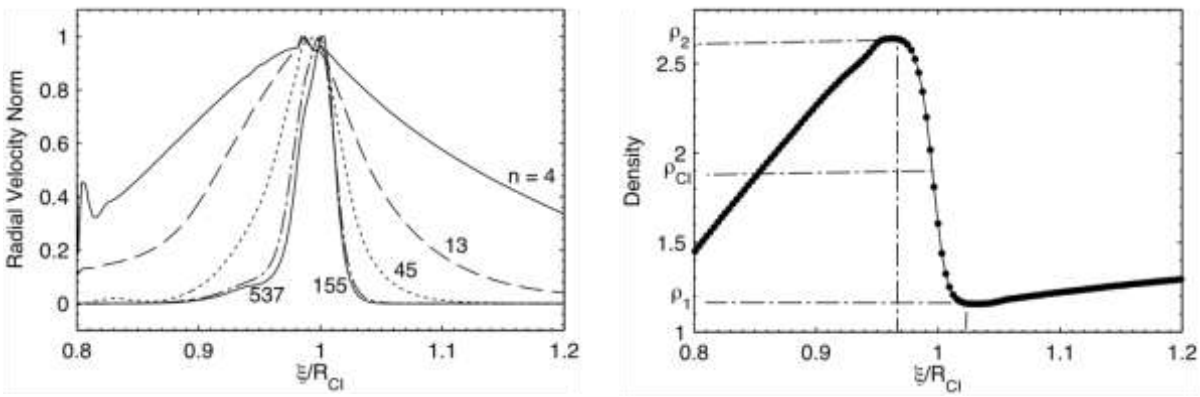

6a 6b

Figure 2–6. Dependence of perturbation structure on spherical wave number (6a) and the finite width of the Contact Interface (6b).

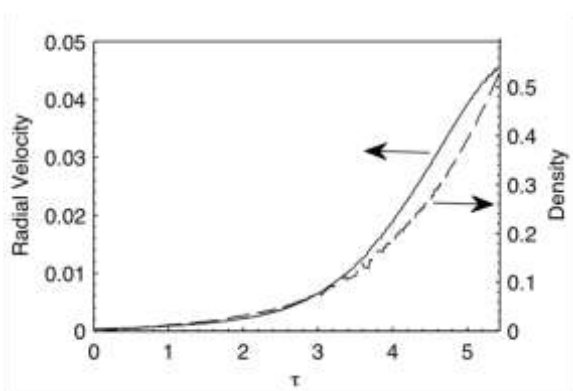

Figure 2–7. Peak perturbation density and radial velocity growth over time.

Figure 2–7 represents the growth in time of the peak density and radial velocity perturbation. The growth appears to be exponential over the time range of [1.0 4.0] (to be established below in section 5.3). Notice that the growth of the disturbance remains smooth and continuous starting from $\tau = 0.0$, and the exponential growth appears to be valid from the start without much transient behavior. This suggests that the initial Gaussian disturbance is quite close to the true exponentially growing perturbation and that the initial adjustment is quite small and rapid. The slight oscillation in the perturbation density amplitude seen in Figure 2–7 around $\tau = 3.5$ is

not due to physical phenomenon; instead it is caused by post processing. We have used an automated interface tracking technique to identify the location of the contact interface and extract the perturbation properties there. This automated tracking becomes sensitive when the contact interface changes direction (i.e., when the contact interface velocity is close to zero) and the location numerically alternates between two adjacent nodes. This effect is more evident in Figure 2–4b in the plots of CI's width. As can be expected this fluctuation decreases with increasing resolution, and can be removed by more sophisticated post-processing. This was not pursued since it has little effect on the results to be discussed below.

2.4.3. The Effect of the Perturbation's Initial Condition on the Amplification Rate

We attempt herein to clarify the nature of the growth rate and its dependence on the initial disturbance. Since our focus is on the instability of the CI, we choose to start with an initial disturbance that is centered on the CI. For the range of parameters considered here the primary shock is always stable; consequently, any disturbance that leaks from the CI towards the primary shock rapidly decays. On the other hand, the secondary shock is initially stabile but becomes unstable as it collapses towards the origin. Once it reflects off the origin, its stability behaves in the same fashion as the primary shock. In general as shown in Figure 2–6a, during the initial period of interest here, for sufficiently large n the presence of the PS and SS does not influence the non-classical RT instability of the CI. Past this duration of interest, the reflected secondary shock interacts with the CI and leads to RM instability.

For the present study, the growth rate is obtained from the time evolution of the following volume integral of the perturbation:

$$\mathrm{I}(\tau) = \int_{0.85\mathrm{R_{CI}}}^{1.15\mathrm{R_{CI}}} \tilde{u}^2(\xi,\tau)\xi^2 d\xi \tag{50}$$

It can be thought of as the integrated kinetic energy contribution strictly from the perturbation radial velocity localized around the contact interface.

Figure 2–8a plots $\mathrm{I}(\tau)$ for various initial perturbations in order to establish the independence of the disturbance growth rate from the initial condition. The perturbed flow is governed by a linear system; therefore, the results should simply scale with the initial amplitude of the disturbance, and as such some of the curves were shifted for presentation purposes. The independence of the growth rate from the initial condition is established by comparing $\mathrm{I}(\tau)$ for five different types of initial disturbances:

- An initial parabolic perturbation in density alone with a maximum at the CI , while the rest of the initial disturbance quantities are set to zero.
- An initial Gaussian perturbation in density alone centered on the CI.
- An initial Gaussian perturbation in the total energy alone centered on the CI.
- An initial Gaussian perturbation in the radial velocity alone centered on the CI.
- Gaussian disturbances are introduced in both the density and total energy, again the remaining disturbance quantities are set to zero.

All the five cases share a common pattern: first the disturbance grows very rapidly over a short initial period of $\tau < 0.5$. This initial period of rapid growth is followed by an extended period of exponential growth that lasts to about $\tau = 4.0$, and is characterized by the straight segment in the log-linear plot.

Notice the initial adjustment time is minimal for case 2 where the disturbance introduced is only in the density and of Gaussian shape. Also for case 4, since the asymptotic structure of the radial velocity disturbance is also Gaussian-like, only a slight initial adjustment is required. For cases 3 and 5, a Gaussian profile for the initial perturbation energy is not appropriate as it substantially deviates from its asymptotic structure. As a result, the time evolution of the integrated perturbation shows large initial oscillation before entraining into the exponential growth period.

Also note that the definition of $I(\tau)$ based on the integrated radial velocity squared is not a unique choice for evaluating the growth rate. Figure 2–8b also depicts the growth rate when calculated based on the integrated density squared rather than radial velocity. As expected from linear theory the growth rate is almost the same.

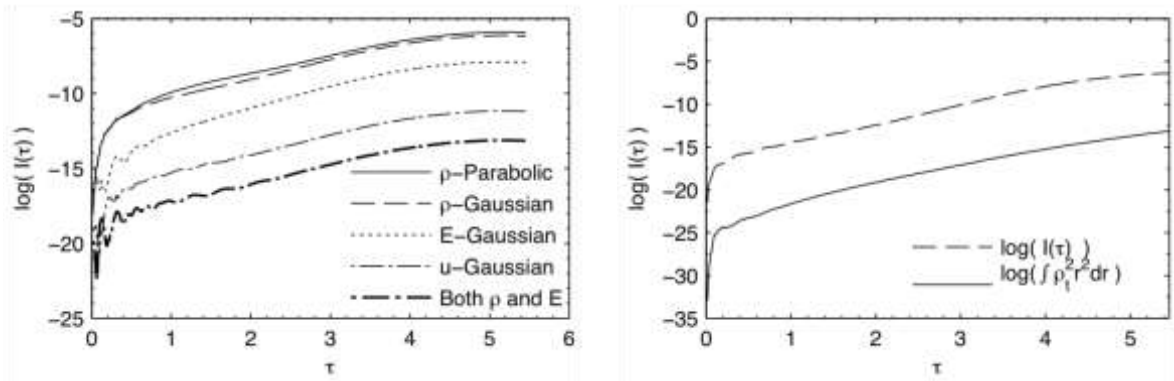

8a 8b

Figure 2–8. The effect of the initial spatial profile on the computed growth rate (8a) and calculating the growth rate based on the radial integration of a variable squared (8b).

An important conclusion drawn from the figure is that there exists an asymptotic eigen structure for the exponentially growing disturbance. Provided the initial disturbance is close to this eigen structure the perturbation enters the exponential growth period with minimal initial adjustment. This allows an exponential growth rate to be defined as a function of the spherical wave number n, independent of the shape and structure of the initial disturbance.

When analyzing the stability of self-similar spherically expanding base flows, the disturbance growth was shown to follow a power-law (Ryu and Vishniac, 1987). We notice here that the growth rate is nearly exponential over an extended time interval. Over this time period, the contact interface's deceleration and Atwood number exhibit a near constant behavior thus allowing an exponential disturbance growth (see Figure 2–3 and Figure 2–4a).

2.4.4. Effect of the Spherical Wave Number on the Growth Rate

During the intermediate period of near constant exponential growth, Figure 2–9 presents the dependence of growth rate on the spherical harmonic wave number. At low wave numbers the growth rate increases as $\sqrt{n}$, but with increasing n the corresponding increase in growth rate slows down and eventually for sufficiently large spherical wave numbers it reaches a constant

value. Also, shown in the figure are the growth rates obtained at five different grid resolutions employed for both the base flow and the perturbation. Also plotted for reference is a line representing the $\sqrt{n}$ increase in growth rate.

Three different wave number regimes with different behaviors can be observed. For small values of n we observe significant departure from the $\sqrt{n}$ increase in growth rate with wave number. This departure is expected, since for such small n the disturbance is quite thick in the radial direction (see Figure 2–6a) and begins to interact with the adjacent shocks. Over this thickness the base state shows considerable variation on either side of the CI, thus contributing to departure from non-classical RT instability. Furthermore, there is additional disturbance growth around the secondary shock (see Figure 2–6a) that interacts with contact interface. The RM instability effects begin to corrupt the estimation of the volume integral of the perturbation as defined in (50) and the resulting growth rate. Nevertheless, the computed growth rates are independent of the grid resolution employed for both the base and perturbation flows.

In the intermediate wave number regime, the growth rate increases as $\sqrt{n}$ and the width of this intermediate regime increases with increasing grid resolution. A grid resolution of 1000 uniform grid points over a domain of $0 < \xi < 15.75$ is adequate to extract grid independent growth rate for $n < 6$ while with a much finer resolution of 8000 grid points we obtain reasonable convergence for $n < 30$, with increasing resolution the $\sqrt{n}$ increase in growth rate can be expected to extend to an even wider range of spherical wave numbers.

This numerical behavior is related to the dependence of the base flow solution on the grid, as shown in Figure 2–3 and Figure 2–4. Although the deceleration of the CI and the Atwood number computed across it reach adequate convergence, as discussed in section 5.1, the thickness of the contact interface remains finite at any level of resolution. Provided the radial width of the perturbation (as shown in Figure 2–6) is much larger than the thickness of the CI, the perturbation sees the CI as a near discontinuity and the perturbation growth rate increases as $\sqrt{n}$. With increasing n, since the radial penetration of the perturbation around the CI narrows, the finite thickness of the contact interface cannot be ignored and the increase in growth rate with n slows down.

For large n the length scale of the perturbation becomes smaller than the finite thickness of the CI. As will be shown later in this report, in this regime the growth rate can be expected to be independent of n and depend only on the gradients of density and pressure across the finite thickness of the CI. With increasing resolution we observe this numerically influenced asymptotic constant growth rate regime to be postponed to larger n. Furthermore, the asymptotic constant growth rate increases with increasing resolution, since the density gradient within the CI increases as its finite thickness decreases.

With the inclusion of viscous and diffusive effects the perturbation growth rate will decrease for large n and the most amplified spherical harmonic can be identified. Furthermore, since the viscous and diffusive effects well define the finite thickness of the CI, a precise finite resolution requirement can be stated for accurate grid-independent prediction of the growth rate. However, in the present case of inviscid analysis, since there is no finite length scale for the discontinuous CI, a definite limiting numerical resolution cannot be achieved.

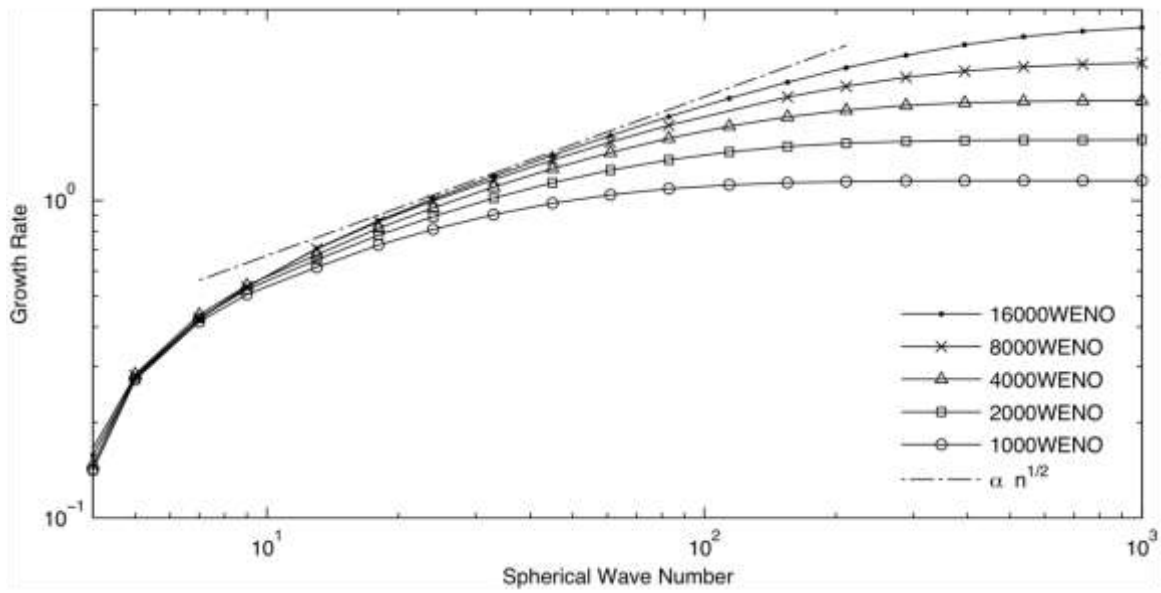

Figure 2–9. The global growth rate vs. the wave number for various resolutions.

2.4.5. Comparison with Theoretical Models

To establish the validity of the computed instability results, we compare our results with previous theoretical models. In order to identify the mechanisms involved we consider different theoretical models that systematically include the effects of spherical geometry, compressibility, unsteady effects, and the finite thickness of the interface. Before we proceed to compare the theoretical and computed results we briefly summarize the theoretical results to be considered.

2.4.5.1. Incompressible Planar RT Instability

Taylor (1950) considered two incompressible fluids separated by a planar interface. The density is discontinuous across the interface and the system is subjected to a gravitational acceleration, g. Taylor established the perturbation amplitude $a(t)$ to grow exponentially as:

$$a(t) = a(0)exp(\sigma_{Ta}\, t)\,. \tag{51}$$

Here $a(0)$ is the initial amplitude and the planar growth rate is given by

$$\textbf{Taylor}:\ \ \sigma_{Ta} = \sqrt{k\, At\, g}\ , \tag{52}$$

where k is the planar wave number and At is the Atwood number:

$$At = \frac{\varrho_2 - \varrho_1}{\varrho_2 + \varrho_1}\ , \tag{53}$$

where the subscripts 1 and 2 refer to the outside and inside of the contact interface. In order to compare Taylor's planar results with the present spherical problem several considerations must

be made. First, Taylor's formulation is for a constant Atwood number. As shown in Figure 2–4 the computed Atwood number is nearly a constant over an extended time interval, from which an average Atwood number is computed to evaluate the growth rate. For the planar case, the wave number has a dimension of one over length, but the spherical wave number is dimensionless. To facilitate comparison, the two are taken to be related by $k = n/\mathrm{R_{CI}}$, where $\mathrm{R_{CI}}$ is the radius of the CI. Again $\mathrm{R_{CI}}$ varies in time as a parabola, however, a time averaged value for $\mathrm{R_{CI}}$ is used. In the recent work by Epstein (2004), it was shown that for an accelerating interface g must be taken to be equal to the pressure gradient scaled by the density at the interface

$$g = g_p = -\left[\frac{1}{\varrho}\frac{\partial P}{\partial r}\right]_{CI} \tag{54}$$

Note that the density and pressure gradients are both discontinuous across the contact interface, but g_p is continuous. Due to the finite thickness of the CI, the value of discontinuous quantities on either side of the interface and the value of continuous quantities must be appropriately evaluated. If we refer to Figure 2–6b, densities ρ_1 and ρ_2 outside and inside of the interface are defined as the local minimum and maximum adjacent to the interface. The finite thickness of the interface is defined to be the distance between these two locations. Quantities at the interface $[.]_{\mathrm{CI}}$ are evaluated at the midpoint between the local extrema which is observed to be approximately the same as averaging across the width of the interface. In our simulations, g_p is observed to be nearly equal to the acceleration of the contact interface $\ddot{\mathrm{R}}_{\mathrm{CI}}$.

2.4.5.2. Compressible and Incompressible Spherical RT instability

Here we present Epstein's (2004) elegant formulation that clearly highlights the classical RT instability from the BP effect, while accounting for the compressibility of the base flow by allowing the density on either side of the interface to vary in time. The perturbation is taken to be incompressible. As in the original formulation of Plesset (1954) the time evolution of the perturbation amplitude is governed by a second-order differential equation:

$$\textbf{Epstein} - \textbf{ODE}: \quad \left(-\sigma_\varrho - \sigma_R + \frac{d}{dt}\right)\frac{d(a\varrho {\mathrm{R_{CI}}}^2)}{dt} = \sigma_o^2\, a\varrho {\mathrm{R_{CI}}}^2 \tag{55}$$

where

$$\sigma_0^2 = \frac{n(n+1)}{R}\,\frac{\rho_2 - \rho_1}{n\varrho_2 + (n+1)\varrho_1}\; g_p \tag{56}$$

$$\sigma_\varrho = \frac{1}{\varrho_1}\frac{\partial \varrho_1}{\partial t} = \frac{1}{\varrho_2}\frac{\partial \varrho_2}{\partial t}\ , \quad \sigma_R = \frac{\dot{\mathrm{R}}_{\mathrm{CI}}}{\mathrm{R_{CI}}}\ . \tag{57}$$

In equation (56), g_p is the same as given in (54), σ_ϱ and σ_R account for the compressibility and the convergence (geometric) effects, while σ_0 accounts for the RT instability. The solution for

the above differential equation can be obtained for any arbitrary time-dependent contact interface, where σ_ϱ, σ_R and σ_0 are functions of time. In applying this theoretical formulation to the computed base flow, we take σ_ϱ to be the average value obtained from the either side of the CI, which are approximately equal for our problem. We observe the solution to the above ordinary differential equation nearly follows an exponential growth during the intermediate time period of interest. From which an average growth rate can be evaluated and for the purpose of comparison we will denote this theoretical growth rate to be **Epstein-ODE**.

An explicit expression for the growth rate can be obtained from (55) if the compressibility, convergence and RT parameters (σ_ϱ, σ_R and σ_0) are constants. In this limit, Epstein (2004) obtained the growth rate to be

$$\textbf{Epstein}: \quad \sigma_{Ep} = \frac{1}{2}\left(\sigma_\varrho + \sigma_R\right) \pm \sqrt{\sigma_o^2 + \frac{1}{4}\left(\sigma_\varrho + \sigma_R\right)^2} \ . \tag{58}$$

It is easier to present the original incompressible analysis of Plesset (1954) in terms of the above formulation by Epstein (2004). The incompressibility limit of Plesset can be obtained by setting the compressibility effect to zero (i.e. $\sigma_\varrho = 0$) in (55). Thus, the time evolution of the incompressible perturbation is also governed by a second order differential equation. Again, an explicit expression for the growth rate can be obtained if σ_R and σ_0 are constants and the resulting growth can be expressed as

$$\textbf{Plesset}: \quad \sigma_{Pl} = \frac{\sigma_R}{2} \pm \sqrt{\sigma_o^2 + \frac{\sigma_R^2}{4}} \ . \tag{59}$$

2.4.5.3. Incompressible RT Instability of an Interface of Finite Thickness

In 1998, the effect of finite thickness of the interface in the incompressible planar context was considered by Lind l(1998). The configuration was the same as that of Taylor (1950), however instead of a discontinuous change in density across the interface, Lindl assumed the density to vary exponentially in space across the interface. In other words, in Lindl's analysis both the width and the density gradient across the contact interface are finite. In this case the modified growth rate was obtained to be:

$$\textbf{Lindl}: \quad \sigma_{Li} = \sqrt{\frac{k\ At\ g_p}{1 + k\ At\ L}} \tag{60}$$

where L is the density gradient length scale across the interface, which is equivalent to the thickness of the contact interface. Again k will need to be approximated by $k = n/R_{CI}$.

2.4.5.4. Local Compressible Convective Instability of a Finite Interface

The instability of the contact interface of finite thickness can also be considered as a convective instability arising from density stratification. The general Schwarzschild criterion for convective instability in a compressible medium can be easily derived and can be expressed as $\mathcal{R}/\mathcal{P} < 1/\gamma$, where $\mathcal{P} = \partial lnP/\partial r$ and $\mathcal{R} = \partial ln\rho/\partial r$. In general, across a contact interface of finite thickness both $\mathcal{P}$ and $\mathcal{R}$ will vary with position thus the above criterion must be interpreted as local instability criterion. The corresponding criterion for instability in an incompressible flow can be expressed as $\mathcal{R}/\mathcal{P} < 0$ and thus in this context the effect of compressibility can be seen to be destabilizing. The local growth rate in the limit of large wave numbers can be written as (Bandiera, 1984):

$$\textbf{Bandiera}: \ \sigma_{sc} = \frac{c}{\gamma}\sqrt{\mathcal{P}^2 - \gamma\mathcal{P}\mathcal{R}} \tag{61}$$

where c is the speed of sound. In applying the above formula to estimate the growth rate of the perturbation we will use the average value of $\mathcal{P}$ and $\mathcal{R}$ evaluated across the interface and also use the outer speed of sound.

2.4.5.5. Comparison with Theories

A comparison of the computed growth rate with the various theoretical models discussed above is presented in Figure 2–10. The predictions of planar and spherical RT instability theories are generally close to each other indicating the relatively modest effects of compressibility and sphericity. The dominant feature of all these theories is the increase in growth rate as square root of the spherical wave number. The computed growth rate follows this scaling up to a wave numbers of about 40, beyond which the growth rate slows down and eventually saturates to a constant growth rate that is independent of the wave number. In the regime where growth rate is $\propto \sqrt{n}$ the solution to the compressible ODE by Epstein (2004) in equation (55) and its steady approximation (58) compare the best with the computed growth rate. This can be expected since Epstein's theory accounts for both compressibility and radial effects. Surprisingly Taylor's (1950) incompressible theory seems to do quite well. The growth rate predicated by Plesset (1954) is slightly higher than the rest. The effect of compressibility is to decrease the growth rate and as a result prediction by Plesset is higher than by Epstein. Interestingly, the radial effects work the other way and partly compensate for the compressibility effect. Thus, Taylor's theory that ignores both compressibility and radial effects compares better than Plesset's prediction.

The asymptotic constant growth rate computed for large wave numbers compares well with the local convective growth rate given by Bandiera (1984). At such large wave numbers the finite thickness of the contact interface computed in the base flow solution begins to have a strong influence. The interface does not appear as a discontinuity and the density gradient in conjunction with the local pressure gradient within the contact interface dictates the growth rate. Unlike classical RT instability, the convective instability given in (61) is independent of the spherical wave number. Figure 2–10 corresponds to a grid resolution of $N = 16000$ for both the base flow and perturbation solutions. The theory by Lindl (1998) follows both the low and large wave number behaviors. However, Lindl's prediction is based on incompressible analysis of a planar interface and is somewhat lower than the computed growth rate.

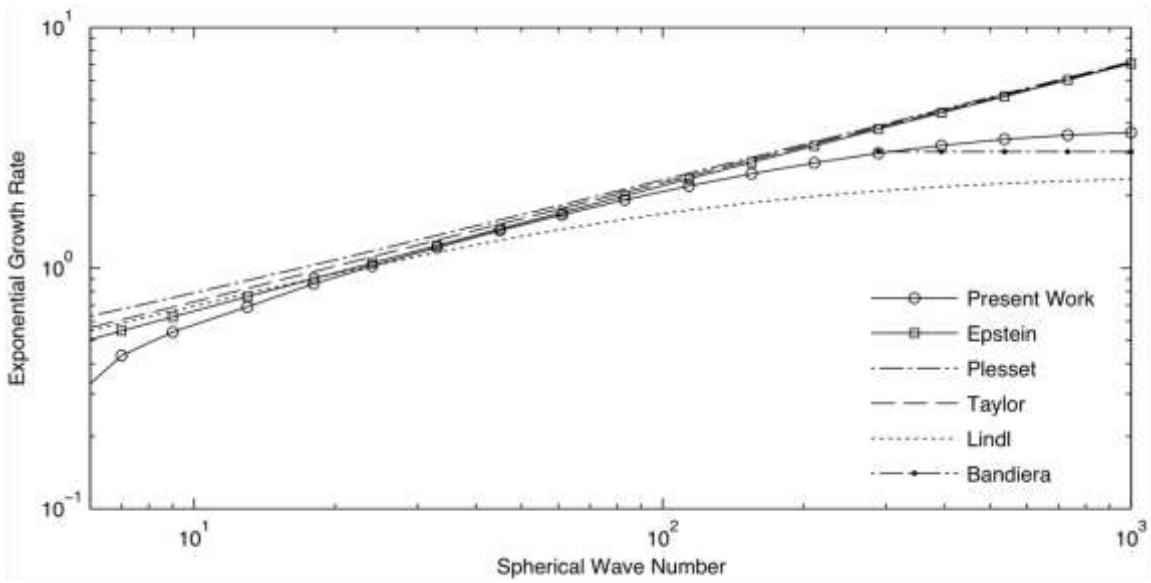

Figure 2–10. The effect of the wave number on the growth rate.

Figure 2–11 depicts the iso-surface of constant density for the contact interface a $\tau = 4.0$. The total density is obtained by adding the base flow density and the perturbation density. The latter is not only a function of time and r, but also a function of θ and φ. The iso-surface is shown for two specific cases Figure 2–11a $n = 45$ with $m = 7$ and Figure 2–11b $n = 9$ and $m = 7$. The wrinkling of the interface increases with time due to the exponential growth of the disturbances and is particularly evident at late times. The amplitude of the disturbance is however dependent on the arbitrary strength of the initial perturbation. The surfaces of the primary and secondary shocks are still purely spherical because they are stable. Note that the theory predicts the growth of the perturbation to depend only on n and independent of m. From experimental observation it can be expected that in the nonlinear regime the growth of the disturbance will depend on both n and m.

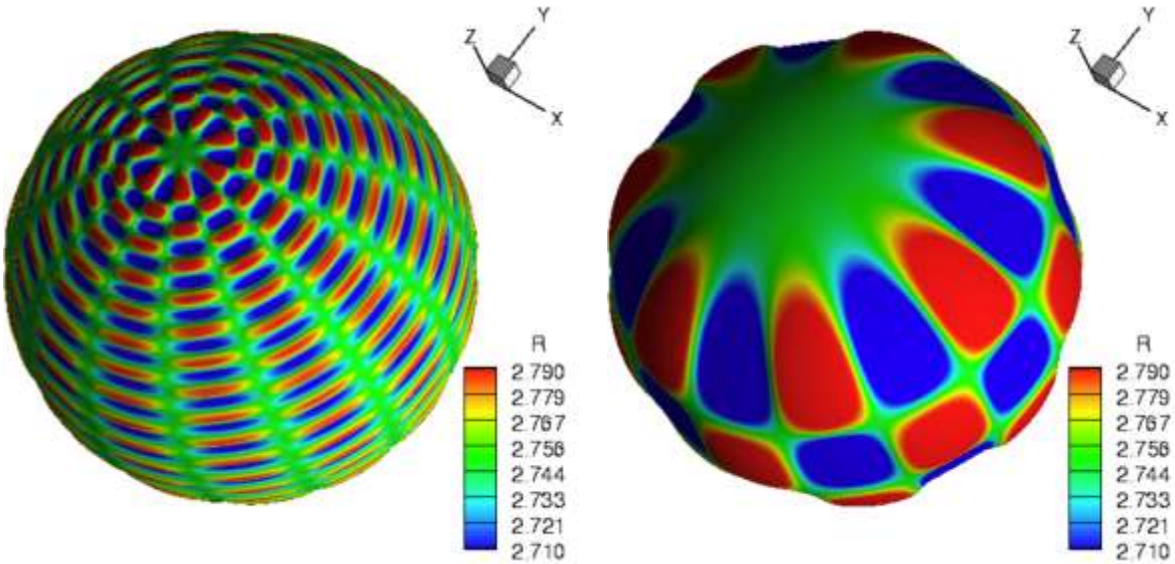

11a 11b

Figure 2–11. The Contact Interface for a wave number of $n = 45$ and a mode of $m = 7$ (11a) and for a wave number of $n = 9$ and mode of $m = 7$ (11b).

2.5. Parametric Study of the Instability

The purpose of the parametric study is to better understand the complicated mechanisms involved in predicting the instabilities. A better understanding will enable designers to control the instabilities, suppress or enhance them depending on the circumstances of the various applications. The problem of a spherical shock tube is characterized by two key parameters: the inside-to-outside pressure ratio and density ratio. The equations of state for the inside gas and the outside ambient will also play a role. But for simplicity we have taken them to follow the ideal gas law relations with adiabatic index of 1.4. In all of the results presented in the previous sections the pressure ratio and density ratios were kept at 22 and correspondingly the temperature of the high-pressure core was equal to the ambient temperature. Thus, this case corresponds to the "cold explosion" limit. This operating condition is the same as that employed by Brode (1959) and Freidman (1961) in their investigations, and is denoted by a star in Figure 2–12. Three sets of parametric studies were performed in order to ascertain the effect of pressure and density ratios on the nature of the base flow contact interface and the resulting non-classical RT instability. In the first set, the pressure ratio is varied and the temperature inside the initial sphere is set equal to the ambient temperature and thus the density ratio is equal to the pressure ratio. The second set corresponds to a fixed pressure ratio of 100 and the density ratio is varied from 100 to 1. The final set corresponds to a fixed density ratio of 6 with varying pressure ratio.

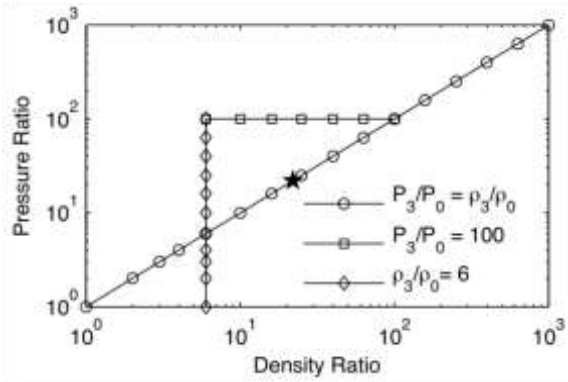

Figure 2–12. Parametric Study of the Pressure Ratio and Density Ratio.

The parametric study revealed two interesting limiting cases. The first is when the pressure ratio is close to unity but the density ratio is larger. In this case, the flow resembles a stationary droplet rather than a spherical shock tube. Another limiting case is when the contact interface resulting from the spherical shock tube has an Atwood number of zero, i.e. no density discontinuity. However the first derivative of the density is still discontinuous. In the present set of simulations this second limiting case is reached either by increasing the pressure ratio past 16 while keeping the density ratio fixed at 6, or by decreasing the density ratio past 16 for a fixed pressure ratio of 100. The three sets of parametric studies and their respective limiting cases are described below in further detail.

2.5.1. Set 1: Pressure Ratio is Equal to the Density Ratio

As predicted by RT instability theory, and verified by the simulation results presented in section 5, the two key quantitative measures of the contact interface that control the perturbation growth rate are the Atwood number and the deceleration of the interface (which is also nearly equal to the pressure gradient scaled by density, i.e., g_p). Here we will focus on the variation of these two flow parameters obtained from the numerical solution of the base flow. The resolution of the base flow was chosen such that the Atwood number and the velocity of the contact interface approached grid independence. However, as discussed in Figure 2–4b the thickness of the contact interface remains finite.

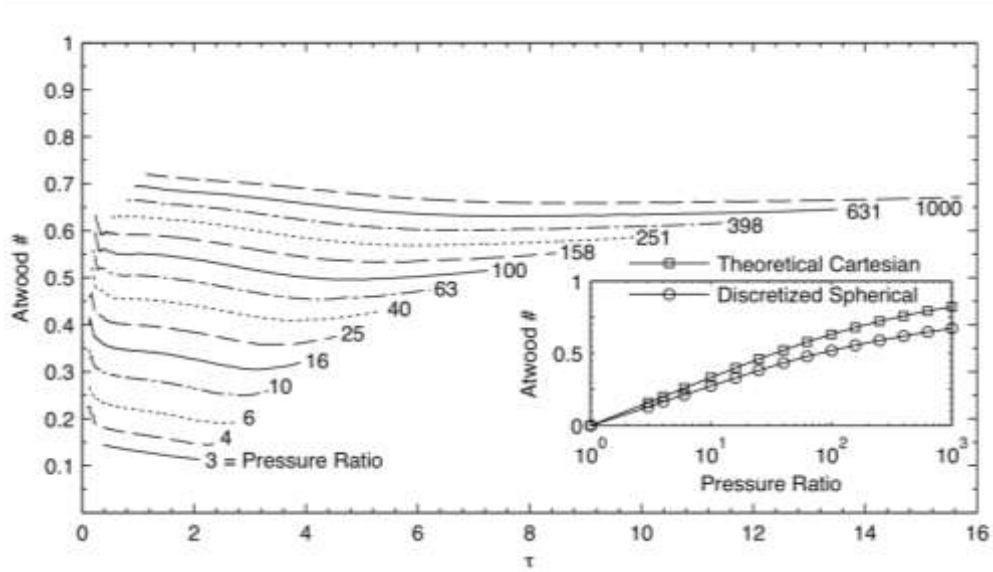

Figure 2–13. The Atwood number as a function of time for various pressure ratios and density ratios.

Figure 2–13 shows the time evolution of the Atwood number for varying initial pressure ratio (the initial density ratio is the same as pressure ratio). For the lowest and the highest pressure ratios of 3 and 1000 shown in the figure, the corresponding Atwood number calculated based on the initial density jump across the spherical diaphragm are 0.15 and 0.72. Once the diaphragm is released the total density jump between the inside gas (still undisturbed by the expansion fan) and the ambient remains the same. However, the density jump is divided amongst the primary shock, secondary shock, and contact interface. Immediately following the release, in order to predict the functional dependence of the Atwood number on the initial pressure and temperature ratios, we will examine the planar shock tube relations and compare them to the spherical case. The resulting Atwood number as a function of initial pressure and density ratios can be obtained by writing the Atwood number in terms of the temperatures since the pressure is continuous across the CI:

$$At_{planar}\Big|_{t\to 0+} = \frac{T_1 - T_2}{T_1 + T_2}, \tag{62}$$

where T_1 and T_2 are temperatures outside and inside the contact interface. In order to compute T_1 and T_2, the shock Mach number M_s must first be computed from the initial pressure ratio $\frac{P_3}{P_0}$ and temperature ratio $\frac{T_3}{T_0}$ (the initial density ratio is used to obtain the temperature ratio):

$$\frac{P_3}{P_0} = \frac{2\gamma M_s^2 - (\gamma - 1)}{(\gamma + 1)\left\{1 - \frac{\gamma - 1}{\gamma + 1}\sqrt{\frac{T_0}{T_3}}\left(M_s - \frac{1}{M_s}\right)\right\}^{\frac{2\gamma}{\gamma - 1}}} \tag{63}$$

Here P_3 corresponds to the initial condition inside the high pressure sphere and P_0 corresponds to ambient conditions. Now T_1 can be obtained from the moving normal shock relation:

$$\frac{T_1}{T_0} = 1 + 2\frac{\gamma - 1}{(\gamma + 1)^2}\,(1 + \gamma\, M_s^2)\left(1 - \frac{1}{M_s^2}\right) \tag{64}$$

Finally T_2 is obtained from the constant Riemann characteristics across the expansion fan:

$$\frac{T_1}{T_0} = 1 + 2\frac{\gamma - 1}{(\gamma + 1)^2}\,(1 + \gamma\, M_s^2)\left(1 - \frac{1}{M_s^2}\right) \tag{65}$$

Once the temperatures across the CI are computed, the Atwood number in (62) is computed and plotted as a function of the pressure ratio in Figure 2–13 as an inset. In the computations of the spherical shock tube, immediately following the initial release, the Atwood number across the contact interface rapidly increases to reach a peak (as the interface forms) and then rapidly decreases to reach a near constant value (this can be more clearly observed in Figure 2–4a). Over longer time the Atwood number of the contact interface shows a slow variation. The time averaged value of the computed Atwood number, averaged after the rapid initial transients, is also shown in the inset of Figure 2–13. Notice that the planar Atwood number predicted using the planer shock tube theory (62) is somewhat larger than the computed time-averaged value of the spherical Atwood number. We observe this difference to somewhat reduce with increasing resolution of the CI.

The velocity of the contact interface computed for set 1 is shown in Figure 2–14, plotted as a function of time. Although deceleration of the interface appears to slowly vary over time, it can be seen that in all the cases over an extended period of time the variation in interface deceleration is quite small. It is also evident that the magnitude of the deceleration weakens with increasing pressure ratio. In Figure 2–13 and Figure 2–14 the time varying results for the Atwood number and CI velocity are plotted only over the time duration till about the point when the secondary shock reflects off the origin. This allows us to focus on non-classical RT instability, since the subsequent interaction between the contact interface with the secondary shock will involve RM instability. The duration of non-classical RT instability increases with pressure ratio from about 2 time units for an initial pressure ratio of 3 to about 16 time units for a pressure ratio of 1000. As discussed in Brode (1955) the time scale of spherical expansion depends on initial pressure ratio as $\left(\frac{P_3}{P_0}\right)^{1/3}$, which is in excellent agreement with the increase in the time duration of non-classical RT instability shown in Figure 2–13 and Figure 2–14.

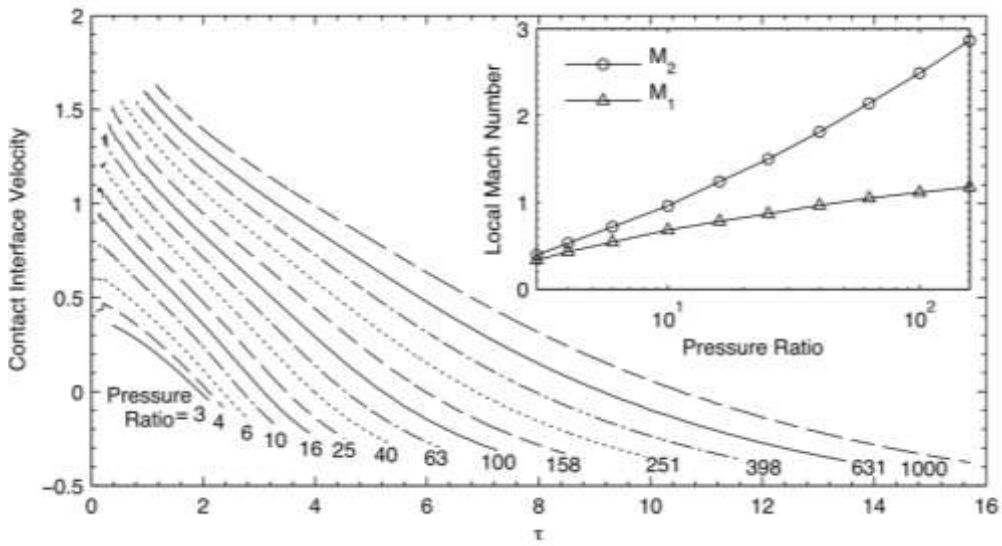

Figure 2–14. The CI Velocity as a function of time for various pressure ratios and density ratios.

The flow is initially at rest but upon releasing the diaphragm the velocity rapidly reaches its maximum (which appears as the initial CI velocity in Figure 2–14). The Mach number for this peak velocity is plotted for various pressure ratios in the inset of Figure 2–14. Since density is discontinuous, two different Mach numbers associated with the contact interface are plotted. The two Mach numbers are based on local values inside and outside of the contact interface, M2 and M1 respectively. Since the CI velocity in Figure 2–14 was normalized by the ambient speed of sound it falls between M2 and M1. Both the inner and outer Mach numbers monotonically increase as the pressure ratio increases, which suggest increasing compressibility effects.

The inset of Figure 2–15 shows the time-averaged square root of the product of the Atwood number and deceleration of the contact interface against the pressure ratio. It is evident that the product reaches an asymptotic constant value. Increasing the pressure ratio beyond 100 (which corresponds to a CI Mach number of about 2) can be expected to have a negligible effect on the perturbation growth rate. In Figure 2–15 the time evolution of the integrated perturbation radial velocity squared is plotted as a function of time for various initial pressure ratios at a fixed spherical wave number of 45. For this wave number adequate resolution has been achieved for both the base flow and the perturbation for all the pressure ratios. The growth rate of the perturbation is observed to increase with increasing pressure ratio, but consistent with the inset of Figure 2–15, the long term growth rate of the disturbance remains the same for initial pressure ratios in excess of 100.

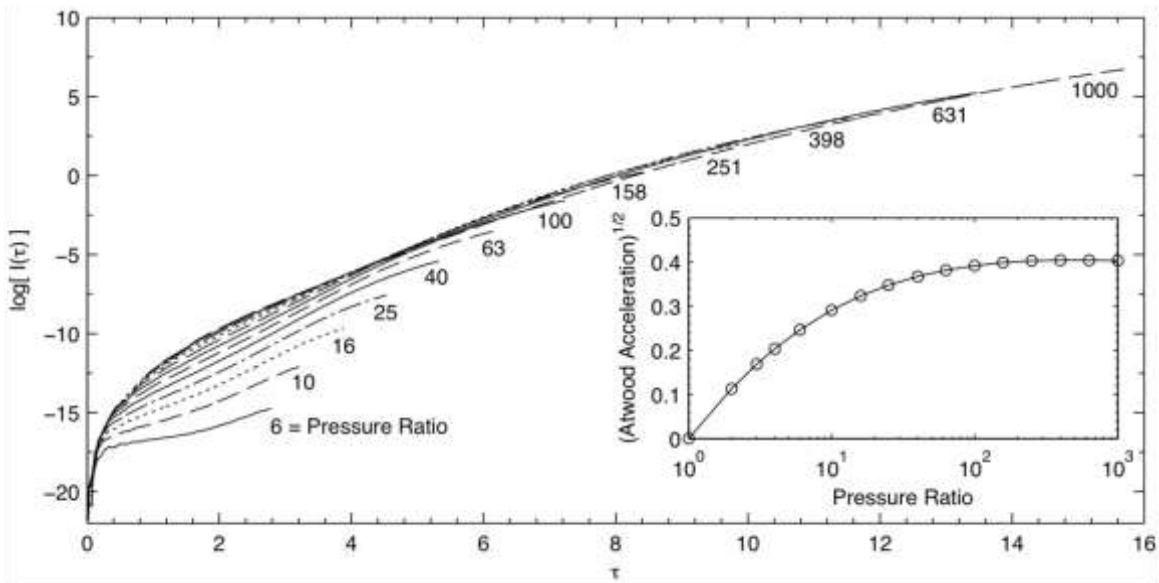

Figure 2–15. The growth of the perturbations for a wave number of 45 for various pressure ratios.

For varying pressure ratios, the effect of compressibility and spherical geometry on the growth rate of the instability is investigated as follows. We calculate the theoretical growth rate using Epstein's formulation (58) with σ_o, σ_ϱ, and σ_R evaluated from the computed base flow. Figure 2–16 shows the growth rate σ_o for varying pressure ratio, which corresponds to classical RT instability without compressibility and geometric effects. Also plotted is σ_{Ep} which includes both compressibility and Bell-Plesset effects. Setting $\sigma_\varrho = 0$ allows us to include the Bell-Plesset effects but exclude the compressibility effects and results thus obtained are also shown. It is evident that the effect of compressibility is to decrease the growth rate. This Mach number effect is consistent with the conclusions of Yu and Livescu (2008). Ignoring both compressibility and spherical geometry effects results in a decrease in the predicted growth rate. Thus the geometry effect more than compensates for the compressibility effect. This finding is consistent with the observation seen in Figure 2–10 that Plesset overestimates the growth rate, while prediction based on Taylor's and Epstein's theories are in better agreement.

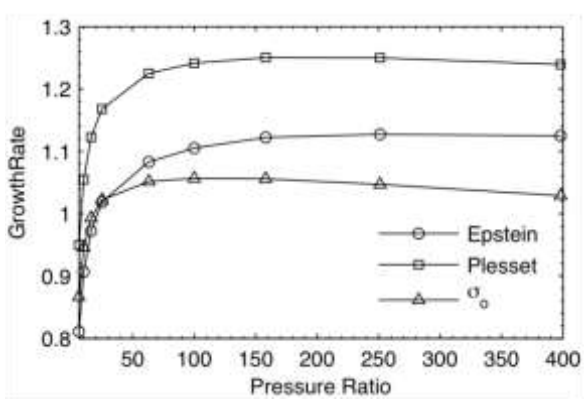

Figure 2–16. The growth rate predicted by various theoretical works for a wave number of 45 for various pressure ratios.

2.5.2. Set 2: Pressure Ratio is Fixed at 100 but the Density Ratio is Varying

In set two the initial pressure and density ratios are no longer equal. In other words, the initial core temperature is no longer equal to the ambient temperature but hotter. For a fixed pressure ratio as the density ratio drops the core temperature becomes hotter. Figure 2–17a shows the time evolution of Atwood number for the different density ratios for a fixed pressure ratio of 100. For the largest density ratio of 100 considered, the Atwood number is about 0.58 and with decreasing density ratio the Atwood number decreases. For a density ratio of 25 (the core is four times hotter than the ambient), the contact interface is characterized by a very week density jump. Further reduction in density ratio, to a value of 16, results in a near zero Atwood number. For the density ratio of 16, a plot similar Figure 2–11c of the radial variation in base flow density (not shown here) indicates that for $\tau > 0.1$ there is no density discontinuity across the contact interface, although the contact interface is marked by a rapid change in the radial derivative of the density. In this case, the initial density ratio of 16 gets distributed across the primary and secondary shocks, with virtually no change in density across the contact interface. The planar case formula (63) predicts that the Atwood number goes negative; however, this is not the case for the spherical geometry. Figure 2–17b presents the corresponding CI velocity for various density ratios and deceleration of the contact interface increases with decreasing density ratio. The inset of the figure illustrates that at the zero Atwood number limit M2 and M1 are identical.

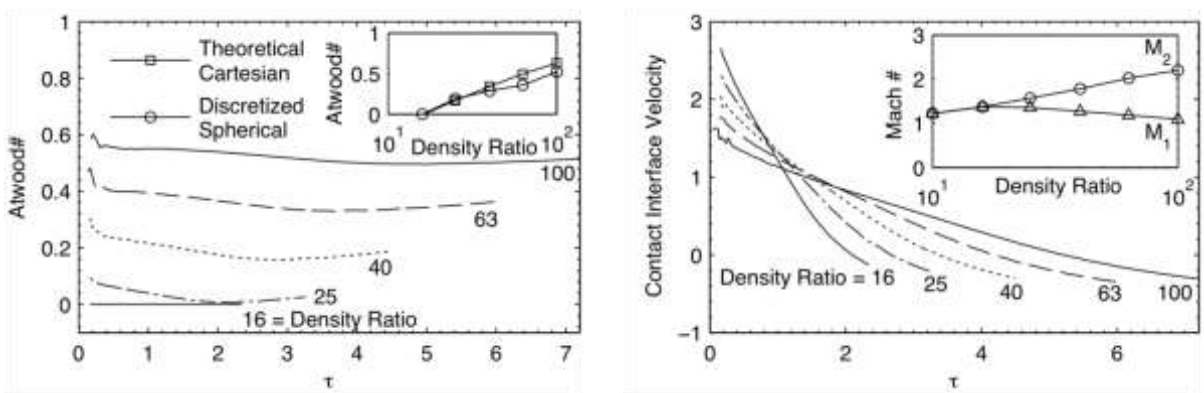

17a **17b**

Figure 2–17. The Atwood number (17a) and CI Velocity (17b) as a function of time for a pressure ratio of 100 and various density ratios.

Figure 2–18 depicts the time evolution of the perturbation for the various density ratios. As can be expected from the above base flow characterization, the perturbation is barely growing for density ratios less than 25. Notice that as the density ratio decreases from 100 to 16 the interface's deceleration increases but Atwood number decreases. Figure 2–18 reflects the fact that the decrease in Atwood number is greater than the increase in the interface's deceleration.

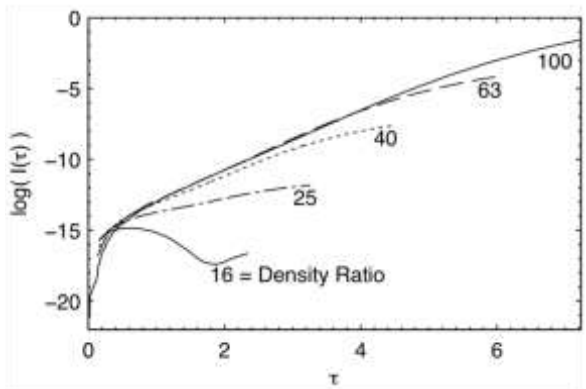

Figure 2–18. For a pressure ratio of 100, the growth of the perturbation for various density ratios at a wave number of 45.

2.5.3. Set 3: The Density Ratio is Fixed at 6 but the Pressure Ratio is Varying

As the pressure ratio increases for a fixed density ratio of 6, Figure 2–19a and Figure 2–19b show that the Atwood number decreases but deceleration increases. The zero Atwood number limit can be reached by increasing the pressure ratio to 16 for a fixed density ratio of 6 as depicted in Figure 2–19a. In that case, the core temperature is approximately 2.5 hotter than the ambient temperature. Another interesting limiting case that appears in this set is when the pressure ratio approaches unity for a fixed density ratio of 6. Such a limit is analogous to a stationary droplet in a zero-g environment.

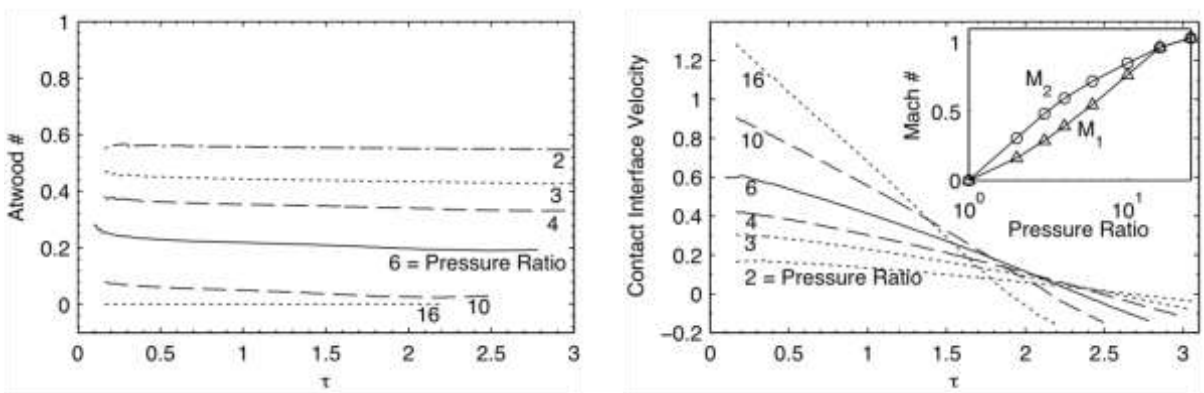

19a 19b

Figure 2–19. The Atwood number (19a) and CI Velocity (19b) for a density ratio of 6 and various pressure ratios.

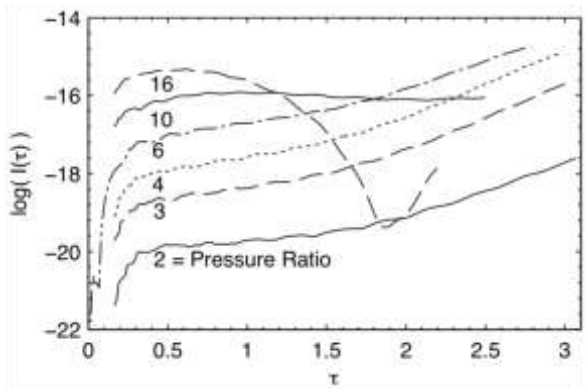

Figure 2–20. For a density ratio of 6, the growth of the perturbation for various density ratios at a wave number of 45.

Recall for the zero Atwood limit the initial density jump across the diaphragm is distributed to the primary and secondary shocks and none to the contact interface. The stationary droplet limit is the opposite, the initial density jump is all allocated to the contact interface and consequently there is no primary or secondary shock. As in the previous two sets the development of the instability is shown in Figure 2–20. Increasing the pressure ratio while fixing the density initially results in a slight increase of the growth rate, but as the pressure ratio increases to about 16 the zero Atwood number limit is reached and the perturbations decay.

2.6. Summary

We have presented herein the linear inviscid stability analysis of the spherical contact interface associated with the sudden release of a high-pressure gas initially contained in a small spherical region. The perturbations were expanded in spherical harmonics to reduce their dependence to only the radial coordinate and time. A high-order WENO scheme was employed to capture the time evolving radial structure of both the base flow and the perturbed flow. The numerical scheme is able to predict a sharper discontinuity with increasing grid resolution without introducing numerical noise around the discontinuity.

For the perturbation analysis, we focus attention to times well before the interaction of the reflected secondary shock with the contact interface. Thus, our results isolate the Rayleigh-Taylor instability from the Richtmyer-Meshkov instability. During this period of interest, the deceleration and characteristics of the contact interface are observed to be nearly constant. As a result, despite the time-dependent nature of the base flow an eigen structure for the disturbance with an exponential growth is observed. Outside this time domain, the growth rate of the perturbation begins to deviate from an exponential growth and slows down.

The radial profiles of the perturbation density and radial velocity were found to be Gaussian-like with a peak around the contact interface, while the tangential velocity switches sign around the contact interface. The effects of the initial disturbance structure was found to be limited to very early time, as the input disturbance quickly evolves to the eigen structure corresponding to the growing mode.

Over an intermediate range of spherical harmonic wave number the growth rate increases with $\sqrt{n}$. This classic RT instability behavior is observed provided the grid resolution is such that the

disturbance sees the contact interface as a near discontinuity. For larger wave numbers, the radial thickness of the perturbation decreases and the finite thickness of the interface influences the perturbation growth rate. In the limit of very large n, the disturbance length scale becomes smaller than the contact interface thickness and in this limit a constant growth rate is approached. Also for very small values of n the perturbation extends over a large radial extent and begins to interact with the primary and secondary shocks. In this limit also the growth rate departs from the $\sqrt{n}$ behavior.

The simulation results compared favorably with the theoretical predictions. The best agreement was with the theoretical model of RT instability by Epstein (2004), since it included both the effects of compressibility and the spherical geometry. Comparison with model of Plesset which ignored the effect of compressibility reveals that the effect of compressibility in the present problem is to reduce the instability's growth rate.

A systematic parametric study was conducted where the inside-to-outside pressure and density ratios were varied. In Set I of the parametric study, the initial temperature ratio was fixed and the pressure ratio was varied, which demonstrated that the growth rate increases with increasing the pressure ratio, until a saturation level that is reached for a pressure ratio of about 100. Further increase in the pressure ratio has little or no effect on the disturbance growth rate. In terms of Mach number of the CI, increasing the Mach number of the CI beyond 2 has little effect on the growth rate. This phenomenon is explained by the fact that the product of the acceleration and the Atwood number of the contact interface reaches an asymptotic value at such high pressure ratios.

In Sets II and III of the parametric study, the initial temperature ratio was allowed to vary by fixing the pressure ratio and varying the density ratio, or by fixing the density ratio and varying the pressure ratio. In both sets it was demonstrated that it is possible to reach a combination of these parameters such that the Atwood number of the CI is practically zero, which may have some significant implication on the possibility of controlling the perturbation instability. Thus, heating of the core for a given pressure ratio can eliminate Rayleigh-Taylor instability.

3. VISCOUS EFFECTS ON THE RAYLEIGH-TAYLOR INSTABILITY OF RAPIDLY EXPANDING SPHERICAL MATERIAL INTERFACES

3.1. Introduction

The interest in studying the stability of a viscous spherical material interface stems from its relevance to many engineering applications such as supersonic combustion, pulse denotation engines, fusion reactors, and propellant rocket motors. Understanding the mechanisms by which the contact interface becomes unstable has several benefits in these applications. For instance, in combustion-based applications, a spherical interface separates the hot fuel mixture from the cold ambient air. Mixing at the interface is essential for continued secondary burning and the release of additional energy. Consequently, the stability of the interface strongly affects the combustion's efficiency.

The early work of Rayleigh (1900) and Taylor (1950a) considered the stability of a plane inviscid interface separating two incompressible stationary fluids of different densities subjected to gravity acceleration. When the direction of gravity is from the heavier to the lighter fluid, Taylor has shown that the flow is unstable and that the instability's growth rate is proportional to the square root of the product of wavenumber, acceleration, and Atwood number. The latter is defined as the ratio of the difference between the two densities to their sum.

The effect of viscosity on the stability of a spherical material interface has been addressed by several researches for incompressible flow situations. Prosperetti (1977) considered the viscous effects of an external liquid on the stability of the contact interface separating an air bubble from the outer liquid. The effect of the viscous boundary-layer thickness is presented in Hao and Prosperetti (1999). In both of these works the density of the inner bubble is neglected. However, recently Lin et al.(2002) extended these works to account for the density of the gas bubble. These studies indicate that the effect of viscosity is to dampen the growth rate of the incompressible Rayleigh-Taylor Instability (RTI) as in the planar case (Chandrasekhar, 1981; Duff et al., 1962).

In many real world applications involving rapid expansion of a material interface the flow is compressible. Therefore in our study, the focus is on the effects of viscosity on the instability of a spherical interface while accounting for the full compressibility effects of both the base flow and the perturbed flow. A Roe-Pike (1999) solver coupled with a high-order WENO scheme is employed to simulate the base flow resulting from the rapid rupture of a spherical diaphragm enclosing high pressure gas. Due to the density jump across the contact interface produced by the rupture, Rayleigh-Taylor instability develops. The governing equations for the 3D linear viscous compressible perturbations are derived, and then solved using an extension of the Roe-Pike scheme and the WENO scheme. The purpose of the linearization is to allow for the expansion of the three-dimensional disturbance in terms of spherical harmonics. Following the spherical decomposition, the viscous governing equations reduce to a set of simultaneous 1D PDEs in time and radial coordinate. While linearization results in the loss of the important nonlinear effects, it allows eliminating the two angular coordinates and hence enabling us to explore high-wave numbers perturbations.

Accounting for the viscous effects results in two major changes that are not present in the inviscid limit. The first is the inclusion of viscous diffusion, which is proportional to the square of the spherical wave number. Hence, as the wave number increases viscous diffusion becomes

more dominant resulting in an optimal wave number of maximum disturbance growth rate. The second major change results from accounting for the base flow's viscous effects. The Atwood number of the base flow is reduced as a result of the viscous effect, which again reduces the disturbance growth rate.

The study is presented in the following order: in section II the derivation of the viscous perturbation equations in spherical coordinates is described. The boundary conditions and numerical implementation are explained in section III. The results for the stability of the contact interface are presented in section IV, while conclusions are given in section V.

3.2. Formulation

Before analyzing the stability of the contact interface, the base flow must first be defined. The base flow of interest here is produced by the sudden release of a high pressure gas contained in a sphere into the air. The limiting case for the base flow is Taylor's (1950b) and Sedov's (1946) point source solution, where the initial high pressure radius goes to zero, i.e., all the energy is contained in a single point at the origin. It is well understood that in the context of a finite-source release (as opposed to point-source), in addition to the main shock wave, there will be a contact interface discontinuity and an expansion fan. The tail of the expansion fan, due to the radial effect, becomes a second shock wave, which after a brief period of outward propagation, turns and starts to move inwards towards the origin. These additional discontinuous surfaces were discussed by Brode (1955) and Friedman (1961). At the contact interface, the pressure and radial velocity on the two sides are the same, but the density and temperature are discontinuous across the interface. Initially, the contact discontinuity moves radially outward behind the main shock front, but its velocity continually decreases until it starts to move inwards towards the origin. After a long time, the contact discontinuity reaches an asymptotic radial location defining the near-field of rapid energy release, while the main shock wave continues to travel out. The far-field solution of the blast wave becomes identical to Taylor's self-similar solution so long as the shock remains strong. Our focus herein is on the viscous Rayleigh-Taylor Instability of the contact interface that develops between the primary and secondary shocks.

3.2.1. Base Flow Equations (Zero-Order)

Here we pursue the approach of Ling et al. (2009) for the base flow, where due to spherical symmetry, only the radial velocity is of importance and the flow quantities are dependent only on time and the radial coordinate. For simplicity, the fluid is taken to be a perfect gas. The base flow equations reduce to a system of three nonlinear partial differential equations in r and t. The continuity, momentum, and energy equations are given by:

$$\frac{\partial \varrho}{\partial t} + \frac{\partial(\varrho U)}{\partial r} + \frac{2\varrho U}{r} = 0 \tag{66}$$

$$\frac{\partial(\varrho U)}{\partial t} + \frac{\partial(\varrho U^2 + P)}{\partial r} + \frac{2\varrho U^2}{r} = \Gamma \tag{67}$$

$$\frac{\partial E}{\partial t}+\frac{\partial(UH)}{\partial r}+\frac{2UH}{r}=\mu\Phi+\frac{\partial}{\partial r}\left(\frac{k}{r^2}\frac{\partial(r^2T\,)}{\partial r}\right)+\frac{2}{r^2}kT \tag{68}$$

Here E is the total energy and U is the base flow velocity in the radial direction. The density is ρ; the pressure is P, the temperature is T, and the total enthalpy H is given by:

$$H=E+P \tag{69}$$

The viscosity μ varies with temperature and is given by the Sutherland Law,

$$\mu=\mu_o T_1(T) \qquad\qquad T_1=\left(\frac{T}{T_o}\right)^{\frac{3}{2}}\frac{T+S}{T_o+S} \tag{70}$$

Here (μ_o, T_o, S) are the reference viscosity, reference temperature, and the Sutherland temperature. The reference viscosity is typically taken to be the same as the ambient viscosity. The radial viscous term is defined as:

$$\frac{\Gamma}{\mu_o}=\frac{4}{3}\frac{\partial}{\partial r}\left[T_1\left(\frac{\partial U}{\partial r}-\frac{U}{r}\right)\right]+4\frac{T_1}{r}\left(\frac{\partial U}{\partial r}-\frac{U}{r}\right) \tag{71}$$

The dissipation function for a radial flow is:

$$\Phi=\ 2\left[\left(\frac{\partial U}{\partial r}\right)^2+2\left(\frac{U}{r}\right)^2\right]-\frac{2}{3}\left[\frac{\partial U}{\partial r}+2\frac{U}{r}\right]^2 \tag{72}$$

We also assume that the thermal conductivity, like the viscosity, follows the Sutherland's law, i.e., the Prandtl number is a constant. Thus, k also varies with temperature as:

$$k(T)=k_o T_1 \tag{73}$$

Here k_o is a reference thermal conductivity. The base flow domain extends from the origin to beyond the primary shockwave where ambient conditions prevail.

3.2.2. The Linearized Perturbation Equations

The starting point for deriving the perturbation equations is the fully compressible Navier Stokes equations in spherical coordinates. We begin by assuming that each flow quantity is composed of the base flow (U, V, W, P, ϱ) and a perturbation (u', v', w', p', ρ'). Thus,

$$u=U+u';\ v=V+v';\ w=W+w';\ p=P+p';\ \rho=\varrho+\rho'; \tag{74}$$

Here (u', v', w', p', ρ') are the perturbation radial velocity, azimuthal velocity, zenithal (polar) velocity, pressure, and density, respectively. Upon substituting this split into the governing equations, neglecting the nonlinear terms, and subtracting the base flow equations, the linearized continuity is obtained as follows:

$$\frac{\partial \rho'}{\partial t} + \frac{1}{r^2}\frac{\partial (r^2 U \rho')}{\partial r} + u'\frac{\partial \varrho}{\partial r} + \varrho(\boldsymbol{\nabla} \cdot \boldsymbol{v}') = 0 \tag{75}$$

For the spherical coordinate system, we define:

$$D' = \boldsymbol{\nabla} \cdot \boldsymbol{v}' = \frac{1}{r^2}\frac{\partial (r^2 u')}{\partial r} + \frac{1}{r sin\theta}\frac{\partial\,(v' \sin\theta)}{\partial \theta} + \frac{1}{r sin\theta}\frac{\partial w'}{\partial \phi} \tag{76}$$

The r-momentum equation is given by:

$$\varrho\frac{\partial u'}{\partial t} + \rho'\frac{\partial U}{\partial t} + \varrho U\frac{\partial u'}{\partial r} + (\rho' U + \varrho u')\frac{\partial U}{\partial r} = -\frac{\partial p'}{\partial r} + \left[\frac{1}{r^2}\frac{\partial}{\partial r}(r^2 \tau'_{rr}) + \frac{1}{r sin\theta}\frac{\partial}{\partial \theta}(\tau'_{r\theta}\, sin\theta) + \frac{1}{r sin\theta}\frac{\partial \tau'_{\phi r}}{\partial \phi} - \frac{\tau'_{\theta\theta} + \tau'_{\varphi\varphi}}{r}\right] \tag{77}$$

The first-order shear stresses are represented by τ'. The tangential momentum equation is deduced from the θ and ϕ momentum equations which are given by:

$$\varrho\frac{\partial v'}{\partial t} + \varrho U\frac{\partial v'}{\partial r} + \frac{v' U \varrho}{r} = -\frac{1}{r}\frac{\partial p'}{\partial \theta} + \left[\frac{1}{r^3}\frac{\partial}{\partial r}(r^3 \tau'_{r\theta}) + \frac{1}{r\, sin\theta}\frac{\partial}{\partial \theta}(\tau'_{\theta\theta}\, sin\theta) + \frac{1}{r\, sin\theta}\frac{\partial \tau'_{\theta\phi}}{\partial \phi} - \frac{\tau'_{\phi\phi}\cot\theta}{r}\right] \tag{78}$$

$$\varrho\frac{\partial w'}{\partial t} + \varrho U\frac{\partial w'}{\partial r} + \frac{w' U \varrho}{r} = -\frac{1}{r\, sin\theta}\frac{\partial p'}{\partial \phi} + \left[\frac{1}{r^3}\frac{\partial}{\partial r}\left(r^3 \tau'_{r\phi}\right) + \frac{1}{r\, sin\theta}\frac{\partial}{\partial \theta}\left(\tau'_{\theta\phi}\, sin\theta\right) + \frac{1}{r\, sin\theta}\frac{\partial \tau'_{\phi\phi}}{\partial \phi} + \frac{\tau'_{\theta\phi}\cot\theta}{r}\right] \tag{79}$$

The energy equation is given by:

$$\frac{\partial E'}{\partial t} + \frac{1}{r^2}\frac{\partial(r^2 UH')}{\partial r} + u'\frac{\partial H}{\partial r} + HD' = \mu'\Phi + \frac{\partial}{\partial r}\left(\frac{k'}{r^2}\frac{\partial(r^2 T)}{\partial r}\right) + \frac{2}{r^2}k''T$$

$$4\mu\left\{\frac{\partial U}{\partial r}\frac{\partial u'}{\partial r} + \frac{U}{r^2}\left(2u' + \frac{\partial v'}{\partial \theta} + v'cot\theta + \frac{1}{sin\theta}\frac{\partial w''}{\partial \phi}\right)\right\} - \frac{4\mu}{3}\frac{1}{r^2}\frac{\partial(r^2 U)}{\partial r}D' + \tag{80}$$

$$k\left\{\frac{1}{r^2}\frac{\partial}{\partial r}\left(r^2\frac{\partial T''}{\partial r}\right) + \frac{1}{r^2 sin\theta}\frac{\partial}{\partial \theta}\left(\sin\theta\frac{\partial T''}{\partial \theta}\right) + \frac{1}{r^2\sin^2\theta}\frac{\partial^2 T''}{\partial \phi^2}\right\}$$

The system is closed by,

$$H' = E' + P' \tag{81}$$

The total energy and total enthalpy of the perturbations are E' and H' respectively. As previously mentioned when presenting the base flow, the viscosity is not constant in space but rather varies with temperature according to the Sutherland law. Consequently, perturbation viscosity μ' appears and is defined as:

$$\mu' = \mu_0 T_2(T, T') \qquad T_2 = T_1\left(\frac{3}{2}\frac{T'}{T} + \frac{T'}{T+S}\right) \tag{82}$$

Likewise, the perturbation thermal conductivity also varies with both the perturbation and base temperature:

$$k' = k_o T_2 \tag{83}$$

3.2.3. Spherical Harmonic Decomposition

The total perturbation velocity is composed of two components: u' in the radial direction and $\boldsymbol{q}'$ for the tangential direction, where

$$\boldsymbol{q}' = v'\,\widehat{\boldsymbol{\theta}} + w'\widehat{\boldsymbol{\phi}} \tag{84}$$

Here $\widehat{\boldsymbol{\theta}}$ and $\widehat{\boldsymbol{\phi}}$ are unit vectors along the azimuthal and zenithal (polar) directions respectively, and

$$\boldsymbol{\nabla_T} = \frac{1}{r}\left(\widehat{\boldsymbol{\theta}}\,\frac{\partial}{\partial \theta} + \widehat{\boldsymbol{\phi}}\frac{1}{sin\theta}\,\frac{\partial}{\partial \phi}\right) \tag{85}$$

is the gradient in the tangential direction. Since the perturbations are linear, we can expand them along the $\widehat{\boldsymbol{\theta}}$ and $\widehat{\boldsymbol{\phi}}$ directions using the spherical harmonic functions as:

$$\boldsymbol{q}'(r,\theta,\phi,t) = \tilde{q}\,(r,t)\,r\,\boldsymbol{\nabla_T} Y_{nm}(\theta,\phi) \tag{86}$$

$$\begin{Bmatrix} \rho'(r,\theta,\phi,t) \\ u'(r,\theta,\phi,t) \\ p'(r,\theta,\phi,t) \\ E'(r,\theta,\phi,t) \\ H'(r,\theta,\phi,t) \end{Bmatrix} = \begin{Bmatrix} \tilde{\rho}(r,t) \\ \tilde{u}(r,t) \\ \tilde{p}(r,t) \\ \tilde{E}(r,t) \\ \tilde{H}(r,t) \end{Bmatrix} Y_{nm}(\theta,\phi) \tag{87}$$

Here, n = 0, 1, 2,… and m = 0, 1, 2,…, n. The spherical harmonic $Y_{nm}(\theta,\phi)$ of order n, m is given by:

$$Y_{nm}(\theta,\phi) = L_n^m(\theta)\, e^{im\phi} \tag{88}$$

Here $L_n^m(\theta)$ is the associated Legendre polynomial. Upon employing this decomposition the divergence becomes:

$$D' = \left[\frac{1}{r^2}\frac{\partial(r^2 u')}{\partial r} + \boldsymbol{\nabla_T}\cdot\boldsymbol{q}'\right] = Y_{nm}\widetilde{D} \qquad \widetilde{D} = \frac{\partial\tilde{u}}{\partial r} + \frac{2\tilde{u} - \lambda\tilde{q}}{r} \tag{89}$$

where $\lambda = n(n+1)$. After substituting the decomposition into the linearized equations we obtain:

$$\frac{\partial\tilde{\rho}}{\partial t} + \frac{1}{r^2}\frac{\partial[r^2(U\tilde{\rho} + \varrho\tilde{u})\,]}{\partial r} - \varrho\lambda\frac{\tilde{q}}{r} = 0 \tag{90}$$

$$\varrho\left(\frac{\partial\tilde{u}}{\partial t} + \tilde{u}\frac{\partial U}{\partial r} + U\frac{\partial\tilde{u}}{\partial r}\right) + \frac{\partial\tilde{p}}{\partial r} - \frac{\tilde{\rho}}{\varrho}\frac{\partial P}{\partial r} = \left\{\frac{\partial}{\partial r}\left[\mu\left(2\frac{\partial\tilde{u}}{\partial r} - \frac{2}{3}\widetilde{D}\right)\right] + \frac{\mu}{r}\tilde{S}_{\mu u}\right\} - \frac{\tilde{\rho}}{\varrho}\Gamma + \tilde{\Gamma} \tag{91}$$

$$\varrho\,\frac{\partial\tilde{q}}{\partial t} + \varrho U\left(\frac{\partial\tilde{q}}{\partial r} + \frac{\tilde{q}}{r}\right) + \frac{\tilde{p}}{r} = \frac{\partial}{\partial r}(\mu\tilde{G}) + \frac{\mu}{r}\tilde{S}_{\mu q} \tag{92}$$

$$\begin{aligned} \frac{\partial\tilde{E}}{\partial t} + \frac{1}{r^2}\frac{\partial\left(r^2 U\tilde{H}\right)}{\partial r} + \tilde{u}\frac{\partial H}{\partial r} + H\left[\frac{1}{r^2}\frac{\partial(r^2\tilde{u})}{\partial r} - \frac{\lambda\tilde{q}}{r}\right] = \mu\widetilde{\Phi} + \tilde{\mu}\Phi + \\ \frac{\partial}{\partial r}\left(\frac{k}{r^2}\frac{\partial(r^2\tilde{T}\,)}{\partial r}\right) + \frac{2-\lambda}{r^2}k\tilde{T} + \frac{\partial}{\partial r}\left(\frac{\tilde{k}}{r^2}\frac{\partial(r^2 T\,)}{\partial r}\right) + \frac{2}{r^2}\tilde{k}T \end{aligned} \tag{93}$$

where,

$$\widetilde{\Phi} = 4\left[\frac{\partial U}{\partial r}\frac{\partial \tilde{u}}{\partial r} + \frac{U}{r^2}(2\tilde{u} - \lambda\tilde{q}) - \frac{1}{r^2}\frac{\partial(r^2 U)}{\partial r}\frac{\widetilde{D}}{3}\right] \tag{94}$$

$$\frac{\tilde{\Gamma}}{\mu_o} = \frac{4}{3}\frac{\partial}{\partial r}\left[T_2\left(\frac{\partial U}{\partial r} - \frac{U}{r}\right)\right] + 4\frac{T_2}{r}\left(\frac{\partial U}{\partial r} - \frac{U}{r}\right) \tag{95}$$

$$\tilde{S}_{\mu u} = 2\left[2\frac{\partial \tilde{u}}{\partial r} - \frac{2\tilde{u} - \lambda\tilde{q}}{r}\right] - \lambda\tilde{G} \tag{96}$$

$$\tilde{S}_{\mu q} = 3\tilde{G} + \frac{2\tilde{u}}{r} - \frac{2}{3}\widetilde{D} - 2(\lambda - 1)\frac{\tilde{q}}{r} \tag{97}$$

$$\tilde{G} = \frac{\partial \tilde{q}}{\partial r} - \frac{\tilde{q}}{r} + \frac{\tilde{u}}{r} \tag{98}$$

3.2.4. Dimensionless Conservative Form

3.2.4.1. Non-dimensionalization

In order to ascertain the effect of the Reynolds number and Prandtl number on the perturbed flow, the governing equations are normalized by reference values.

$$\xi = \frac{r}{r_o} \qquad \tau = \frac{c_a}{r_o}t \qquad \begin{pmatrix}\varrho^+\\ \tilde{\rho}^+\end{pmatrix} = \frac{1}{\varrho_a}\begin{pmatrix}\varrho\\ \tilde{\rho}\end{pmatrix} \qquad \begin{pmatrix}T^+\\ \tilde{T}^+\end{pmatrix} = \frac{1}{T_a}\begin{pmatrix}T\\ \tilde{T}\end{pmatrix} \tag{99}$$

$$\begin{pmatrix}U^+\\ \tilde{u}^+\\ \tilde{q}^+\end{pmatrix} = \frac{1}{c_a}\begin{pmatrix}U\\ \tilde{u}\\ \tilde{q}\end{pmatrix} \qquad \begin{pmatrix}H^+\\ \widetilde{H}^+\\ \tilde{E}^+\\ \tilde{p}^+\end{pmatrix} = \frac{1}{\varrho_a c_a^2}\begin{pmatrix}H\\ \widetilde{H}\\ \tilde{E}\\ \tilde{p}\end{pmatrix} \tag{100}$$

Here $(\mathrm{r_o}, c_a, \rho_a, T_a)$ are the initial location of the diaphragm, ambient speed of sound, ambient density, and ambient temperature, respectively. The Reynolds number and Prandtl number are defined as:

$$Re = \frac{\varrho_a c_a\, r_o}{\mu_o} \qquad Pr = \frac{\mu_o C_p}{k_o} \tag{101}$$

Recall μ_o is the reference viscosity that appears in the Sutherland law which is the same as the ambient viscosity.

3.2.4.2. Conservative Form

For aesthetic purposes from hence forth, the plus superscript in $\boldsymbol{U}^{+}$is dropped to $\boldsymbol{U}$ even though it is dimensionless; likewise for all the other remaining parameters. The final viscous dimensionless perturbation equations are written in conservative form with Reynolds and Prandtl numbers as follows:

$$\frac{\partial \boldsymbol{U}}{\partial \tau} + \frac{\partial \boldsymbol{F}}{\partial \xi} + \boldsymbol{S} = 0 \tag{102}$$

$$\boldsymbol{U} = \begin{Bmatrix} u_1 \\ u_2 \\ u_3 \\ u_4 \end{Bmatrix} = \begin{Bmatrix} \tilde{\rho} \\ \tilde{\rho}U + \varrho\tilde{u} \\ \varrho\tilde{q} \\ \tilde{E} \end{Bmatrix} \qquad \boldsymbol{F} = \begin{Bmatrix} u_2 \\ 2Uu_2 - \tilde{\rho}U^2 + \tilde{p} \\ Uu_3 \\ \tilde{u}H + U\tilde{H} \end{Bmatrix} + \boldsymbol{F_\mu} + \boldsymbol{F_k} \tag{103}$$

$$\boldsymbol{S} = \frac{1}{\xi}\begin{Bmatrix} 2u_2 - \lambda u_3 \\ U[2(2u_2 - \tilde{\rho}U) - \lambda u_3] \\ \tilde{p} + 3Uu_3 \\ 2\left(\tilde{u}H + U\tilde{H}\right) - \lambda\tilde{q}H \end{Bmatrix} + \boldsymbol{S}_\mu + \boldsymbol{S}_k \tag{104}$$

where,

$$\boldsymbol{F_\mu} = -\frac{T_1}{Re}\begin{Bmatrix} 0 \\ 2\dfrac{\partial\tilde{u}}{\partial\xi} - \dfrac{2}{3}\tilde{D} \\ \tilde{G} \\ 0 \end{Bmatrix} \qquad \boldsymbol{F}_k = \frac{-T_1}{RePr(\gamma-1)\xi^2}\begin{Bmatrix} 0 \\ 0 \\ 0 \\ \dfrac{\partial(\xi^2\tilde{T})}{\partial\xi} + \dfrac{T_2}{T_1}\dfrac{\partial(\xi^2 T)}{\partial\xi} \end{Bmatrix} \tag{105}$$

$$\boldsymbol{S}_\mu = -\frac{T_1}{Re}\begin{Bmatrix} 0 \\ \dfrac{\tilde{S}_{\mu u}}{\xi} - \dfrac{\tilde{\rho}}{\varrho}\dfrac{\Gamma}{T_1} + \dfrac{\tilde{\Gamma}}{T_1} \\ \dfrac{\tilde{S}_{\mu q}}{\xi} \\ \tilde{\Phi} + \dfrac{T_2}{T_1}\Phi \end{Bmatrix} \qquad \boldsymbol{S}_k = \frac{-T_1}{RePr(\gamma-1)\xi^2}\begin{Bmatrix} 0 \\ 0 \\ 0 \\ (2-\lambda)\tilde{T} + 2\dfrac{T_2}{T_1}T \end{Bmatrix} \tag{106}$$

To close the system, we have:

$$\tilde{p} = (\gamma - 1)(\tilde{E} - Uu_2 + \frac{\tilde{\rho}}{2}U^2) \tag{107}$$

Note that T_1 and T_2 are dimensionless temperatures associated with the Sutherland law. Thus, for a given n^{th} mode we can solve the continuity, radial-momentum, tangential-momentum, and energy equations to obtain the perturbation solution.

3.3. Boundary Conditions and Numerical Scheme

Very far away from the contact interface and past the primary shock, the disturbances must decay and thus the far-field boundary condition becomes:

$$r \to \infty : \qquad \{\tilde{\rho}, \tilde{\rho}U + \rho\tilde{u}, \rho\tilde{q}, \tilde{E}\} \to \{0,0,0,0\} \tag{108}$$

The inner boundary condition for the base flow is a reflecting wall at the origin; consequently, the inner boundary condition for the perturbation flow is also a reflecting wall at $\mathrm{r} = 0$. The base flow's reflecting boundary condition requires the radial velocity to be zero ($\mathrm{U} = 0$) at the origin, which leads to $\frac{\partial \mathrm{P}}{\partial \mathrm{r}} = 0$ in order to satisfy the radial momentum equation. Likewise for the perturbation flow, the vectorial velocity must also be zero ($\tilde{\mathrm{u}} = 0$ and $\tilde{\mathrm{q}} = 0$) which leads to $\frac{\partial \tilde{\mathrm{p}}}{\partial \mathrm{r}} = 0$ in order to satisfy the radial momentum equation.

3.3.1. The Numerical Scheme

A finite volume approach is employed to solve the viscous system of perturbation equations. The flux is calculated by applying the Roe-Pike scheme (Roe-Pike 1999). Gradients are calculated using a Weighted Essentially Non-Oscillatory scheme (WENO) that is second order accurate (Jian and Shu, 1996; Haselbacher 2005). The time evolution is according to the classical fourth order Runge-Kutta method.

3.3.2. Extension of the Roe-Pike Method

The Roe-Pike scheme is extended here for the perturbation flow. There are three major steps in the Roe-Pike Method. The first of which involves writing the equation in a semi-linear form by defining a Jacobian $\boldsymbol{A} = \frac{\partial \boldsymbol{F}}{\partial \boldsymbol{U}}$ for some ‚average' values of the quantities and calculating the Eigen values/vectors of the Jacobian in terms of these average quantities. The second step is decomposing the jumps across the discontinuity in terms of the Eigen vectors, K as $\Delta\boldsymbol{U} = \sum_{i=1}^{4} \alpha_i \boldsymbol{K}_i$, and finding the weights α in terms of the averaged quantities. Lastly, find the average quantities that satisfy the flux-difference formula. The Jacobian $\boldsymbol{A}$ for the perturbation equations is identical to the Jacobian of the Base flow Equations. Hence, the Eigen values and Eigen vectors of $\boldsymbol{A}$ are also the same. Proceeding onto the second step of calculating the wave strengths, a system of four algebraic equations for α_i in terms of $\Delta\boldsymbol{U}$ is formed:

$$\Delta\boldsymbol{U} = \sum_{i=1}^{4} \alpha_i \boldsymbol{K_i} \tag{109}$$

The solution to the system yields the perturbation weights which are given as:

$$\alpha_2 = \frac{\gamma - 1}{a_a^2}\left[\Delta u_1 \left(\frac{H_a}{\rho_a} - U_a^2\right) + U_a \Delta u_2 - \Delta u_4\right] \tag{110}$$

$$\alpha_1 = \frac{1}{2a_a}[\Delta u_1(U_a + a_a) - \Delta u_2 - a_a\alpha_2] \tag{111}$$

$$\alpha_4 = \Delta u_1 - (\alpha_1 + \alpha_2) \tag{112}$$

$$\alpha_3 = \Delta u_3 \tag{113}$$

Here, the subscript a is used to denote an average between the right and left states.

The equations obtained for the perturbation's weights α have the same form as that of nonlinear Euler equations (Toro, 2009). However here, $\Delta\boldsymbol{U}$ denotes the perturbation's jump across the discontinuity rather than the base flow's jump. Roe-Pike also presented an approximate formula for the weights in terms of the characteristic variables; it is possible to derive such an approximate formula for the perturbation equations as well. For either form of the perturbation weights, the „averaged' base flow quantities are determined in the third and last step. Following Roe-Pike's method, the „average' value is determined such that the flux difference equation is satisfied.

$$\Delta\boldsymbol{F} = \sum_{i=1}^{4} \alpha_i\lambda_i\boldsymbol{K}_i \tag{114}$$

For the base flow's weights, Roe and Pike showed that the approximate characteristic weights satisfy the flux difference equation for any definition of an average. In other words, so long as the averaged value falls between the right and left values the flux difference is satisfied. Upon repeating the same process for the perturbation's characteristic weights, the conclusion is the same. Unlike the approximate characteristic weights, the more accurate weights demand that the average be defined as:

$$\rho_a = \sqrt{\rho_R\rho_L} \tag{115}$$

$$U_a = \frac{\sqrt{\rho_R}U_L + \sqrt{\rho_L}U_R}{\sqrt{\rho_R} + \sqrt{\rho_L}} \tag{116}$$

The remaining averaged parameters required to compute the perturbation weights are averaged in the same fashion as the base flow's velocity. Now that flux difference is computed, the flux at the face can be evaluated by:

$$\boldsymbol{F}_F = \frac{1}{2}(\boldsymbol{F}_L + \boldsymbol{F}_R) - \frac{1}{2}\Delta\boldsymbol{F} \tag{117}$$

Notice that the perturbation equations' Jacobian was directly given in terms of only the base flow. Therefore, no additional approximation was needed. This is no surprise because the perturbation system was already linear, so there was no need for a quasi-linear form.

3.3.3. Inner Boundary Numerical Implementation

At the inner face, solely by requiring that $U = 0$, $\tilde{u} = 0$, and that $\tilde{q}$ is nonsingular the fluxes at the face reduce to:

$$\boldsymbol{F} = \begin{Bmatrix} \tilde{\rho}U + \varrho\tilde{u} \\ 2Uu_2 - \tilde{\rho}U^2 + \tilde{p} \\ Uu_3 \\ \tilde{u}H + U\tilde{H} \end{Bmatrix} \rightarrow \begin{Bmatrix} 0 \\ \tilde{p} \\ 0 \\ 0 \end{Bmatrix} \tag{118}$$

The condition that the perturbation pressure's gradient is zero is enforced through the flux, since the pressure at the face is set equal to the cell centered value. The $\tilde{q} = 0$ condition is reinforced by refraining from solving the q-equation at the first node; instead, specify q at the first node as $\tilde{q} = \frac{2\tilde{u}}{\lambda}$ which is approximately zero. Especially for the inviscid case, reinforcing the tangential velocity condition is required to ensure the source terms are well behaved near the origin.

3.4. Results and Discussion

The results are presented in the following order: the base flow, the perturbation radial profiles and time history, the growth rate vs. wave number for various Atwood numbers, comparison with theoretical models, for a given Atwood number the effect of the Reynolds number, and the wrinkling of the contact interface. All the results presented are for a base-flow pressure ratio of 22, a temperature ratio of one, an adiabatic index γ of 1.4, and the initial location of the diaphragm is at 0.0254 m. The ambient temperature and pressure are 299 K and 1.0207 atm respectively. These operational parameters were chosen because several other studies use the same operational parameters, since the earliest work by Brode (1955). For example, Freidman (1961) also used the same operating conditions.

All the results presented herein are dimensionless and have been normalized as specified in the formulation section. In order to highlight the direct effect of viscosity on the perturbation flow the base flow's Atwood number must be unchanged. Hence, the viscous perturbation results are compared with the inviscid perturbation results, while the base flow is considered inviscid in both cases to keep the Atwood number constant. Additionally, for all the results presented the thermal conductivity is neglected; thus, Prandtl number is taken to be infinity.

3.4.1. The Base Flow

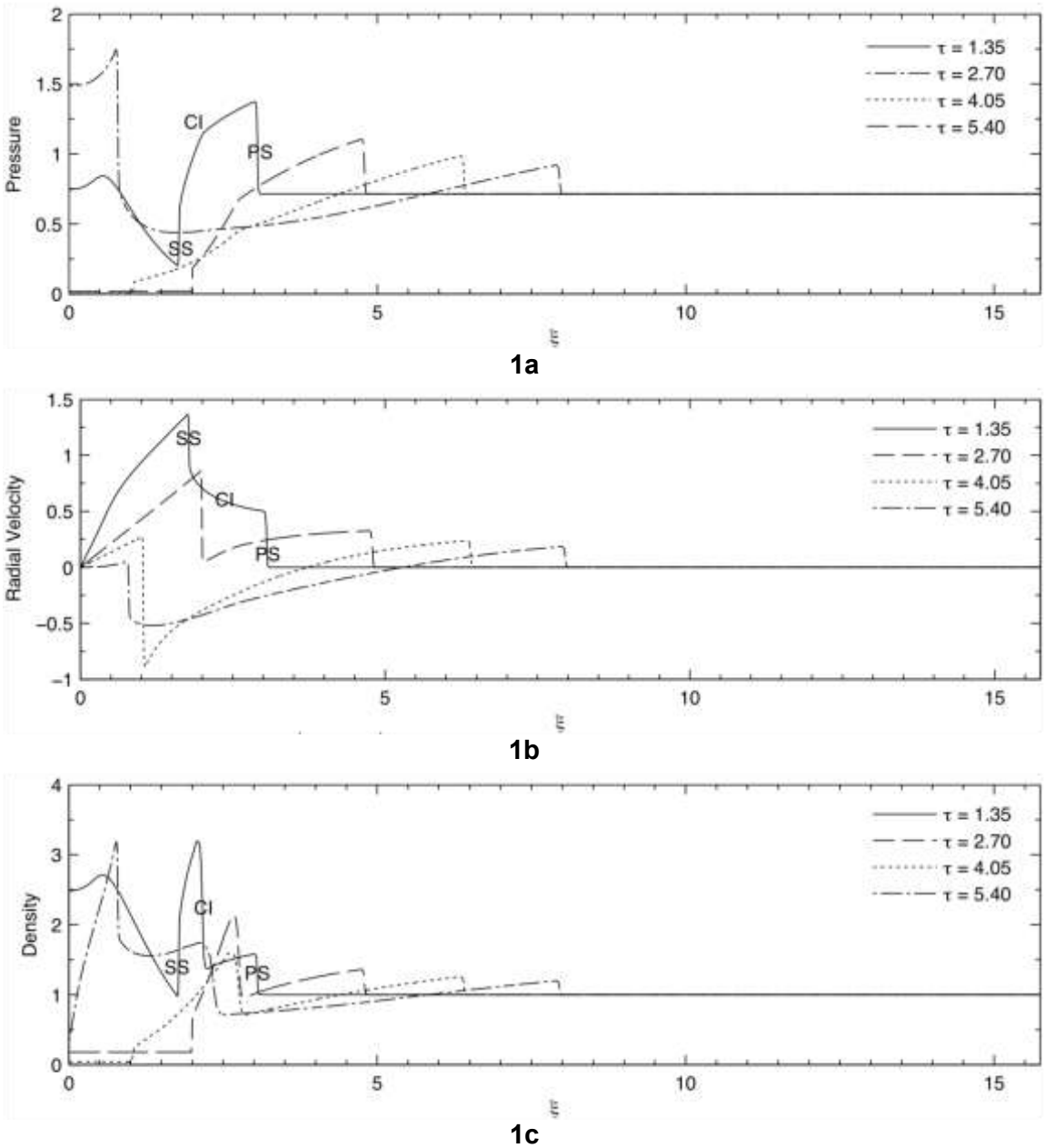

Figure 3–1. The radial dependence of (a) pressure, (b) radial velocity, and (c) density of the base flow at 4 different non-dimensional times. The location of the primary shock (PS), secondary shock (SS) and contact interface (CI) are most evident in the density profile and are marked. The above results are obtained with a discretization of 2000 uniform grid points extending up to a radial location of ξ = 15.75.

Figure 3–1 shows the pressure, velocity, and density of the base flow as a function of r at various times. The pressure and velocity jumps across both the Primary Shock (PS) and the secondary shock (SS) are clear in Figure 3–1a and Figure 3–1b respectively. The pressure and velocity are continuous across the contact interface (CI) or contact surface (CS), but the density is discontinuous, which is evident in Figure 3–1c. The secondary shock corresponds to the inner

discontinuity in pressure and velocity. However, unlike the primary shock; it moves inward then reflects off the origin.

Figure 3–2a depicts the location of the discontinuities as a function of time. During the time range between [1, 4.5] the contact interface's path is approximately parabolic, consequently the deceleration of the CI is constant for this time range. The secondary shock's first reflection happens at the dimensionless time, $\tau = 4.6$. Once the SS is reflected it continues to move outward until it hits the CI creating a tertiary shock while undergoing Richtmyer-Meshkov Instability (RMI) (Richtmyer 1960; and Meshkov, 1969). Recall our focus is on studying the RT instability of the CI. Therefore, the time domain of interest is up to $\tau = 5.4$ in order to isolate the RTI mechanism from the RMI mechanism.

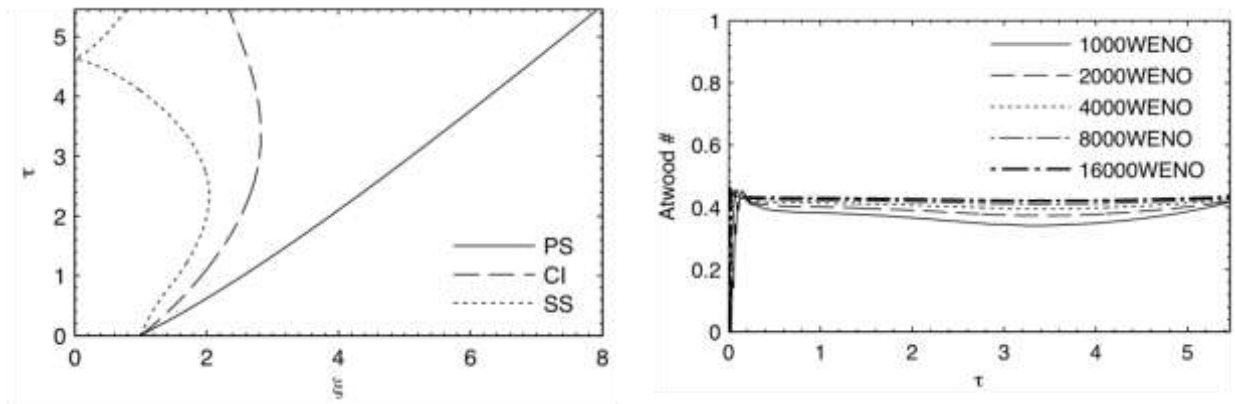

2a **2b**

Figure 3–2. a) ξ-τ Diagram of the location of the contact interface, primary shock, and secondary shock. b) Grid independence of the Atwood number.

The behavior of the base flow with increasing numerical resolution is critical when studying the behavior of the perturbation flow. The ξ-τ Diagram is completely grid independent and as a result the CI's velocity and acceleration are also grid independent. On the other hand, Figure 3–2b illustrates the effect of refining the computational grid on the Atwood number which is relevant to the instability study. From Figure 3–2b, it is clear that the Atwood number converges as the number of points increases; however, complete convergence for a perfect discontinuity cannot be achieved in shock capturing. With increasing resolution the discontinuity will continue to be resolved sharper and sharper. The time averaged Atwood numbers of (0.3575, 0.3839, 0.4023) correspond to a resolution of (1000, 2000, 4000) points for the radial domain using WENO.

3.4.2. The Perturbation Solution

The perturbation results are initialized as an initial Gaussian distribution with a peak density equal to 1% of the base flow density, centered at the initial location of the diaphragm. The effect of the initial profile on the growth rate was found to be negligible. The initial flow adjustment is limited to the period $\tau < 0.5$ during which the inserted disturbance conforms to the appropriate spatial structure of the Eigen mode. The adjustment period is followed by an exponential growth range that lasts to about $\tau = 4.5$.

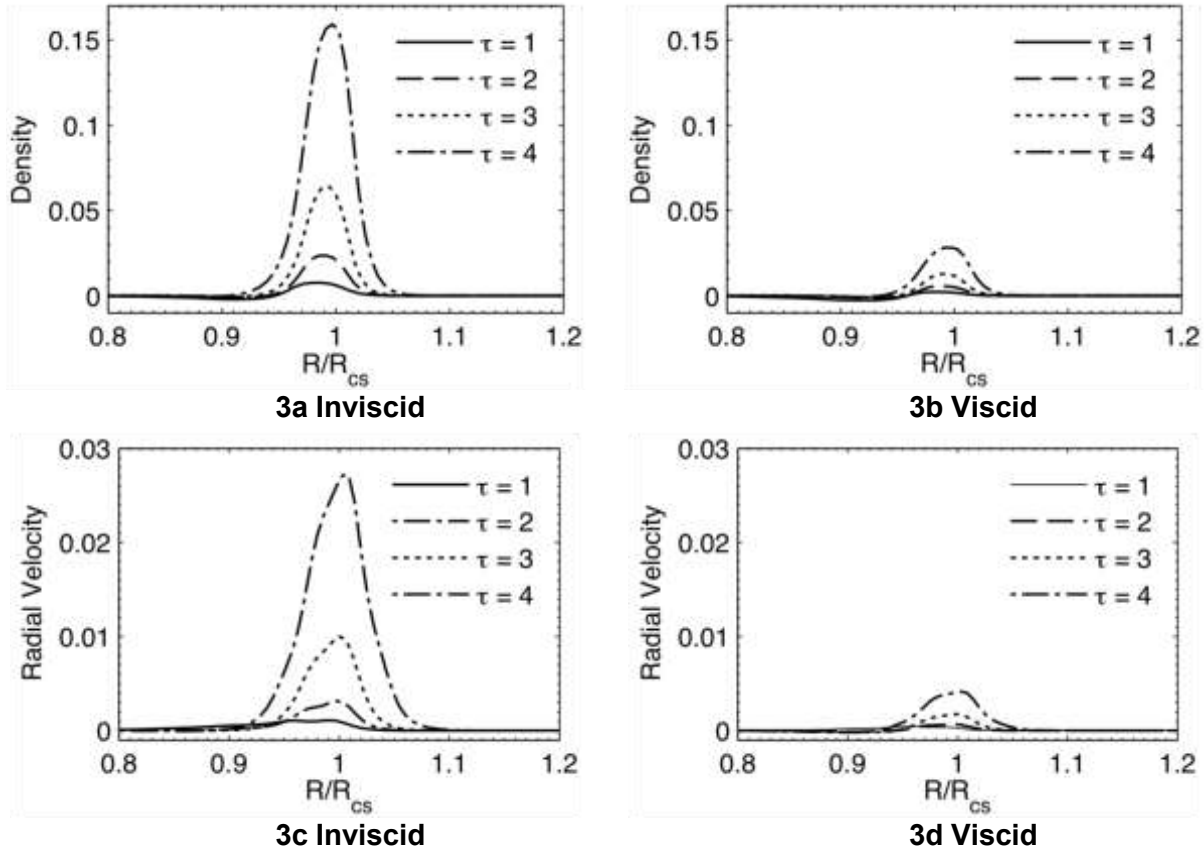

Figure 3–3. The radial shape of the perturbed flow's density and radial velocity for both the inviscid and viscid cases. The spherical wave number is 1862 and the Atwood number is 0.3575.

The radial profile of the perturbation is provided in Figure 3–3 and Figure 3–4 for various times. The perturbation density, temperature, and velocity have a Gaussian-like profile. Interestingly, the tangential velocity is much smaller than the radial velocity and switches sign around the CI, which is physically meaningful. It is clear that for a large spherical harmonic wave number, such as the one chosen for this figure, the viscosity has a strong effect and inhibits the growth rate when compared to the inviscid results.

Figure 3–5a shows the time evolution of the peak value of the perturbation radial velocity as obtained by both the inviscid and viscous stability analyses. In Figure 3–5b, At refers to Atwood number and WN refers to the spherical wave number. Here the plotted peak corresponds to the location of the contact interface for all time. The growth is exponential for the time range of [1.0 to 4.5]. Notice that the initial disturbance is well chosen, so that even at very early time, there hardly is any irregularity that could be discerned as the initial disturbance adjusting to the Eigen structure.

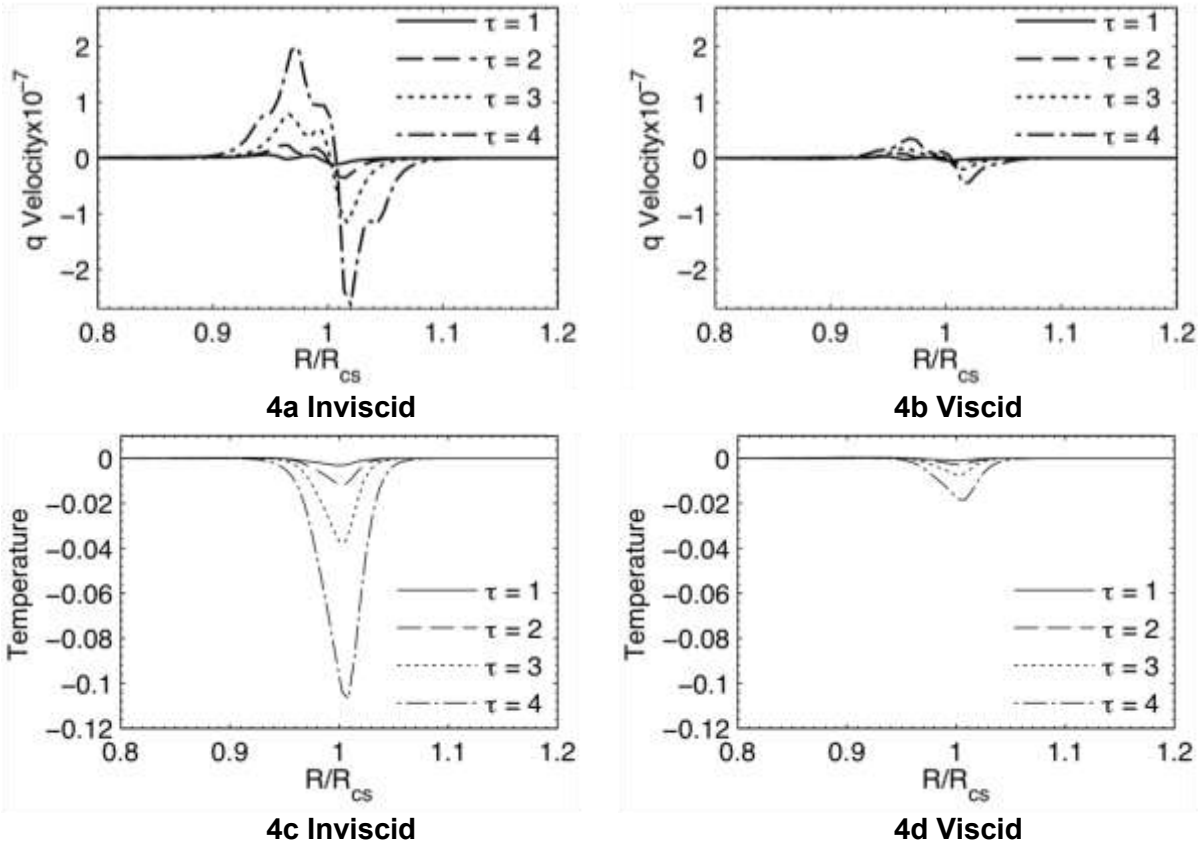

4a Inviscid 4b Viscid

4c Inviscid 4d Viscid

Figure 3–4. The radial shape of the perturbed flow's tangential velocity and total energy for both the inviscid and viscid cases. The spherical wave number is 1862 and the Atwood number is 0.3575.

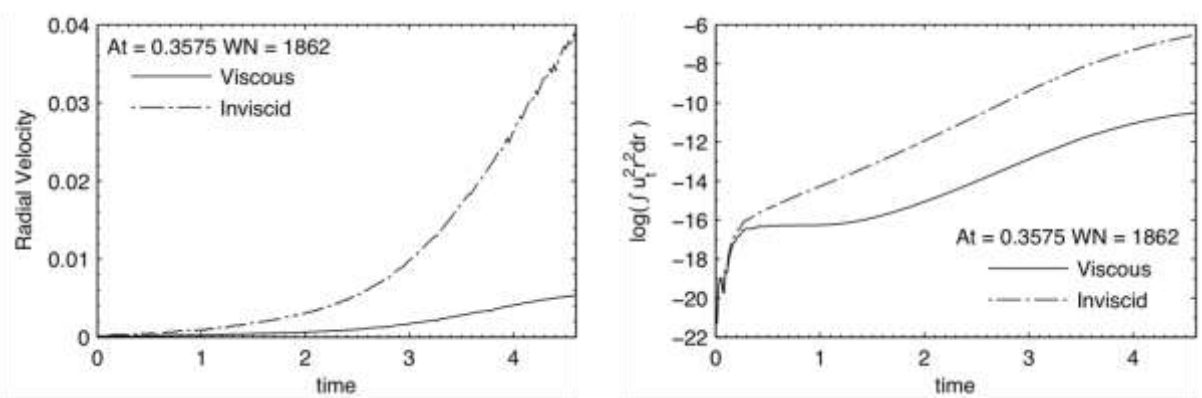

5a 5b

Figure 3–5. a) Viscous vs. inviscid evolution of the peak perturbation radial velocity. b) the growth of the inviscid perturbation vs. the viscous perturbation.

In the following the growth rate is obtained by performing the following volume integral at each time step:

$$I(\tau) = \int_{0.85R_{CI}(\tau)}^{1.15R_{CI}(\tau)} \tilde{u}^2(\xi, t)\xi^2 d\xi \tag{119}$$

Keeping track of this integral for all times is used to ascertain the growth rate of the perturbed flow. It can be thought of as the specific kinetic energy contribution strictly from the radial velocity or simply a radially averaged quantity. The effect of the viscous forces dampening the growth is evident in Figure 3–5b. In the inviscid limit, the growth is much higher than the growth predicted by viscous theory.

3.4.3. Effect of the Wave Number

Figure 3–6 presents the growth rate versus the wave number for both the inviscid case and the viscous case. For the inviscid case, initially the growth rate increases as the wave number increases until an asymptotic value is reached at high wave numbers. The base flow parameters such as Atwood number and the contact interface's width affect the growth rate. Since these parameters are affected by grid resolution as outlined before, the instability solution is influenced as well as shown in Figure 3–6. However notice that in Figure 3–6, the pattern of growth rate dependency on the wave number is the same for various Atwood numbers. Yet the asymptotic values reached for very high wave numbers are dependent on the Atwood number. This is actually not a numerical shortcoming, but rather reflects the physics. A higher Atwood number means a sharper discontinuity and hence a higher growth rate.

The viscous effects are negligible for low wave numbers and their significance is only seen at large wave numbers. The viscous effects stifle the perturbation's growth and consequently a maximum growth rate is achieved. For a Reynolds number of 6.2 x 105, a spherical wave number around 400 corresponds to the maximum growth rate predicted by viscous theory. Unlike viscous theory, inviscid theory predicts no change in the growth rate as the wave number goes to infinity.

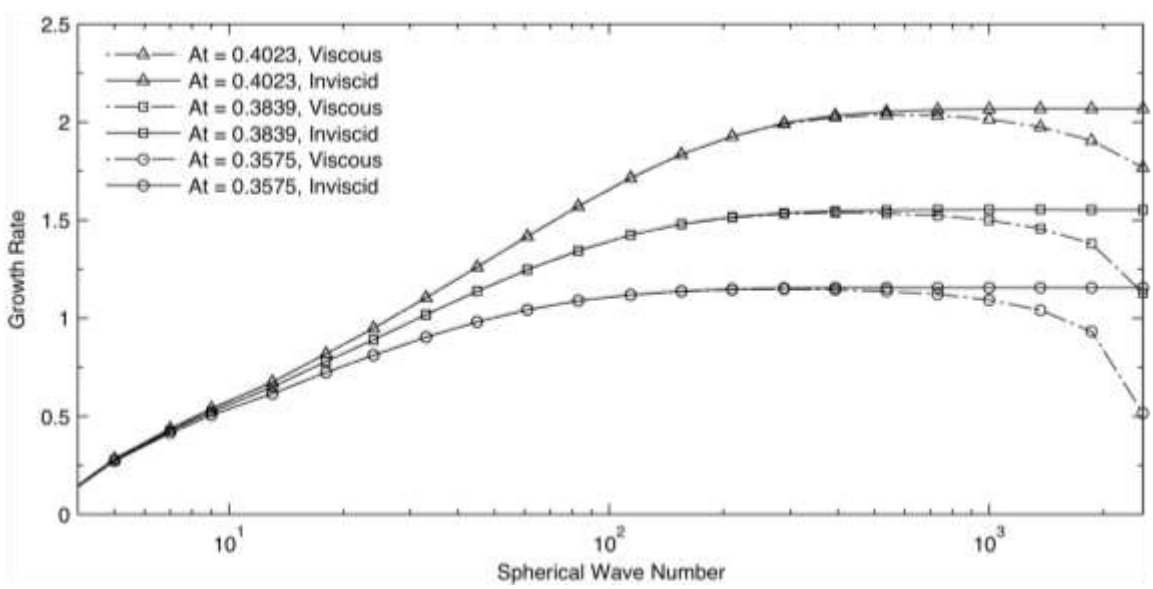

Figure 3–6. The global growth rate vs. the wave number for various Atwood numbers at a Reynolds number of 6.2 x 105.

3.4.4. Comparison with Theoretical Models

In order to identify the mechanisms involved and the validity of the assumptions made in modeling the viscous fully compressible instability, a comparison with previous theoretical models is presented in Figure 3–7. The comparison is performed for the viscous simulation corresponding to an Atwood number of 0.4023 and a Reynolds number of 6.2x105. We compare our results in Figure 3–7 with the theoretical incompressible models of Plesset (1954), Chandrasekhar (1981), and Lin et al. (2002). Plesset model is for a spherical RTI in bubble collapse and does not account for the viscous effects, but is included as a reference to help identify the viscous effects. Chandrasekhar model include the viscous effects, but it is for the plane, incompressible RTI. Lin et al. model, as in Plesset, considers RTI in the case of the bubble collapse but accounts. These three models for the incompressible case consider the global instability in that they accounts for the boundary conditions.

For all of these models, as well as our simulation, we note that for wave numbers less than 25, the growth rate is proportional to the square root of the wave number. As the wave number increases, our computation begins to deviate from these models. Our simulations indicate that a maximum growth rate is reached at a wave number of about 400. As our simulations predict the Lin et al. model and the Chandrasekhar model also illustrates the viscous effects at high wave numbers inhibiting the perturbation's growth.

In addition to the viscous or spherical effects considered in the previous models, our simulations account for full compressibility effects as well as the interface's thickness effects. Our predicted peak amplification rate is lower than that of the incompressible models. To validate our results, we also present in the Figure 3–7 the local growth rate predicted by Bandiera (1984) which is valid only for high wave numbers. Bandiera's model is a simple local model based on only the local pressure and density gradients, but as shown in the figure it predicts almost the same peak growth rate as our simulations.

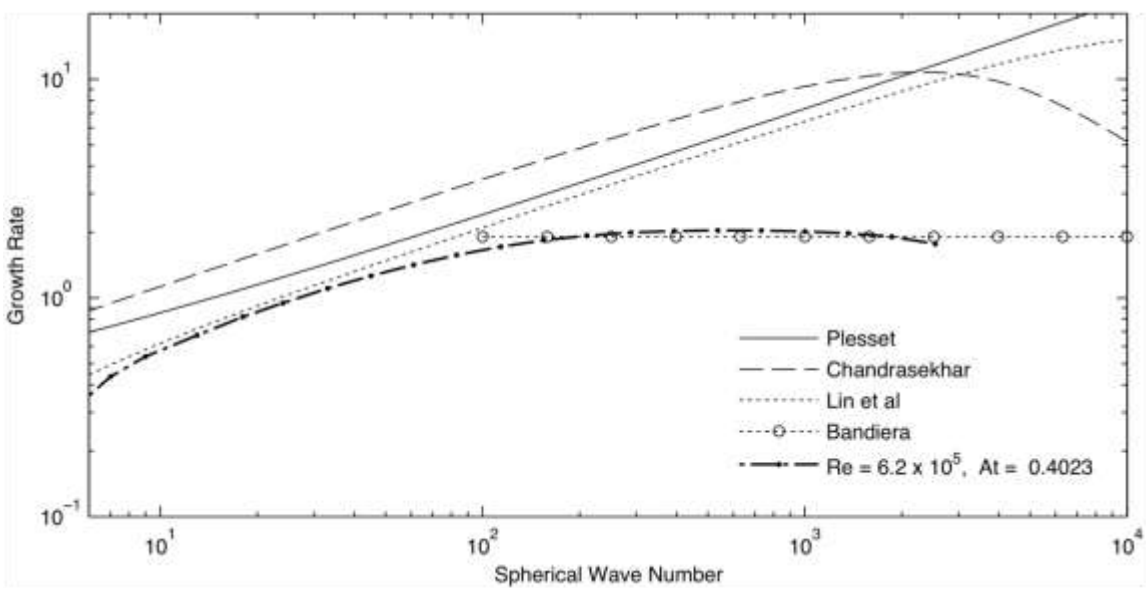

Figure 3–7. The effect of the wave number on the growth rate.

3.4.5. The Effect of the Reynolds Number

Figure 3–8 demonstrates the effect of the Reynolds number on the growth rate for a given Atwood number. For low wave numbers the Reynolds number has no effect on the growth rate. Consequently, the growth rate predicted for wave numbers less than 45 did not change as the Reynolds number went from 6.2 x 10^5 to 10^4. However, for high have numbers, as the Reynolds number decreases the peak growth rate and its corresponding wave number also decrease. As the Reynolds number is reduced from 6.2 x 10^5 to 10^4, the peak growth rate is reduced from 1.15 to 1.07 and its corresponding wave number also reduced from 400 to 100. For the limiting case of very large Reynolds number ($Re \rightarrow \infty$), the inviscid solution is recovered where the growth rate saturates and does not decline for very large wave numbers. The low-Reynolds number cases may be taken as an approximation to the turbulent flow case, in which the presence of turbulence can be modeled by an eddy viscosity that increases the effective Reynolds number.

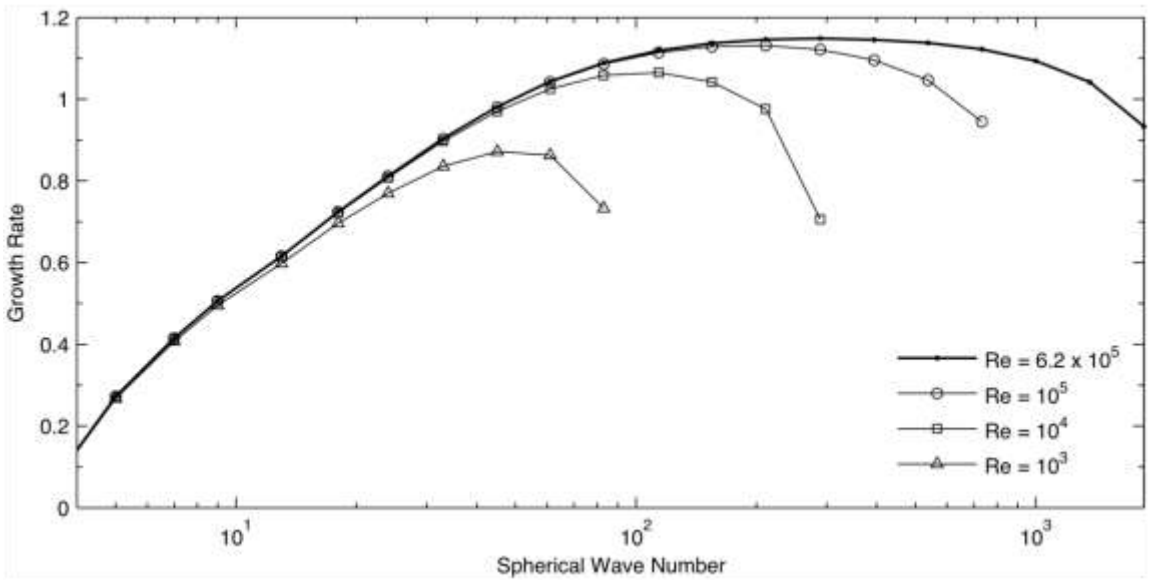

Figure 3–8. The effect of the Reynolds number on the growth rate for an Atwood number of 0.3575.

3.4.6. The Wrinkling of the Contact Interface

Figure 3–9 paints the density contours at various time intervals. The total density is obtained by adding the base flow density and the perturbation density. The latter is not only function of time and r, but also a function of θ and φ. The results shown in Figure 3–9 are for l = 40, m = 1. The wrinkling increases with time and due to the exponential growth of the disturbances it is particularly evident at late times. The wrinkling of the contact interface is evident in the contours. However, the surfaces of the primary and secondary shocks are still purely spherical because they are stable at this wave number.

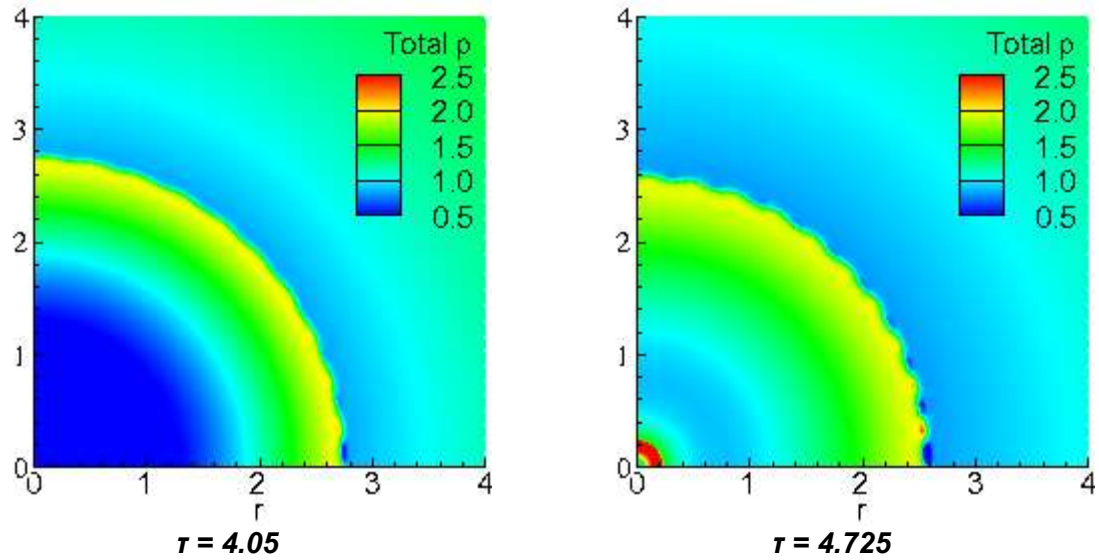

Figure 3–9. The total density of the interface for a wave number of 40 and Atwood number of 0.4039.

3.5. Conclusions

We have presented herein the fully compressible-viscous-spherical linear stability analysis of the spherical contact interface associated with the sudden release of a high-pressure gas initially contained in a small spherical region. A high-order WENO scheme was employed to capture both the base flow and the perturbed flow. The numerical scheme is able to predict a sharper discontinuity with increasing grid resolution without introducing numerical noise around the discontinuity.

The radial profiles of the perturbation density, temperature, and radial velocity were found to be Gaussian-like with a peak around the contact interface, while the tangential velocity switches sign around the contact interface. The peaks of these profiles are reduced in the viscous case as compared to the inviscid one. For the inviscid case, as the wave number increases the growth rate increases until it saturates at very large wave numbers. Unlike the inviscid case, the viscous case predicts a maximum growth rate around a spherical wave number of 400 for a Reynolds number of 6.2 x 105. As the Reynolds number decreases, the maximum growth rate and its corresponding wave number both decrease.

The present analysis provides an explanation of the viscous mechanism. We note that the viscous terms in the perturbation equations include $\lambda = n(n+1)$, where n is the spherical wave number. Thus, only at high wavenumbers the viscous effects becomes important and is proportional to the square of the wavenumber. Such high wave numbers correspond to a small wavelength, hence, would require a prohibitive number of grid points in both angular directions if we attempt to capture them by nonlinear direct numerical simulations. The linearization process, however, enables us to eliminate the need to resolve the angular dimension, thus were able to properly capture the viscous effects at high-wave numbers.

4. FUTURE WORK: SIMULATIONS OF THE EFFECTS OF SOLID PARTICLES ON FLOW INSTABILITY IN DETONATIVE COMBUSTION

Our goal is to extend the work performed in Chapter 2 and Chapter 3 to account for the presence of particles. The instability resulting from the presence of a gas-particle interface in close proximity to the contact interface is a rich problem that many researchers are interested in understanding.

4.1. Introduction

4.1.1. Significance of the Problem

The stability of a material interface (MIF) is significant in several applications, but we will focus our discussion herein on its role in combustion and in industrial explosions. There are two common types of combustion: deflagration (flame propagation is subsonic), and detonation (flame propagation is supersonic). When detonation occurs, a shock wave is formed that increases the temperature and pressure of the driven gas and induces a flow in the direction of the shock wave but at lower velocity than the lead wave. Simultaneously, a rarefaction wave travels back into the driver gas. The interface separates the driven and the driver gases is referred to as the contact surface or interface and separates the fuel mixture from the combustion products. Figure 4–1 shows an experimentally observed Rayleigh-Taylor Instability (1950) (RTI) in which spherical cellularity develops on the surface of a spherical expanding flame. This stability can be influenced by the presence of small solid particles and, thus, can be used to enhance the combustion process.

Industrial explosions can happen accidentally or intentionally. Cant et al. (2004) provides an excellent review of CFD applications in modeling large explosions in nuclear and petrochemical industries. An example of designed explosion is that of a rocket lift-off. Such explosions are associated with a contact surface behind the shock. The stability of this interface affects the explosion process. Spraying solid particles have been proposed as an effective means for blast mitigation (Schwer and Kailasanath, 2003).

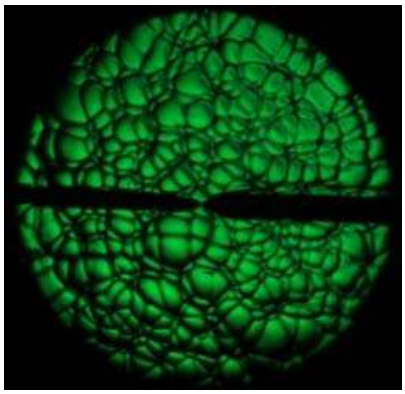

Figure 4–1. Observed Cellularity Developing on the Surface of a Spherically-Expanding Flame (Marshall et al. 2010).

4.1.2. Review of Recent Work

Frost et al. (2005) have conducted a series of experiments to demonstrate the effect of including solid particles on explosive detonations. Figure 4–2 shows a time series of developing the combustion products: on the left, heterogeneous charge contained zirconium particles and to the right homogeneous charge contained only sensitized Nitro Methane (NM) charges. Time between photographs for (a) is 0.5 ms, whereas the times for the photographs in the right figure are 0.2, 0.4, 0.6, 1.0, and 2.5 ms, respectively. In both cases, perturbations are evident on the surface of the fireball at early times. However, the perturbations are more regular and persist for a longer time for the heterogeneous charges. Frost et al. have attempted to interpret Figure 4–2 as a result of the reduced deceleration of metalized fireballs compared to the homogenous explosives; hence, the perturbation will persist longer.

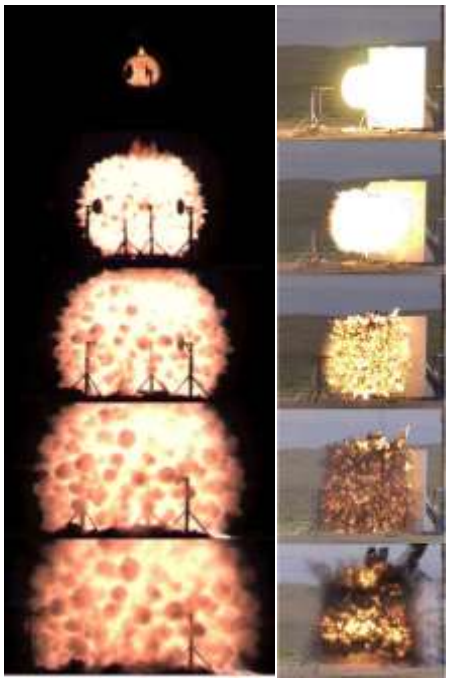

Figure 4–2. Frost et al. Experimental Results.

Balakrishnan and Menon (2010, 2011) have conducted 3D nonlinear simulations of the flow-field subsequent to the detonation of a spherical charge of TNT including the presence of reactive solid particles. Considering the symmetry of a spherical explosion, only a sector of the explosion was modeled. RTI ensues on the contact interface that separates the inner detonation products from the outer shock-compressed air. Upon growth with time, a mixing layer forms where the detonation products afterburn due to the inclusion of additional air. In Figure 4–3 from Balakrishnan and Menon the black dots represent the steel particles in the NM charge. A most interesting phenomenon to note is that in part a of the figure one can clearly see Rayleigh-Taylor structures forming in the mixing layer. At this early time the particles have yet to reach the surface. At a later time in part b, the particles overrun the interface. According to Balakrishnan and Menon, there must be two types of perturbation: one without the particles the other involves the particles. They have also pointed out the mixing layer stretches wider for the particle cases as compared with the baseline particle-free case.

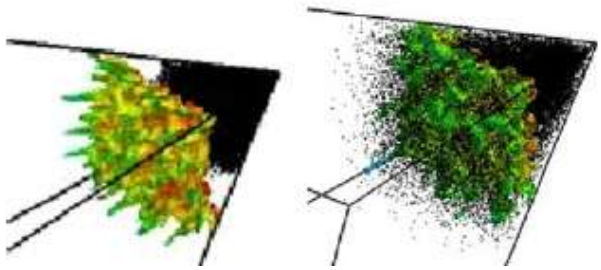

3A 3B

Figure 4–3. Sector of a sphere from Balakrishnan and Menon (2011), parts A and, B are the simulated iso-surfaces of the mixing layer.

(The time stamps for parts a and b are 0.13 and 0.58, milliseconds respectively.)

Mankbadi and Balachandar (2011) have used a high-fidelity scheme to study the flow instability resulting from the sudden release of a high pressure gas contained in a small sphere and followed its time evolution in an effectively spherical shock tube representing a detonative combustion. Their work is extended here to include the presence of solid particles that results in a second interface separating the mixture from the pure gas. In the formulation section, we discuss the basic flow, the splitting approach adopted, and the governing equations for the base and perturbations flows. In the results section, we discuss the base flow development in the absence or presence of solid particles. The results for the perturbation flow are first presented for a simplified analytical model of two interfaces in the proximity of each other's representing the two distinct interfaces characteristic of the presence of solid particles in the shock-tube problem. Further numerical results will be presented later followed by the summary and conclusion section.

4.2. Formulation

4.2.1. Description of the Flow

Figure 4–4 from Ling et al.(2010) depicts the flow regimes. Following the detonative combustion, a forward propagating shockwave is formed that separates the ambient region (0) from behind the shock (1). Simultaneously, a rarefaction wave travels back into the driver gas which develops into a shock due to the converging geometry between regions (3) and (4). An interface develops that separates the driven and the driver gases between regions (1) and (2). Upon the inclusion of solid particles, a second material interface develops that separates the gas-solid mixture from the gas between regions (2) and (3).

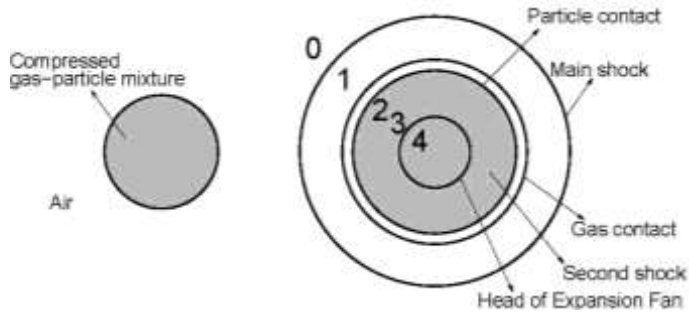

Figure 4–4. Schematic Illustration of Explosive Dispersals from a Spherical Charge Containing Gas-Particle Mixture (Ling et al, 2010).

4.2.2. Direct versus Splitting Approaches

In Direct Numerical Simulations (DNS) the full Navier-Stokes equations are solved directly with fine resolution enough to resolve all the relevant scales. For almost all attempts of direct simulations to address the present problem, the computer limitations allow only resolving a small range of scales. Therefore, such attempts are effectively some sort of Implicit Large-Eddy Simulations (ILES). There are several recent ILES of the present problem with no solid particles. This includes: Fraschetti et al. (2010) who have considered the Rayleigh-Taylor instabilities that are generated by the deceleration of a supernova remnant during the ejecta-dominated phase. Also, Kuhl et al. (2011) have simulated combustion in confined TNT explosions using an ILES approach coupled with an adaptive mesh refinement. They have concluded that the dominant effect that controls the rate of TNT combustion with air is the turbulent mixing rate.

The alternative to ILES is the splitting technique in which each flow parameter is split into a basic component and a perturbations one. Separate equations are solved for the base flow and another set of equations are solved for the perturbations flow. The later set is linearized, and therefore, the nonlinear effects are lost. Our focus here is on the instability waves, which according to the classical RT theory is more amplified at high-wave numbers (small wave length), which cannot be captured by DNS or ILES due to the resolution requirements. As such, we adopt here the splitting approach in which each total flow parameter is split into a base flow and a fluctuation component. The base flow is essentially one-dimensional spherical, and can be predicted effectively. New equations are then developed for the perturbation part of the flow. Upon, linearizing these equations, it is then possible to use a spherical harmonic decomposition to reduce the physically 3-D perturbations into an effectively 1-D system of equations. This will be discussed further in section 2.4 below.

4.2.3. Base Flow Governing Equations

The governing equations of the gas phase are conveniently expressed in the Eulerian frame of reference, while that of the particles flow is usually described using a Lagrangian frame of reference. However, we follow here a recent approach by Ling et al. (2009, 2010) which adopts an Eulerian approach for the particles as well. As in Ling et al. we consider the sudden release of a compressed air including particles initially contained in a spherical diaphragm of a small radius Ri. The following assumptions are made: (1) the fluid is a perfect gas; (2) the fluid motion may be regarded as inviscid, so its viscosity and conductivity are neglected except in the interaction with the particles; (3) the particles are inert, rigid, and spherical; (4) the particles have constant

heat capacity and uniform temperature distribution; (5) the volume fraction of the particles is negligible; (6) the only force acting on the particles is the viscous drag force; (7); the particles do not collide with each other. The mass, momentum and energy equations of the gas phase can be written as:

$$\frac{\partial}{\partial t}\begin{Bmatrix} \varrho\, Y^g \\ \varrho\, Y^g\, u^g \\ \varrho\, Y^g\, E^g \end{Bmatrix} + \frac{\partial}{\partial r}\begin{Bmatrix} \varrho\, Y^g\, u^g \\ \varrho\, Y^g\, (u^g)^2 + p^g \\ \varrho\, Y^g\, H^g\, u^g \end{Bmatrix} + \frac{2}{r}\begin{Bmatrix} \varrho\, Y^g\, u^g \\ \varrho\, Y^g\, (u^g)^2 \\ \varrho\, Y^g\, H^g\, u^g \end{Bmatrix} = -\begin{Bmatrix} 0 \\ f^p \\ u^p f^p + q^p \end{Bmatrix} \tag{120}$$

Here Y^g, u^g, p^g, E^g, and H^g represent gas's mass fraction, velocity, pressure, total energy, and total enthalpy, respectively. Note that ϱ is the mixture density; it is not identical to the gas density. The superscripts g and p represent the gas and particle phase respectively. To close the system, the total enthalpy of the gas H^g is given by:

$$H^g = E^g + \frac{p^g}{\varrho\, Y^g} \tag{121}$$

The corresponding mass, momentum, and energy equations of the particle phase in an Eulerian frame of reference are:

$$\frac{\partial}{\partial t}\begin{Bmatrix} \varrho\, Y^p \\ \varrho\, Y^p\, u^p \\ \varrho\, Y^p\, E^p \end{Bmatrix} + \frac{\partial}{\partial r}\begin{Bmatrix} \varrho\, Y^p\, u^p \\ \varrho\, Y^p\, (u^p)^2 \\ \varrho\, Y^p\, E^p\, u^p \end{Bmatrix} + \frac{2}{r}\begin{Bmatrix} \varrho\, Y^p\, u^p \\ \varrho\, Y^p\, (u^p)^2 \\ \varrho\, Y^p\, E^p\, u^p \end{Bmatrix} = +\begin{Bmatrix} 0 \\ f^p \\ u^p f^p + q^p \end{Bmatrix} \tag{122}$$

The terms f^p and q^p that appear on the right-hand sides of the equations represent the drag force and heat transfer of the particle phase. The mixture density $\varrho = \varrho_m$ is related to the gas and solid densities by

$$\varrho_m = \varrho_g \varphi_g + \varrho_p \varphi_p \tag{123}$$

Here φ is the volume fraction. Thus, we have:

$$\varrho_m = \varrho_m Y_g + \varrho_m Y_p; \qquad Y_p + Y_g = 1 \tag{124}$$

The mass fraction Y is related to the volume fraction φ by the relations:

$$Y_p = \frac{\varrho_p \varphi_p}{\varrho_m}; \;\; Y_g = \frac{\varrho_g \varphi_g}{\varrho_m} \tag{125}$$

Since Y_p is usually less than 0.2, we can make the dilute flow approximations:

$$\varphi_g = 1; \qquad \varrho_m = \varrho_p \varphi_p + \varrho_g = \varrho_m Y_p + \varrho_g \tag{126}$$

4.2.4. The Perturbation Equations

For the time being we neglect the direct effects of the particles forces and heat transfer on the flow perturbations (but no on the base flow) and follow the same approach as in Mankbadi and Balachandar (2011). The starting point for deriving the perturbation equations is the fully compressible Navier Stokes equations in spherical coordinates. We begin by assuming that each flow quantity is composed of the base flow $(\mathrm{U}, \mathrm{V}, \mathrm{W}, \mathrm{P}, \varrho)$ and a perturbation $(\mathrm{u}', \mathrm{v}', \mathrm{w}', \mathrm{p}', \rho')$. Thus,

$$u = U + u';\ v = V + v';\ w = W + w';\ p = P + p';\ \rho = \varrho + \rho'; \tag{127}$$

Here (u', v', w', p', ρ') are the perturbation radial velocity, azimuthal velocity, zenithal (polar) velocity, pressure, and density, respectively. Upon substituting this split into the governing equations, neglecting the nonlinear terms, and subtracting the base flow equations, the linearized continuity is obtained. We then use Spherical Harmonic decomposition as follows. The total perturbation velocity is composed of two components: u' in the radial direction and $\boldsymbol{q}'$ for the tangential direction, where:

$$\boldsymbol{q}' = v'\,\widehat{\boldsymbol{\theta}} + w'\,\widehat{\boldsymbol{\phi}} \tag{128}$$

Here $\widehat{\boldsymbol{\theta}}$ and $\widehat{\boldsymbol{\phi}}$ are unit vectors along the azimuthal and zenithal (polar) directions respectively, and:

$$\boldsymbol{\nabla_T} = \frac{1}{r}\left(\widehat{\boldsymbol{\theta}}\,\frac{\partial}{\partial\theta} + \widehat{\boldsymbol{\phi}}\,\frac{1}{sin\theta}\,\frac{\partial}{\partial\phi}\right) \tag{129}$$

is the gradient in the tangential direction. Since the perturbations are linear, we can expand them along the $\widehat{\boldsymbol{\theta}}$ and $\widehat{\boldsymbol{\phi}}$ directions using the spherical harmonic functions as:

$$\boldsymbol{q}'(r, \theta, \phi, t) = \tilde{q}\,(r, t)\ r\,\boldsymbol{\nabla_T} Y_{nm}(\theta, \phi) \tag{130}$$

$$\begin{Bmatrix} \rho'(r,\theta,\phi,t) \\ u'(r,\theta,\phi,t) \\ p'(r,\theta,\phi,t) \\ E'(r,\theta,\phi,t) \\ H'(r,\theta,\phi,t) \end{Bmatrix} = \begin{Bmatrix} \tilde{\rho}(r,t) \\ \tilde{u}(r,t) \\ \tilde{p}(r,t) \\ \tilde{E}(r,t) \\ \tilde{H}(r,t) \end{Bmatrix} Y_{nm}(\theta,\phi) \tag{131}$$

Here, n = 0, 1, 2,… and m = 0, 1, 2,…, n. The spherical harmonic $Y_{nm}(\theta, \phi)$ of order n, m is given by:

$$Y_{nm}(\theta,\phi) = L_n^m(\theta)\, e^{im\phi} \tag{132}$$

Here $L_n^m(\theta)$ is the associated Legendre polynomial. Upon employing this decomposition the perturbation equations are obtained in the form:

$$\frac{\partial Y^g \tilde{\rho}}{\partial t} + \frac{1}{r^2}\frac{\partial[Y^g r^2\left(U^g\tilde{\rho} + \varrho\widetilde{u^g}\right)]}{\partial r} - Y^g\varrho\lambda\frac{\widetilde{q^g}}{r} = 0 \tag{133}$$

$$Y^g\varrho\left(\frac{\partial\tilde{u}^g}{\partial t} + \widetilde{u^g}\frac{\partial U^g}{\partial r} + U^g\frac{\partial\widetilde{u^g}}{\partial r}\right) + \frac{\partial\widetilde{p^g}}{\partial r} - \frac{\tilde{\rho}}{\varrho}\frac{\partial P^g}{\partial r} = 0 \tag{134}$$

$$Y^g\varrho\left(\frac{\partial\widetilde{q^g}}{\partial t} + U\left(\frac{\partial\widetilde{q^g}}{\partial r} + \frac{\widetilde{q^g}}{r}\right)\right) + \frac{\widetilde{p^g}}{r} = 0 \tag{135}$$

$$\begin{gathered}\frac{\partial Y^g\widetilde{(\varrho E)}}{\partial t} + \frac{1}{r^2}\frac{\partial\left(Y^g r^2 U^g\widetilde{(\varrho H)}\right)}{\partial r} + \tilde{u}^g\frac{\partial(Y^g\varrho H)}{\partial r} + \\ (Y^g\varrho H)\left[\frac{1}{r^2}\frac{\partial\left(r^2\widetilde{u^g}\right)}{\partial r} - \frac{\lambda\widetilde{q^g}}{r}\right] = 0\end{gathered} \tag{136}$$

where $\lambda = n(n+1)$. Here we have assumed that the mass fraction cannot be perturbed. Note that if Y^g does not vary in time and space but rather is taken to be a constant, then the above system of equations is identical to the gas-gas system.

4.3. Preliminary Results

We present the results for a specific case of a spherical container with an inside to ambient pressure ratio of 22 and a temperature ratio of 1. For simplicity we consider both the compressed gas and the ambient to be air with an adiabatic index γ of 1.4. Correspondingly, the initial inside to ambient density ratio is also 22. The ambient temperature and pressure are taken to be 299 K and 1.0207 atm respectively. The initial location of the diaphragm r_o was 0.0254 m. These operational parameters were chosen because several other prior studies have used the same spherical shock tube condition since the earliest work by Brode (1959). For this case we first briefly review the results of the base flow and then proceed to discuss the instability results

All the results presented herein are normalized as follows: the length scale is chosen to be the initial location of the spherical diaphragm separating the high pressure gas from the ambient air, thus, a dimensionless radial coordinate can be defined as $\xi = r/r_o$. The velocity and density are normalized by the ambient speed of sound and density respectively. The time scale τ is formed from the ambient speed of sound and the initial location of the diaphragm, hence, the dimensionless time is obtained as $\tau = (t\,a)/r_o$. Lastly, the pressure and total energy are normalized by ρa^2, where ρ and a are the density and speed of sound of the undisturbed ambient.

4.3.1. Base Flow

Figure 4–5 from Mankbadi and Balachandar (2012) shows the dimensionless pressure, velocity, and density of the base flow as a function of ξ at various times without including solid particles. The pressure and velocity jumps across both the primary shock (PS) and the secondary shock (SS) are clear in Figure 4–5b respectively. The pressure and velocity are continuous across the contact interface (CI), but the density is discontinuous, which is evident in Figure 4–5c. The primary shock moves only in the forward direction, while the secondary shock initially moves inward then reflects off the origin. The location of the maximum density derivative is used as an estimate for the contact interface's position denoted by R_{CI}.

Figure 4–6 depicts the location of the discontinuities as a function of time. As shown in Figure 4–6a, during the time range [0, 4] the contact interface's path is approximately parabolic, which suggests a constant deceleration of the CI. The secondary shock's first reflection happens at a dimensionless time, $\tau = 4.6$. Once the SS is reflected it continues to move outward until it interacts with the CI creating a tertiary shock. For now, we focus on studying the RT instability of the CI, before its interaction with the secondary shock. Therefore, the time domain of interest is up to $\tau = 5.4$ in order to isolate the RT mechanism. In Figure 4–6b, we normalize the radial distances by the location of the CI, thus showing the location of the shocks relative to the CI. It is clear that the secondary shock for an extended duration remains close to the contact at about 80% of its radial location; even the primary shock till about $\tau = 3.3$ remains within one radius of the contact's location. Thus, it is of interest to study how the RT instability of the CI is influenced by the presence of the two nearby shocks.

Before we show the effect of particles on the base flow, we first validate the new Eulerian-Eulerian approach. Figure 4–7 shows the gas and the particle velocities for the planar case in comparison with the corresponding standard ordinary-differential equation (ODE) solution. It matches very nicely for fine resolution. While the gas phase is characterized with the discontinuous jump, the particle velocity gradual increases. In the final manuscript we will present results to show that the spherical Eulerian case do match with the Lagrangian case.

5A

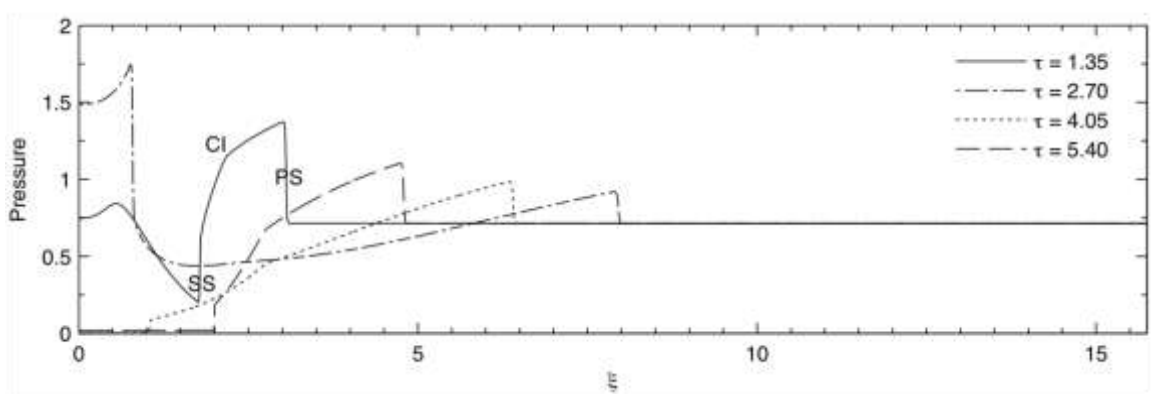

5B

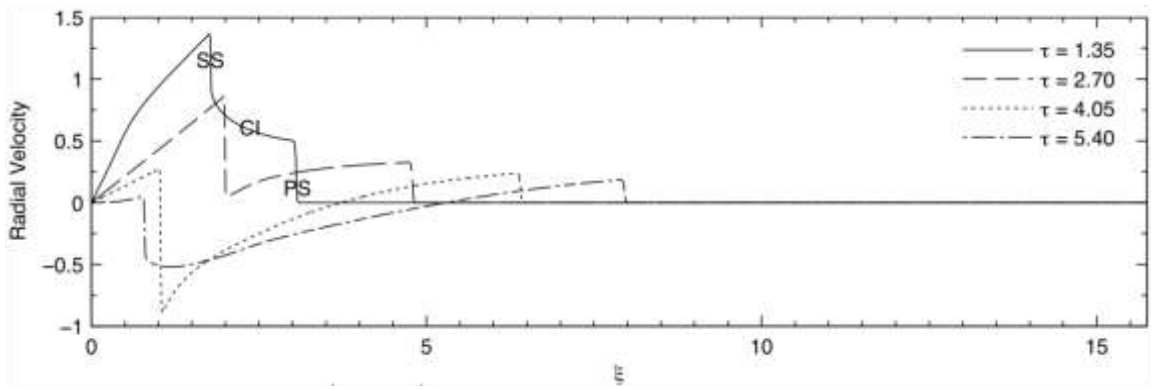

5C

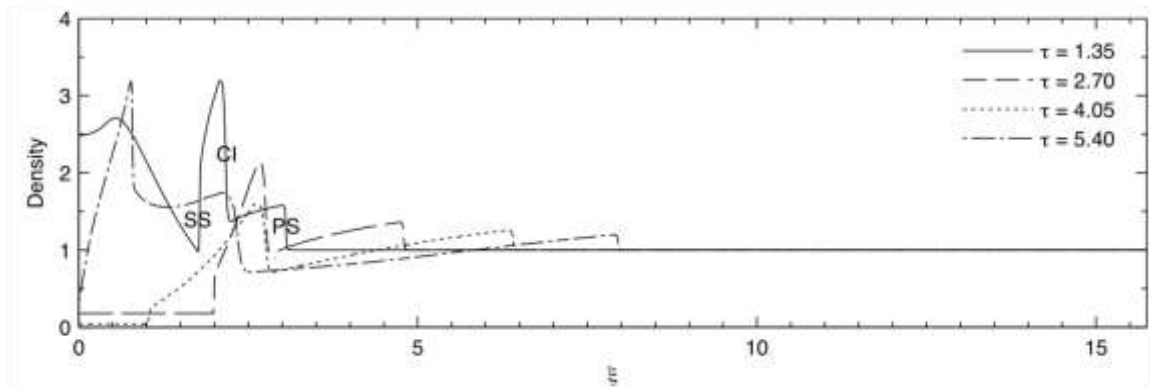

Figure 4–5. The radial dependence of (a) pressure, (b) radial velocity, and (c) density of the base flow at 4 different non-dimensional times. The location of the primary shock (PS), secondary shock (SS) and contact interface (CI) are most evident in the density profile and are marked. The above results are obtained with a discretization of 2000 uniform grid points extending up to a radial location of ξ = 15.75.

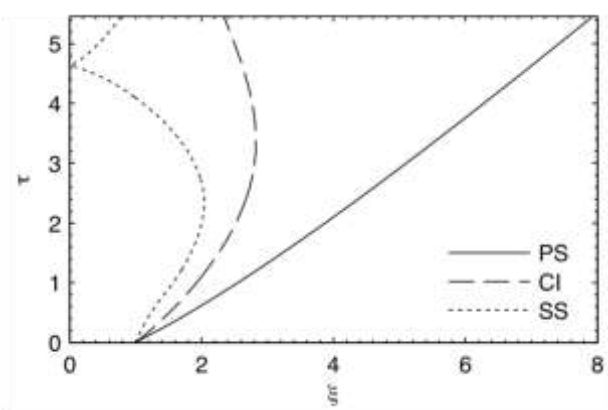

6a

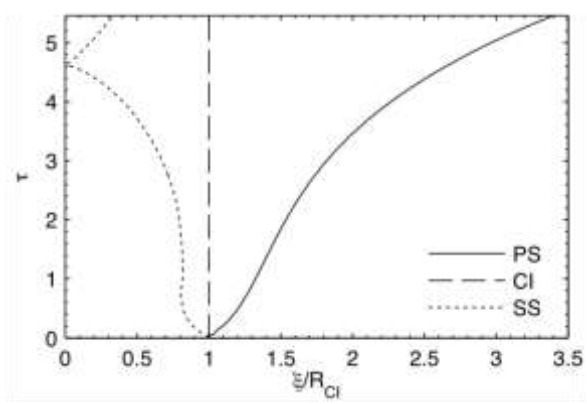

6b

Figure 4–6. ξ- τ Diagram of the location of the contact interface, primary shock, and secondary shock. In terms of the original non-dimensional location (6a), and rescaled by the location of the contact interface (6b).

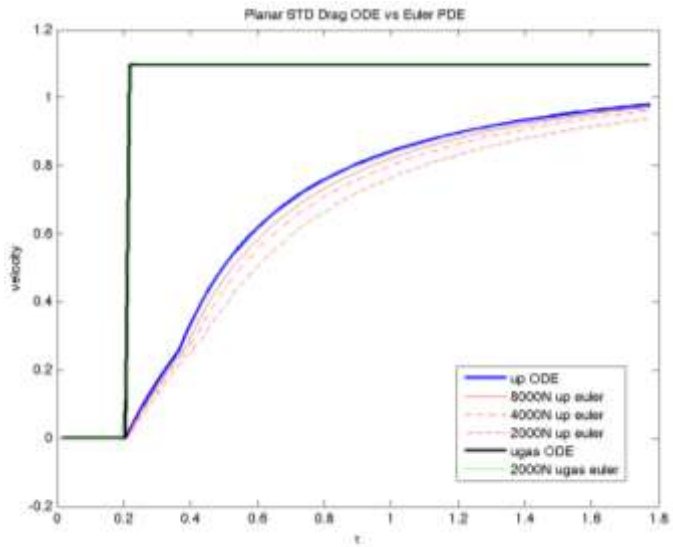

Figure 4–7. Numerically Predicted Gas and Particle Velocities in the Planar Case using the Eulerian Approach in Comparison with the planar Standard Drag ODE.

4.3.2. Preliminary Perturbation Flow- Analytical Solution for the Stability of Two Contact Surfaces

In the final manuscript we will present results for the flow instability in the presence of solid particles. In the meantime, we present here an analytical model for the instability of two adjacent contact surfaces representing the gas-gas interface, and the gas-mixture interface

ϱ_2

_____ Z=0

ϱ_1

_____ Z=-L

ϱ_0

Figure 4–8. A model of Two Contact Surfaces Distance "L" Apart where $\varrho_2 > \varrho_1 > \varrho_o$.

Consider the two contact interfaces illustrated above. The governing equations for each layer are:

$$u'_x + w'_z = 0 \tag{137}$$

$$u'_t = -\frac{1}{\varrho}\, p'_x \tag{138}$$

$$w_t' = -\frac{1}{\varrho}\, p_z' \tag{139}$$

A stream function is introduced:

$$\psi' = \phi(z) e^{ikx - i\omega t} \tag{140}$$

Upon substituting into the two momentum equations, the solution at each region is obtained in the form:

$$\varphi_2 = A\, e^{-kz}\ ;\ \ \phi_1 = B\, e^{-kz} + C\, e^{kz}\ ;\ \ \phi_o = D\, e^{kz} \tag{141}$$

The boundary conditions are that the solution decays away from the CI's and at each CI the z-velocity and the total pressure are continuous. Applying these two boundary conditions at both interfaces produces four linear equations for A, B, C, D. Setting the determinate of the algebraic system to zero produces a dispersion relation:

$$\omega^4\left(1 - e^{-2kL} A_{21}\, A_{10}\right) + \omega^2 (A_{21} + A_{10}) gk + g^2 k^2 A_{21} A_{10}\left(1 + e^{-2kL}\right) = 0 \tag{142}$$

Here A21 and A10 are the Atwood numbers between the 2 and 1regions and between the 1 and 0 regions, respectively. Solving for ω^2:

$$\frac{\omega^2}{gk} = \frac{-1}{2\,(1 - e^{-2kL}\, A_{21}\, A_{10})}\Big\{(A_{21} + A_{10}) + \sqrt{(A_{21} + A_{10})^2 \ \ - 4A_{21}\, A_{10}\,(1 + e^{-2kL})(\,1 - e^{-2kL}\, A_{21}\, A_{10})}\Big\} \tag{143}$$

Only the negative sign above such that if any of the two A's are zero, we retrieve the classical, single CS solution. For a givenA_{20}, we have:

$$\varrho_2 > \varrho_1 > \varrho_o$$

$$A = A_{20} = \frac{\varrho_2 - \varrho_o}{\varrho_2 + \varrho_o} \tag{144}$$

$$\varrho_1 = \varrho_o + \alpha\,(\varrho_2 - \varrho_o); \qquad 0 < \alpha < 1 \tag{145}$$

Therefore for a given A and α, the corresponding two Atwood numbers can be computed as:

$$A_{21} = \frac{1-\alpha}{1+\ \alpha\, A}\ \ A; \quad A_{10} = \frac{\alpha}{1-(1-\alpha)A}\ \ A \tag{146}$$

$$\frac{(\omega_r, \omega_i)}{\sqrt{gkA_{20}}} = i\ sqrt(\frac{1}{2A_{20}\ T_1}\{(A_{21}+A_{10}) + \sqrt{\ (A_{21}+A_{10})^2\ \ -4\ \ A_{21}\,A_{10}\,(1+\ e^{-2kL}\ )T_1}\}) \tag{147}$$

Here,$T_1 = 1 - e^{-2kL}\ A_{21}\ A_{10}$.

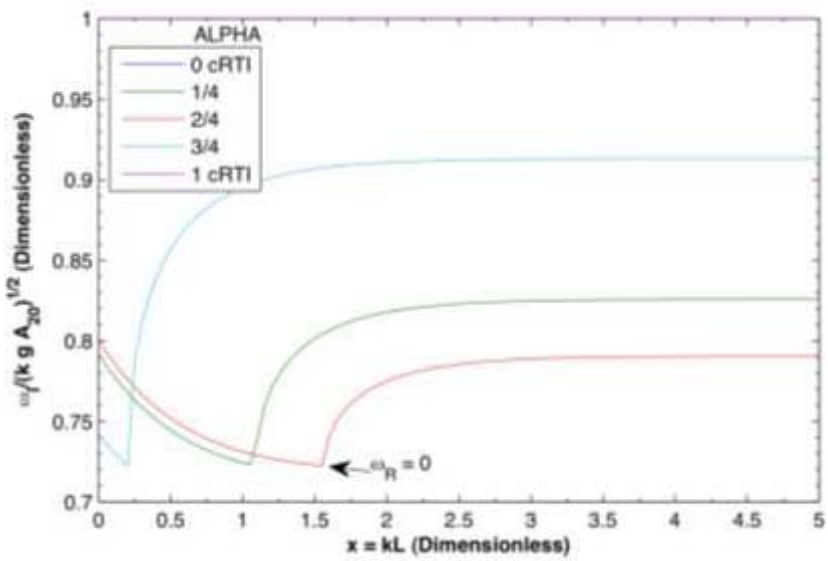

Figure 4–9. Imaginary Part of Omega.

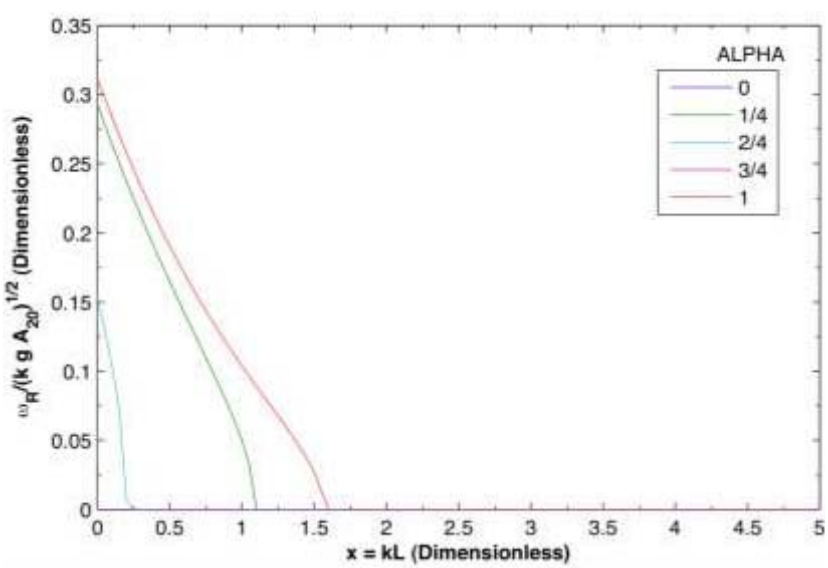

Figure 4–10. Real Part of Omega.

We show in Figure 4–9 and Figure 4–10 the imaginary and real pars of the growth rate for A=0.4. The amplification rate is given by the imaginary component. We note that when the density discontinuity in one of the CS is zero, the amplification rate of the other one is the same as that of the classical RTI:

$$\alpha = 0, \quad then\, \varrho_1 = \varrho_o \quad A_{10} = 0; \qquad \omega = i\sqrt{gkA_{21}} \tag{148}$$

$$\alpha = 1, \quad then\, \varrho_1 = \varrho_2 \quad A_{21} = 0; \qquad \omega = i\sqrt{gkA_{10}} \tag{149}$$

Also, if kL is very large

$$kL \to \infty, \quad e^{-kL} \to 0 \tag{150}$$

$$\omega^2 = -gk\, A_{21}; \quad \omega = i\sqrt{gkA_{21}} \tag{151}$$

Physically this means, $kL \gg 1; \quad L \gg \frac{1}{k}$, i.e., the thickness is much larger than the x-wave length, the presence of the other CS diminishes.

When kL is order (1), then the square root may have an imaginary part. Thus, the presence of two CS in the proximity of each other can result in modifying each individual CS's growth rate and in introduce an oscillatory component in the time development of the perturbations.

4.4. Proposed Work

We considered here in the problem of flow instability associated with forming two distinct material interfaces resulting from the detonative release of energy while including the effects of the presence of solid particles. A splitting technique is adopted in which each flow component is split into a base flow and linearized perturbations, and a high-fidelity numerical simulation code is developed to solve the resulting two systems of equations. Results for the base flow with no solid particles are presented for reference. The newly developed Eulerian-Eulerian approach for studying the effect of solid particles is verified for the planar case. For the perturbation flow, we have presented an analytical model to examine the effect of having two distinct contact surfaces in the proximity of each other. The two CI represent the gas-gas interface, and the mixture-gas interface. Further numerical results for the base flow and perturbations will be presented in the final manuscript.

We are currently working on performing the following tasks which will shed some light on the instability of the multiphase problem. These tasks will define the scope of my thesis.

- Employ the two fluid Eulerian model and verify the base flow by comparing it with the Lagrangian-Eulerian base flow.
- Numerically evaluate the perturbation equations for the two phase problem and vary the spherical wave number.

- Compare the growth of the multiphase interface with the growth of the single gas-gas interface from Chapter 2.
- Study the effects of Viscous diffusion, thermal diffusivity, and mass diffusion on the two phase problem and compare with the single-phase results from Chapter 3.
- Explore the new instability's parametric space by varying the initial location of the gas-particle interface and the initial mass fraction distribution.
- Past the linear regime, observe the continued growth of the instability into the nonlinear regime.

5. SUMMARY

The inviscid case was covered in great detail in Chapter 2 and a parametric study was performed across various pressure and density ratios. The inviscid results revealed a region of constant exponential growth that was compared with various theoretical works. The comparison revealed that the effect of compressibility for constant adiabatic index was stabilizing while the spherical Bell-Plesset effects were destabilizing. There exists a regime of wave numbers where the growth rate is proportional to the square root of the wave number as in the classical Raleigh-Taylor instability. Due to the finite thickness of the interface, for very large wavenumbers the growth rate saturates. The results of the inviscid case were published in the Journal the Physics of Fluids.

Upon investigating the inviscid problem, the viscous terms were included in order to better capture the real world physics of the problem. As wave number is increased to a large enough value that it is of the same order as the square root of the Reynolds number the viscous effects begin to dampen the instability. A maximum growth rate is reached at a given wave number beyond which further increase in the wave number results in a decay of the growth rate. The peak amplification rate occurs at a wave number that scales with the square root of the Reynolds number. Hence, if the Reynolds number is decreased by two orders of magnitude then the corresponding peak wave number is decreased by one order of magnitude. Furthermore, the thermal diffusivity effects are the same as that of the viscous effects in that they also dampen the growth at the instability. As was the case for the viscous effects, also the thermal diffusivity effects are only important when the square root of the Reynolds number is of the same order as the wave number. Likewise, mass diffusivity effects are the same as that of the thermal diffusivity effects in that they also slightly dampen the growth of the instability at very large wave numbers.

Upon inclusion of solid particles, in addition to the gas-gas contact interface the gas-particle interface is of interest especially due to its close proximity to the gas-gas interface. The base flow problem is modeled by an Eulerian-Eulerian approach and the resulting instability PDEs are similar to that of the gas-gas interface's instability. Hence, the same numerical technique applied to the single-phase problem can be employed for the multi-phase problem.

6. REFERENCES

Amendt, P., J.D. Colvin, H.F. Ramshaw, H.F., Robey, and O.L. Landen, 2003, "Modified Bell-Plesset Effect with Compressibility: Application to double-shell ignition target designs," *Physics of Plasmas* 10: pp. 820-829.

Balakrishnan, K. and Menon, S., 2010, "On the Role of Ambient Reactive Particles in the Mixing and Afterburn behind the Explosive Blast Waves", *Combustion Science and Technology* 182: pp. 186–214, Taylor and Frances.

Balakrishnan, K., Menon, S., 2011, "Characterization of the Mixing Layer Resulting from the Detonation of Heterogeneous Explosive Charges," Flow Turbulence Combust 87: pp. 639-671, Springer.

Bandiera, R., 1984, "Convective Instability," Astronomy and Astrophysics, 139: pp. 368-374.

Bell, G.I., 1951, "Taylor Instability on Cylinders and Spheres in the Small Amplitude Approximations," Report LA-1321, Los Alamos National Laboratory.

Bernstein, I.B. and D.L. Brook, 1983, "Effect of Compressibility on the Rayleigh-Taylor Instability," *Physics of Fluids* 26(453).

Brode, H. L., 1955, "Numerical Solutions of Spherical Blast Waves," *Journal of Applied Physics* 26: pp. 766-775.

Brode, H. L., 1959, "Blast Waves from a Spherical Charge," *Physics of Fluids* 2(2): pp. 217-229.

Cant, R.S., W.N. Dawes, and A.M. Savill, 2004, "Advanced CFD and Modeling of Accidental Explosions," *Annual Review of Fluid Mechanics*, 36: pp. 97-119, ISSN 0066-4189.

Chandrasekhar, S., 1981, *Hydrodynamic and Hydromagnetic Stability,* NY, NY: Dover Publications, Inc.

Duff, R.E., F.H. Harlow, and C.W. Hirt, 1962, "Effects of diffusion on interface instability between gases," *Physics of Fluids* 5: pp. 417-425.

Epstein, R., 2004, "On the Bell-Plesset Effects: The Effects of Uniform Compression and Geometrical Convergence on the Classical Rayleigh-Taylor Instability," *Physics of Plasmas* 11(11): pp. 5114-5124.

Erpenbeck, J.J., 1962, "Stability of step shocks," *Physics of Fluids* 5: p. 1181.

Fraschetti, F., R. Teyssier, J. Ballet, and A. Decourchelle, 2010, "(2010), "Simulation of the Growth of the 3D Rayleigh-Taylor Instability in Supernova Remnants using an Expanding Reference Frame," *Astronomy and Astrophysics manuscript*, 515(Article Number A104)(2010).

Friedman, M. P., (1961), "A simplified Analysis of Spherical and Cylindrical Blast Waves," *Journal of Fluid Mechanics*, 11: pp.1-15.

Frost, D.L., Z. Zarei, and F. Zhang, 2005, "Instability of Combustion Products Interface from Detonation of Heterogeneous Explosives," 20th International Colloquium on the Dynamics of Explosions and Reactive Systems, Montreal, Canada.

Hao, Y. and A. Prosperetti, 1999, “The Effect of Viscosity on the Spherical Stability of Oscillating Gas Bubbles,” *Physics of Fluids* 11(6): pp. 1309-1317.

Haselbacher, A., 2005, “A WENO Reconstruction Algorithm for Unstructured Grids Based on Explicit Stencil Construction,” AIAA paper 0879.

Jian, G.S. and C. W. Shu, 1996, “Efficient Implementation of Weighted ENO Scheme,” *J. Computational Physics* 126: pp. 202-228.

Kuhl, A. L., J.B. Bell, V.E. Beckner, and H. Reichenbach, 2011, “Gas Dynamics Model of Turbulent Combustion in TNT Explosions,” Proceedings of the Combustion Institute, 33: pp. 2177-2185.

Kushnir, D., E. Waxman, and D. Shvarts, 2005,“The Stability of Decelerating Shock Waves Revisited,” *The Astronomical Journal*, 634: pp. 407-418.

Lin, H., B.D. Storey, and A.J. Szeri, 2002, “Rayleigh-Taylor Instability of Violently Collapsing Bubbles,” *Physics of Fluids* 14(8): pp. 2925-2928.

Lindl, J.D., 1998, “Inertial Confinement Fusion,” New York: Springer-Verlag.

Ling, A., A. Haselbacher, A. and S. Balachandar, 2009, “Numerical Investigation of Particle Dispersal in Multiphase Explosions,” AIAA-2009-1532, Aerospace Sciences Meeting.

Ling, Y., A. Haselbacher, and S. Balachandar, 2009 “Transient Phenomenon in One-Dimensional Compressible Gas-Particle Flows,” Shock Waves, 19:67-81.

Ling, Y., A. Haselbacher, and S. Balachandar, 2010, “Numerical Investigation of Particle Dispersal in Multiphase Explosions,” AIAA2010-768, Aerospace Sciences Meeting, Orlando, FL.

Mankbadi, M.R. and S. Balachandar, 2011, “Instability of Rapidly Expanding Spherical Material Interfaces," ASME IMECE2011-62400, ASME International Mechanical Engineering Congress and Exposition.

Mankbadi, M.R. and S. Balachandar, 2012a, “Compressible Inviscid Instability of Rapidly Expanding Spherical Material Interfaces,” Accepted to the *Physics of Fluids*.

Mankbadi, M.R. and S. Balachandar, 2012b, “Viscous Effects on the Rayleigh-Taylor Instability of Rapidly Expanding Spherical Material Interfaces,” AIAA-2012-0437, 50th AIAA Aerospace Sciences Meeting including the New Horizons Forum and Aerospace Exposition, Nashville, Tennessee, USA.

Marshall, S.P., R. Stone, C. Heghes, T.J. Davies, and R.F. Cracknell, 2010, "High Pressure Laminar Burning Velocity Measurements and Modeling of Methane and n-Butane," *Combustion Theory and Modeling* 14(4): pp. 519-540.

McFadden, J.A., 1952, “Initial behavior of a spherical blast,” *Journal of Applied Physics* 23(1269).

Meshkov, E. E., 1969, "Instability of the Interface of Two Gases Accelerated by a Shock Wave”, *Soviet Fluid Dynamics* 4: pp. 101-104.

Plesset, M.S., 1954, “On the Stability of Fluid Flows with Spherical Symmetry,” *Journal of Applied Physics* 25(1): pp. 96-98.

Prosperetti, A., 1977, “Viscous Effects on Perturbed Spherical Flows,” *Applied Mathematics Quarterly* 34(339).

Rayleigh, L., 1900, “Scientific Papers II,” Cambridge University Press, Cambridge, England.

Richtmyer, D. H., 1960, Communication in Pure Applied Mathematics 13(297).

Roe, P. L. and J. Pike 1984 and 1999, “Efficient Construction and Utilization of Approximate Riemann Solutions*,” Computational Methods in Applied Sciences and Engineering, North-Holland*.

Roe, P.L., 1981, “Approximate Riemann Solvers, Parameter Vectors, and Difference Schemes,” *Journal of Computational Physics*, 43: pp. 357-372.

Ryu, D. and E.T. Vishniac, 1987, “The Growth of Linear Perturbations of Adiabatic Shock Waves,” *The Astrophysical Journal*, 313: pp. 820-841.

Schwer, D., and K. Kailasanath, 2003, “Blast Mitigation by Water Mist (2) - Shock Wave Mitigation using Glass Particles and Water Droplets in Shock Tubes,“ NRL/MR/6410-03-8658, US Naval Research Laboratory.

Sedov, L. I., 1946, “Propagation of Intense (Strong) Blast Waves,” *Prikl. Mat. Mek. (PMM)*10: p. 241 (in Russian); See also Sedov, L.I., 1959 and 1993, “Similarity and Dimensional Methods in Mechanics, “Academic Press, NY, Chapter 4, (10th ed, CRC Press, London.

Sharp, D.H., 1984, “An overview of Rayleigh-Taylor Instability,” *Physica D* 12(3).

Swan, G.W. and G. R. Fowles, 1975, “Shock wave stability,” *Physics of Fluids* 18: pp. 28–35.

Taylor, G. I., 1950a, “Hydrodynamic Instabilities,” Proceedings of the Royal Society, Ser. A, 201: p. 192.

Taylor, G. I., 1950b, “The formation of a blast wave by a very intense explosion I,” Proceedings of the Royal Society, Ser. A, 201: pp. 159-174.

Toro, E. F., 2009, “Riemann Solvers and Numerical Methods for Fluid Dynamics,” Springer-Verlag, Berlin.

Turner, L., 2002, “Rayleigh-Taylor Instabilities and Gravity Waves in Compressible Fluids,” Los Alamos National Laboratory Report LA-UR 02-6439.

Vandervoot, P.O., 1961, “The Character of the Equilibrium of a Compressible, Inviscid Fluid of Varying Density,” *Journal of Astrophysics* 134(1961): p. 699.

Yang, Y., and Q. Zhang, 1993, “General Properties of a Multilayer Stratified Fluids Systems," *Physics of Fluids A*, 5: p. 1167.

Yu, H. and D. Livescu, 2008, “Rayleigh-Taylor Instability in Cylindrical Geometry with Compressible Fluids," *Physics of Fluids*, 20,104103.

DISTRIBUTION

1	MS0899	Technical Library	9536 (electronic copy)
1	MS0359	D. Chavez, LDRD Office	1911

Sandia National Laboratories